Design Optimization of Structures with Shape Memory Alloy Member Actuators

Michele Pachikara

A thesis
submitted in partial fulfillment of the
requirements for the degree of

Master of Science in Aeronautics and Astronautics

University of Washington

2013

Committee:
Eli Livne, Chair
Keith Holsapple

Program Authorized to Offer Degree:
Aeronautics and Astronautics

University of Washington

Abstract

Design Optimization of Structures with Shape Memory Alloy Member Actuators

Michele Pachikara

Chair of the Supervisory Committee:
Eli Livne, Professor
Aeronautics and Astronautics

A capability was developed to perform mass-minimization of a truss with SMA actuation to determine optimal element diameters and actuator applied temperature changes. The Nonlinear Programming/Approximation Concepts (NLP/AC) approach was used. This method is based on using a sequence of approximate optimization problems rather than optimizing with the full nonlinear analyses. Some special approximations based on new intermediate variables were used. Results are presented and analyzed.

Table of Contents

List of Figures

1 Introduction

1.1 Motivation

Multidisciplinary design, analysis, and optimization (MDAO) is an important research field that is part of the drive for maintaining competitiveness in areas such as the aerospace industry. The current aerospace design process includes enduring several design cycles involving sub-groups such as aerodynamics, structures, and controls, leading to large amounts of re-work and risk of miscommunication between the disciplines. It would be ideal to incorporate the objectives and constraints of all major design groups into one integrated tool, greatly streamlining the aircraft design process. Obviously, designing and optimizing a massive system such as an aircraft, or even an aircraft subsystem, is a daunting task that still requires much research into developing the MDAO process. An impetus behind this work is to contribute to exploring the subject of multidisciplinary optimization in the active structures and aeroservoelastic areas.

Smart materials such as shape memory alloy and piezoelectric materials have demonstrated properties that, when integrated into a moving structure, can theoretically provide benefits over their electromechanical counterparts; therefore, there is a need to integrate these materials into design tools, which will take advantage of their contribution to the optimization of structures. This work also seeks to explore the challenges associated with modeling and implementing smart materials into an active structures optimization routine.

1.2 Smart Material Background and Applications

The piezoelectric phenomenon was discovered in 1880 when Pierre and Jacques Curie were studying the electrical charge generation of Quartz and other crystals when under pressure. Since then, piezoelectric materials have been applied to communications, automotive, and medical systems, among many others [1]. In aerospace and other engineering disciplines, piezoelectrics have been coupled with control systems for active vibration and noise control as well as shape control. For example, NASA Langley examined the application of piezoelectric actuation (among other materials) to aircraft morphing and health monitoring [3]; however, traditional piezoelectric materials are usually unable to produce the large displacements necessary for morphing, which is a large disadvantage for these kinds of materials in aerospace applications.

Shape memory alloys have been in use for decades, with the shape memory effect being first documented in 1932 and the medical profession using SMA's in anything from orthodontic braces to surgical procedures since the 1970s [4,5]. More recently, shape memory alloys have gained attention from the aerospace industry for their potential to simplify existing actuation systems, among other benefits. For example, a single SMA component is capable of producing large deformations and forces in a small amount of area. This high energy density implies that an SMA actuator will have a much lower complexity when compared with the more traditional electromechanical and hydraulic actuators. Despite these benefits, the shape memory alloy's highly nonlinear and hysteretic properties make the material difficult to both model and control. Also, the response time of the SMA is fairly slow, especially when cooling the material; nevertheless, SMAs have found themselves in numerous aeronautical applications and research projects.[2]

Reference [6] surveys the aerospace applications of shape memory alloys. One example of the many SMA fixed-wing projects, the Smart Wing program, sought to demonstrate the effectiveness of smart actuation on morphing a lifting body. Also, Boeing has done much research related to SMAs, with one project including the placement of SMA beams on engine chevrons to reduce engine noise at low altitudes. Boeing has also filed a patent related to using various SMA actuation techniques for deployable surfaces around an aircraft [7]. Other SMA applications pertain to rotorcraft, satellites, and other spacecraft.

1.3 Approach

This work presents an exploratory study of the MDAO process focused on a two dimensional structural optimization problem with SMA materials used for strain-based actuation. Chapter 2 provides a review of the fundamentals of structural analysis, such as stiffness and mass matrices creation, displacement and stress calculations, and an introduction to modeling SMA rod actuator elements. This modeling is validated using a truss structural analysis problem. Chapter 3 proceeds with an introduction to sensitivity computation, a crucial element in gradient-based optimization, as well as the development of stress and displacement constraints. In Chapter 4, the NLP/AC optimization method is introduced as well as approximation techniques to accelerate the optimization process. These methods are validated on the same truss structure as in Chapter 3, first with stress constraints then again with stress and displacement constraints. Chapter 5 presents a strain-based truss structure with solid aluminum rods as caps and hollow SMA rods for actuation. The objective and constraint functions are developed for this active structure, and it is noticed for this application that a new approximation method can be employed. The results of the new optimization technique and process described in Chapter 5 are shown in Chapter 6. Chapter 7 ends the research with conclusions and suggestions for future work.

2 Structural Analysis

2.1 Finite Element Derivations

The finite element modeling for this research was based on the SMART code [8], developed at the University of Washington, a Fortran-based capability for preliminary design of aircraft augmented with strain actuation – namely piezoelectric materials and shape memory alloy. For the purposes of this project, portions of SMART's finite element modeling were converted into Matlab and augmented. The capabilities include producing stiffness and mass matrices for truss and membrane elements, force induced by strain actuation, and stress calculation. See Appendix A for membrane element derivations, as they are not used in this reported exploratory study. A technical briefing of these details is discussed in the following sections. References [8] or [9] offer more details.

2.1.1 Degrees of Freedom

SMART always assumes 6 degrees of freedom (DOFs) per node in the finite element model; however, since this exploratory study uses elements that are not capable of rotational motion, the degrees of freedom per node do not exceed three and the rest are zeroed out as single point constraints. For example, displacement DOFs at a node is represented in Eq (2.1).

$$\{u\} = \{u \quad v \quad w \quad \theta_x \quad \theta_y \quad \theta_z\} \tag{2.1}$$

The 3 DOF problem eliminates the need for the θ_x, θ_y, and θ_z degrees of freedom.

2.1.2 Truss Element

A straight element with a node at each end, the truss element displaces only in the axial direction [9]. In the element's local system, the element stiffness matrix can easily be derived, resulting in Eq (2.2).

$$[K_e] = \frac{AE}{L}\begin{bmatrix} 1 & -1 \\ -1 & 1 \end{bmatrix} \tag{2.2}$$

A is the cross sectional area of the truss element, E is the modulus of elasticity of the material used, L is the length of the bar, and the displacement degrees of freedom are $\{u_1 \quad u_2\}$. This stiffness matrix is expanded into a 12x12 matrix to account for the 6 degrees of freedom per node in the element, with the only populated elements of K_e corresponding to those associated with u_1 and u_2. The element stiffness matrix may then be transformed into global coordinates for assembly into the structure's global stiffness matrix, $[K]$.

The mass matrix may be represented in two different ways, depending on the manner in which to situate an element's mass. The lumped mass representation is more computationally simple, as the matrix is diagonal, and it is computed by dividing the element's mass equally amongst the two nodes. The lumped mass matrix in element coordinates is:

$$[M_e^{lumped}] = \frac{\rho AL}{2}\begin{bmatrix} 1 & 0 \\ 0 & 1 \end{bmatrix} \tag{2.3}$$

The parameter ρ is the mass density of the material, and the displacement degrees of freedom are $\{u_1 \quad v_1 \quad w_1 \quad u_2 \quad v_2 \quad w_2\}$. When using Imperial units, lbm must be converted to slinches.

The consistent mass representation for the truss element is shown in Eq (2.4).

$$[M_e^{consistent}] = \frac{\rho AL}{6}\begin{bmatrix} 2 & 1 \\ 1 & 2 \end{bmatrix} \tag{2.4}$$

The displacement DOFs are $\{u_1 \quad u_2\}$, but the matrix must be repeated for DOF $\{v_1 \quad v_2\}$ and $\{w_1 \quad w_2\}$ then assembled into a 12x12 matrix. The element mass matrix may then be transformed into global coordinates for assembly into the structure's global stiffness matrix, $[M]$.

2.1.3 Shape Memory Alloy Actuators

Due to their growing importance and potential, SMA strain-based actuation has been modeled. While structural parameters for both shape memory alloy and piezoelectric materials were calculated in the development of this work, only SMA rod actuators were ultimately considered. For derivations of the piezoelectric rod and membrane actuators as well as membrane SMA actuators, see Appendix A.

The unique properties of the SMA are a result of a transition between two phases of the material: austenite, the high temperature phase also called the "parent" phase, and martensite, the low temperature phase. When austenite is being cooled, in the absence of stress, the transition begins at the martensitic start temperature, M_s, and ends at the martensitic finish temperature, M_f, at which the material is fully martensite. Conversely, when martensite is heated, the transition begins at the austenitic start temperature, A_s, and ends at the austenitic finish temperature, A_f, where the material is fully austenite.[6]

The phenomenon that contributes to the SMA's namesake, the shape memory effect, showcases the material's potential role as an actuator. As shown in experimental results in Figure 2-1, austenite (point α) is cooled under constant stress into martensite, resulting in very large strains (path β-γ). In this scenario, β refers to the point where M_s is met, and γ refers to the point where M_f is reached. Heating the material back to austenite, which includes meeting A_s at point δ and reaching A_f at point ϵ, almost completely recovers from the large strains.

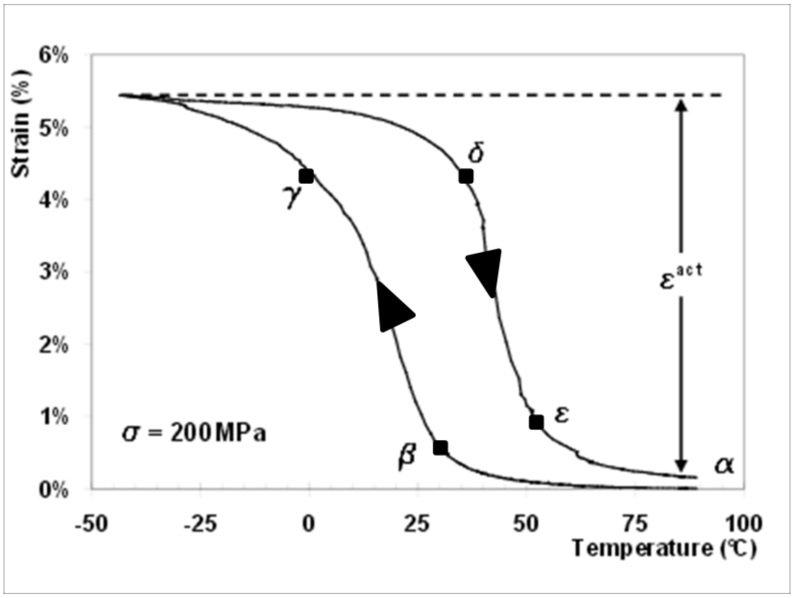

Figure 2-1: Shape Memory Effect [6]

The one-dimensional SMA actuator is modeled as a bias-force actuator, which uses a spring to generate the restoring forces [10,11].

Liang and Rogers provide a comprehensive set of one-dimensional constitutive relationships for shape memory alloy materials as well as their derivations [11]. Representative derivations are shown below. As evident in Figure 2-1, the martensitic fraction, ξ, of the material changes as a function of temperature in the absence of stress. Liang and Rogers chose to represent the $\xi - T$ relationships as a cosine function, as expressed in Eqs (2.5) and (2.6) for the martensite to austenite ($M \rightarrow A$) and the austenite to martensite ($A \rightarrow M$) transformation, respectively.

$$\xi = \frac{\xi_M}{2}\{\cos[a_A(T - A_s)] + 1\} \tag{2.5}$$

$$\xi = \frac{1-\xi_A}{2} cos\left[a_M(T - M_f)\right] + \frac{1+\xi_A}{2} \tag{2.6}$$

Here, a_A and a_M are material constants defined in Eqs (2.7) and (2.8).

$$a_A = \frac{\pi}{A_f - A_s} \tag{2.7}$$

$$a_M = \frac{\pi}{M_s - M_f} \tag{2.8}$$

To add stress into the equation, it has been experimentally determined in Liang and Rogers that the transition temperatures M_f, M_s, and A_s are linearly related to applied stress. It is also assumed that, although the A_f relationship is actually more complicated, the austenite finish temperature behaves in the same linear way as the other temperatures. Two other material constants are created, C_A and C_B, which are defined as the tangent of the slope of the linear relationship between stress and temperature. Adding a stress-induced phase transition term, Eqs (2.5) and (2.6) are re-written to become Eqs (2.9) and (2.10).

$$\xi = \frac{\xi_M}{2}\{\cos[a_A(T - A_s) + b_A\sigma_{sma}] + 1\} \tag{2.9}$$

$$\xi = \frac{1-\xi_A}{2} cos\left[a_M\left(T - M_f\right) + b_M\sigma_{sma}\right] + \frac{1+\xi_A}{2} \tag{2.10}$$

Where the material constants b_A and b_M are:

$$b_A = -\frac{a_A}{C_A} \tag{2.11}$$

$$b_M = -\frac{a_M}{C_M} \tag{2.12}$$

The actuator's response is assumed to be a quasi-static process. For this process, the general relationship between stress and temperature is written in Eq (2.13).

$$\sigma_{sma} - \sigma_0 = \Theta'(T - T_0) + \Omega'(\xi - \xi_0) \tag{2.13}$$

Where

$$\Theta' = \frac{\Theta}{1 + \frac{AE}{k_s L}}, \Omega' = \frac{\Omega}{1 + \frac{AE}{k_s L}} \tag{2.14}$$

This constitutive relation is a function of the initial conditions (temperature T_0, stress σ_0, and martensitic fraction ξ_0); SMA material properties – wire length L, elastic modulus E, thermoelastic tensor Θ, phase transformation tensor Ω, stress σ, strain ϵ, temperature T, and martensitic fraction ξ; as well as the bias spring constant, k_s.

The initial equilibrium state of the actuator is expressed in Reference [10] and repeated in Eq (2.15), and the spring force is defined in Eq (2.16).

$$\sigma_0 A = F_s + W \tag{2.15}$$

$$F_s = k_s L(\epsilon_{res} - \epsilon) \tag{2.16}$$

The parameter ϵ_{res} is the martensitic residual strain, which is caused by repeated loading and unloading.

Using the stress-temperature relationship from Eq (2.13), along with the knowledge of the start and finish temperatures mentioned previously, the stress in the SMA fiber may be calculated. During the heating process, if the actuator temperature is lower than T_M, the initial state temperature, then the stress in the SMA is σ_0; otherwise, the stress-temperature relationships are as follows.

$$\sigma_{sma} = \begin{cases} \Theta'(T - T_M) + \sigma_0 & T_M \leq T \leq A_s^m & (2.17a) \\ \Theta'(T - A_s^m) + \Omega'(\xi - \xi_h) + \sigma_{As} & A_s^m \leq T \leq A_f^m & (2.17b) \\ \Theta'(T - A_f^m) + \sigma_{Af} & A_f^m \leq T & (2.17c) \end{cases}$$

The temperatures A_s^m and A_f^m represent the mechanical transition temperatures, as it was previously mentioned that the transition temperatures change with applied stress. The stresses corresponding to the mechanical transition temperatures are σ_{As} and σ_{Af}. The definition of these parameters can be found in References [10] and [11].

When cooling from austenite to martensite, if the actuator temperature is greater than the initial state temperature, T_C, the stress in the SMA is σ_0. Otherwise, the stress-temperature relationships are shown in Eq (2.18).

$$\sigma_{sma} = \begin{cases} \Theta^{'}(T - T_C) + \sigma_0 & T_C \geq T \geq M_s^m & (2.18a) \\ \Theta^{'}(T - M_s^m) + \Omega^{'}(\xi - \xi_c) + \sigma_{Ms} & M_s^m \geq T \leq M_f^m & (2.18b) \\ \Theta^{'}(T - M_f^m) + \sigma_{Mf} & M_f^m \geq T & (2.18c) \end{cases}$$

Again, M_s^m and M_f^m are the mechanical transition temperatures, and the corresponding stresses are σ_{Ms} and σ_{Mf}. These temperatures and stresses are calculated in References [10] and [11].

It is noted that Equations (2.9) and (2.10) are also needed to solve the stress equations, (2.17b) and (2.18b). In these cases, stress needs to be calculated as a function of martensitic fraction, but martensitic fraction is in turn a function of stress, leaving two equations with two unknowns. An iterative approach was used to solve for these equations. First, initial guesses are made for ξ and σ_{sma}. For heating, the initial martensitic fraction is taken as 1, and for cooling, the initial martensitic fraction is taken as 0. The initial guess for stress is zero. The equations are then solved iteratively until both martensitic fraction and stress converge. Convergence was determined to be when the next iteration falls within 1% of the value of the previous iteration.

Using the stress computed above, the strain produced by the bias spring is calculated.

$$\epsilon = -(\sigma_{sma} - \sigma_0)\left(\frac{A}{kL}\right) + \epsilon_0 \tag{2.19}$$

The force generated by the actuator is then computed to be, using Hooke's Law.

$$F_{SMA} = \epsilon E A \tag{2.20}$$

E is the modulus of elasticity of the material, and A is the cross-sectional area of the SMA core in the actuator. Then, the SMA force is assembled into the local coordinate system force vector.

$$\{F_e^{SMA}\} = \{-F_{SMA} \quad 0 \quad 0 \quad 0 \quad 0 \quad 0 \quad F_{SMA} \quad 0 \quad 0 \quad 0 \quad 0 \quad 0\}^T \tag{2.21}$$

2.1.4 Global Matrix Assembly

With the mass, stiffness, and load (if applicable) matrices computed in global coordinates for each element, the global structure's versions of these matrices can be created. The global structure's matrices have the following dimensions:

$$[K] \in \mathbb{R}^{N_{DOF} \times N_{DOF}}$$

$$[M] \in \mathbb{R}^{N_{DOF} \times N_{DOF}}$$

$$\{F\} \in \mathbb{R}^{N_{DOF} \times 1}$$

The parameter N_{DOF} represents the number of degrees of freedom of the full system. The global matrices are assembled by relating the nodes of each element to the degrees of freedom of the entire structure. If one node shares various forces acting on it, the forces are added together. When an FEA model is created, a set of six DOF numbers are assigned to each node created. Since the model "knows" which nodes are involved in each element, the relevant global degrees of freedom are also known for each element; as a result, each element in the K, M, and F matrices can be transferred into the appropriate elements of the global matrices.

2.2 Static Analysis

The static problem is written in Eq (2.22).

$$[K]\{u\} = \{F\} \tag{2.22}$$

[K] is the global stiffness matrix, {F} is the global load vector, and {u} is the global displacement vector, the parameter for which to be solved. Before solving the problem, the single point constraints (SPCs) are first implemented into the model. These are constraints that force certain individual degrees of freedom not to move. For simplification, the static problem can be re-written in Eq (2.23).

$$[K_{spc}]\{u_{spc}\} = \{F_{spc}\} \tag{2.23}$$

where $[K_{spc}]$ represents the global stiffness matrix with the columns and rows corresponding to a DOF with an SPC removed, $\{F_{spc}\}$ is the global load vector with rows corresponding to a constrained DOF removed, and $\{u_{spc}\}$ is the displacement vector that represents all non-constrained DOFs. The displacement result is then re-assembled to include the single point constraint displacement with a value of zero.

2.3 Stress

For rod elements, one axial stress is calculated for the entire element. Assuming that the local coordinate displacements of node 1 and 2 are u_1 and u_2, respectively, the axial stress is, in two dimensions:

$$\sigma = E\epsilon = \frac{E(u_2 - u_1)_{local}}{L} = \frac{E}{L}\{-1 \quad 0 \quad 1 \quad 0\}\begin{Bmatrix} u_{x1} \\ u_{y1} \\ u_{x2} \\ u_{y2} \end{Bmatrix}_{local} \tag{2.24}$$

Transforming to global coordinates:

$$\sigma = \frac{E}{L}\{-cos\theta \quad -sin\theta \quad cos\theta \quad sin\theta\}\begin{Bmatrix} u_{x1} \\ u_{y1} \\ u_{x2} \\ u_{y2} \end{Bmatrix}_{global} = \{C\}_{\mathrm{2d}}{}^{\mathrm{T}}\{u\}_{global} \tag{2.25}$$

Expanding to three dimensions:

$$\sigma = \frac{E}{L}\{-\mathrm{l} \quad -\mathrm{m} \quad -\mathrm{n} \quad \mathrm{l} \quad -\mathrm{m} \quad \mathrm{n}\}\begin{Bmatrix} u_{x1} \\ u_{y1} \\ u_{z1} \\ \mathrm{u}_{\mathrm{x2}} \\ u_{y2} \\ u_{z2} \end{Bmatrix}_{global} = \{C\}_{\mathrm{3d}}{}^{\mathrm{T}}\{u\}_{global} \tag{2.26}$$

where l, m, and n are the direction cosines of the bar axis.

The vector {C} can be expanded to a 1 x NDOF vector to have a value of zero everywhere except for the four non-zero elements that are placed in the locations corresponding to the degrees of freedom of the nodes that rod element connects.

For SMA elements, the SMA-induced effect is added to the stress calculation by including another array, D, to the stress equation. To include the SMA-induced stress in the rod, the following expression is used.

$$\sigma = \{C\}^{\mathrm{T}}\{u\}_{global} + \mathrm{D} \tag{2.27}$$

In summary, the process that this study takes to perform structural analysis is as follows:

1. Assemble a structural model with external forces and single point constraints (SPCs) specified.
2. Apply a temperature change to the SMA actuator elements.
3. Calculate elemental K and M matrices from Eq (2.2) and either Eq (2.3) or Eq (2.4), depending on which mass matrix generation option (lumped or consistent) is desired.
4. Begin the creation of the load vector, F, by placing the external forces in the correct DOF location in the vector.
5. For SMA elements, calculate stress in the SMA material using the constitutive relationships described in Eq (2.17) for heating or Eq (2.18) for cooling. If the temperature lies between the values specified in (2.17b) or (2.18b), use the iterative approach specified in Section 2.1.3 to solve for martensitic fraction and stress. When heating, numerically solve the system of equations consisting of Eq (2.9) and Eq (2.17b), and for cooling, numerically solve the system of equations consisting of Eq (2.10) and Eq

(2.18b). Iterate until the convergence criteria are satisfied for the solutions to martensitic fraction and stress, when both parameters come within 1% of the previous iteration's value.

6. Use the stress solution from Step 5 to calculate strain produced by the bias spring in the actuator, using Eq (2.19).
7. Solve for force using Eq (2.20), and assemble this force into the load vector, as in Eq (2.21).
8. Assemble the global K, M, and F for the entire structure, which includes SMA and traditional materials, such as aluminum. When elements share a node, add together the effects.
9. Solve Eq (2.23) for displacement.
10. For each element, calculate the stress in that element using Eq (2.27). For non-SMA materials, D = 0. Assemble all stresses into a vector, $\{\sigma\}$.

2.4 Model Validation

The finite element model was implemented on a 2D truss structure to validate the displacements and stresses computed. The shape memory alloy effects were also validated by using an example from Liang and Rogers.

2.4.1 Truss Structure

Testing the truss element calculations (without SMA actuators) for both Imperial and SI unit capabilities, the 10-bar truss from Haftka and Gurdal is used, as shown in Figure 2-2 [12]. The height of the structure as well as the width of the two bays measure 360 inches (9.144 meters). The structure is composed of aluminum material with a Young's Modulus of 10^7psi (69 GPa) and a density of 0.1 lbm/in^3 (2,700 kg/m^3). At two nodes of the structure, two forces of magnitude 100,000 lbs ($4.45 \times 10^5 N$) push down on the model. The deformation and stress in all members of the structure, in both Imperial and SI units, were computed with the areas given in Table 1 and compared to the results obtained in Haftka and Gurdal. The results are also shown in Table 1.

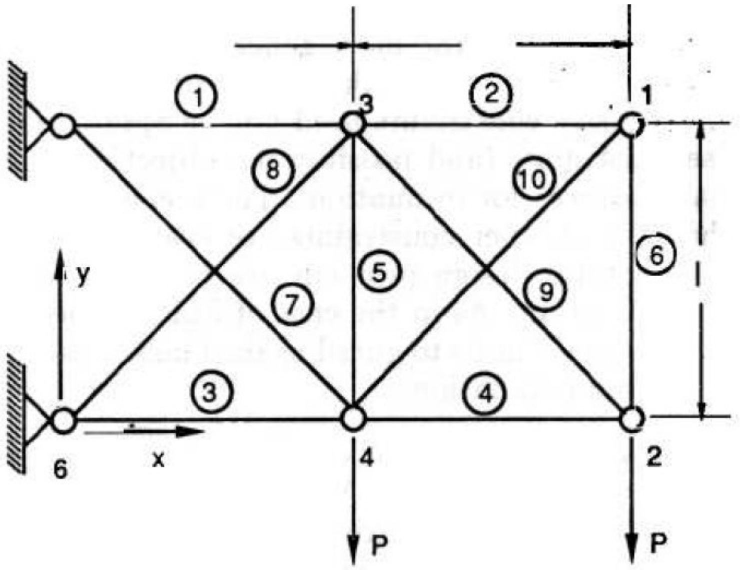

l = 360 ", P = 100 Kips

Figure 2-2: Truss Structure [12]

Table 1: Truss Model Stress Results

Member	Cross-Sectional Area (in^2)	Cross-Sectional Area (m^2)	Stress from Haftka and Gurdal (ksi)	Stress Computed (ksi)	Stress computed (GPa)
1	7.90	5.1×10^{-3}	25.0	25.0	0.17
2	0.10	6.5×10^{-5}	25.0	25.0	0.17
3	8.10	5.2×10^{-3}	-25.0	-25.0	-0.17
4	3.90	2.5×10^{-3}	-25.0	-25.0	0.17
5	0.10	6.5×10^{-5}	-0.07	-0.07	0.00
6	0.10	6.5×10^{-5}	25.0	25.0	0.17
7	5.80	3.7×10^{-3}	25.0	25.0	0.17
8	5.51	3.6×10^{-3}	-25.0	-25.0	-0.17
9	3.68	2.4×10^{-3}	37.5	37.5	0.26
10	0.14	9.1×10^{-5}	-25.0	-25.0	-0.17

It is noted that the calculated stresses exactly match the stresses given in the example. The deformed shape, shown in red, compared with the initial shape of the structure, shown in blue, is displayed in Figure 2-3.

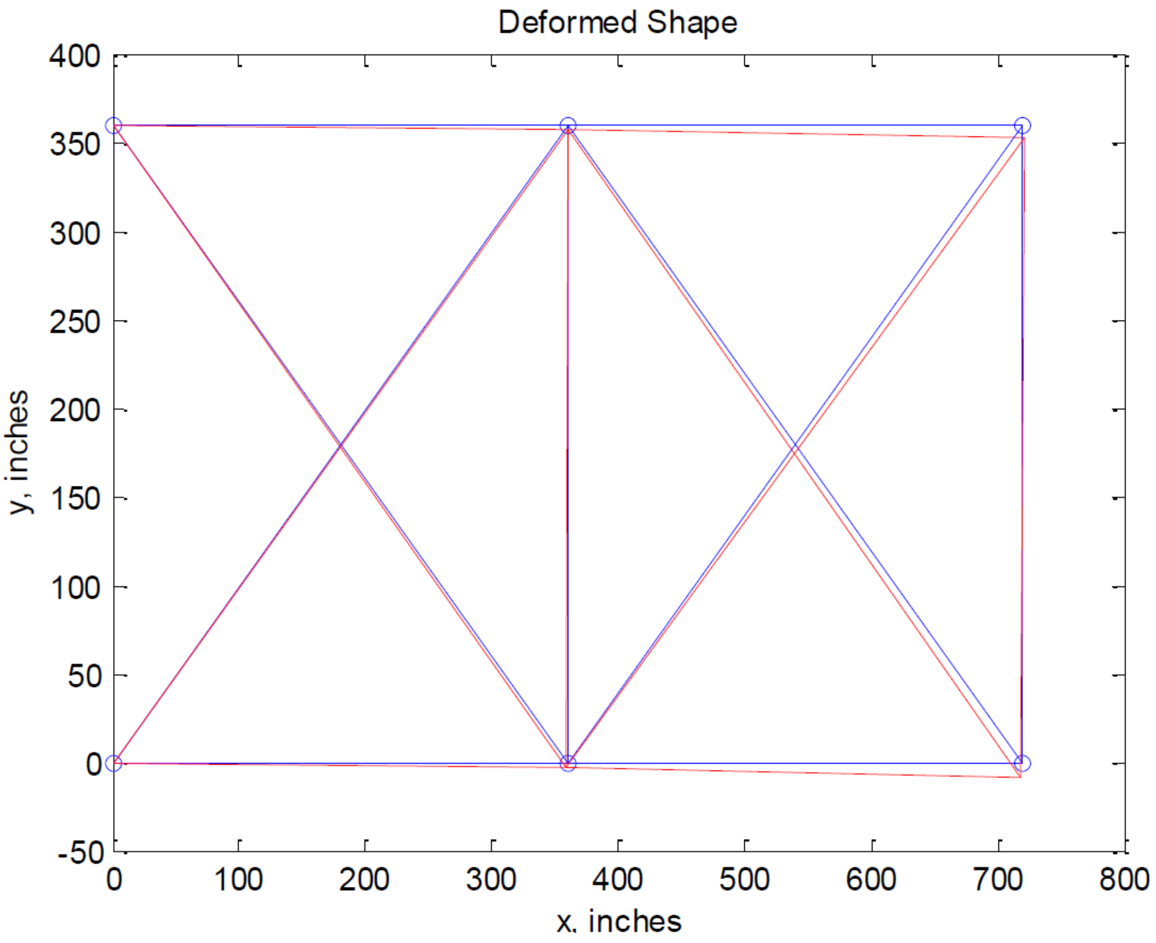

Figure 2-3: Deformed Shape of Truss Structure

2.4.2 Shape Memory Alloy

Following the constitutive relations derived in Reference [11] and shown in Section 2.1.3, a shape memory alloy hysteresis loop is replicated to ensure the model has been coded correctly. Liang and Rogers consider a copper-based SMA material with properties shown in Table 2. The material is first heated from an initial stress of 0 MPa and initial temperature of -35°C up to 25°C.

Throughout the heating process, stress is recorded. The same is done for cooling, where the actuator is initially loaded at 10°C then cooled by 50°C. The stress-temperature hysteresis loop is then recorded, and results are shown in Figure 2-4. It is noticed that these results closely resemble Liang and Rogers' computations in Reference [11].

Table 2: Copper Based SMA Material Constants

(MPa)		(°C)				(MPa/°C)	
E	Ω	M_s	M_f	A_s	A_f	C_A	C_M
7000	-70	-27	-34	-25	-14	1.5	1.5

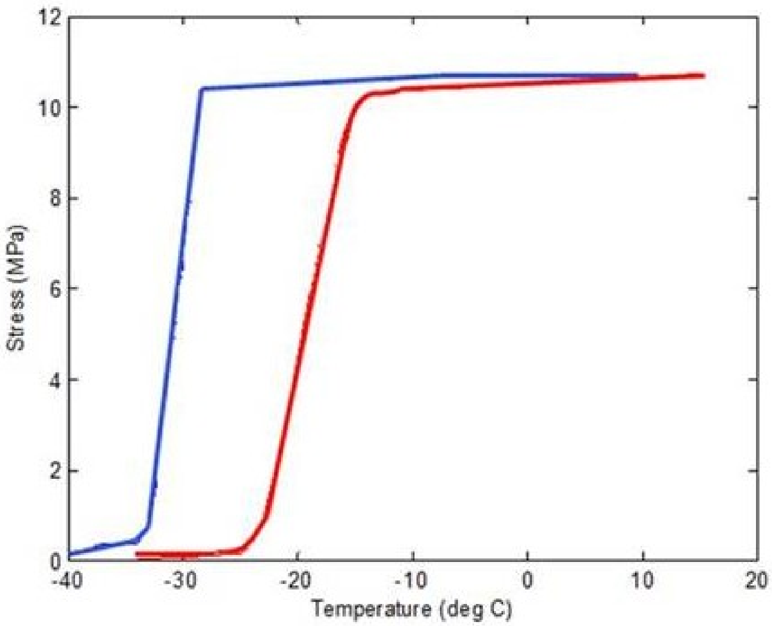

Figure 2-4: Shape Memory Alloy Hysteresis Result

3 Sensitivities

3.1 Introduction

The computation of sensitivities of displacement, stress, and other behavior functions with respect to design variables is an important aspect of gradient-based optimization, as sensitivities are used to construct approximations of the objective and constraint functions. Sensitivities, which were included in the SMART code, have been calculated using finite difference or analytic techniques, as shown in the following sections.

Sensitivities are essentially derivatives calculated with respect to changes in the design variables of the problem. In the exploratory work reported here, the design variables can be any of the following:

- Rod cross-sectional area, A
    - Alternatively, diameters of circular and hollow circular rods, d
- Young's modulus, E
- Material density, ρ
- Temperature change applied to an SMA material, T

3.1.1 Finite Difference Sensitivities

The finite difference method is an easy and straightforward method to determine design sensitivities; however, like other numerical methods, care must be taken to ensure an accurate solution.

The forward difference approximation, known as the first order forward Euler approximation, is derived from the first order Taylor Series.

$$f(x+\Delta x) = f(x) + f'(x)\Delta x \tag{3.1}$$

Performing the arithmetic, the derivative is approximated as:

$$f'(x) \approx \frac{f(x+\Delta x) - f(x)}{\Delta x} \tag{3.2}$$

Therefore, the forward Euler method is performed by evaluating the function at its reference value, perturbing it by a small amount larger than the reference value, and then re-evaluating the function. Perturbing the reference value to a value smaller than itself leads to the backward difference method.

The central difference method is a second order technique that is derived by combining the forward and backward difference methods and by using the second order Taylor series approximation.

$$f(x+\Delta x) \approx f(x) + f'(x)\Delta x + \frac{\Delta x^2}{2} f''(x) \tag{3.3}$$

$$f(x-\Delta x) \approx f(x) - f'(x)\Delta x + \frac{\Delta x^2}{2} f''(x) \tag{3.4}$$

Subtracting the two equations results in the following:

$$f(x+\Delta x) - f(x-\Delta x) \approx 2f'(x)\Delta x \tag{3.5}$$

Solving for the first derivative leads to the central difference approximation, shown in Eq (3.6).

$$f'(x) \approx \frac{f(x+\Delta x) - f(x-\Delta x)}{2\Delta x} \tag{3.6}$$

The step size may greatly affect any finite difference approximation. For example, because first order Euler truncates the 2nd order and higher terms from the Taylor Series, a large step size (Δx) will lead to a poor finite difference approximation due to the truncation of higher order terms. Similarly, too small of a step size may introduce round off error to the solution. Through trial and error, it has been established for the present study that a step size of 1% of the design variable's value will be used as the step size for finite difference sensitivity calculations.

Because the function (the full structural model, in this case) must be evaluated multiple times to calculate a finite difference sensitivity, this numerical method may not be computationally efficient for very large structural models with thousands of degrees of freedom.

Figure 3-1 is a graphical representation of the forward Euler method, as well as backward Euler and the central difference methods for calculating the derivative with respect to a design variable.

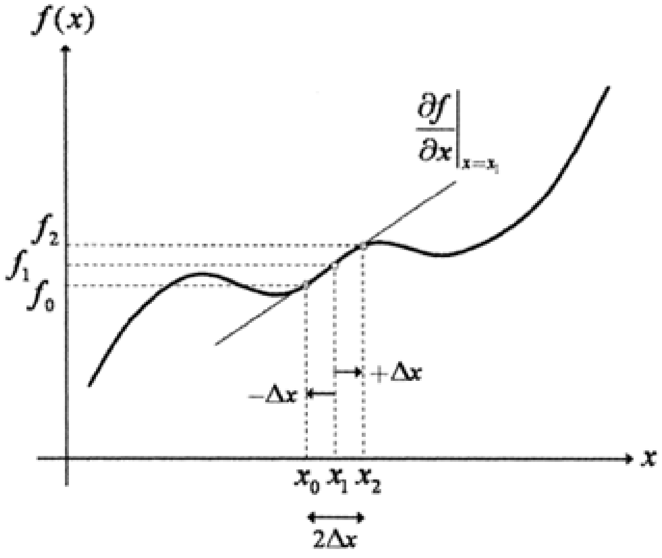

Figure 3-1: Finite Difference Methods [8]

An example of the finite difference method being exercised in SMART is when calculating the sensitivity of the SMA induced stress with respect to temperature change in the SMA actuator. In Eq (2.27), the parameter D introduced the SMA-induced effect, and it is the sensitivity of D with respect to temperature difference that is calculated through the finite difference method. In this case, the temperature difference was increased by 1℃, and D was recalculated. Taking the difference between the two values of D, therefore using the forward finite difference approach, resulted in the sensitivity value.

3.1.2 Analytic Sensitivities

Alternative to finite difference calculations, some sensitivities can be derived analytically, which provides a more efficient approach that is not sensitive to perturbation sizes or numerical issues; however, this approach requires analytic derivatives of often complex equations and added coding and code organization efforts.

Many sensitivities related to static analysis can be computed analytically. Taking the rod element, for example, the expression for the stiffness matrix in local coordinates is known from Eq (2.2), repeated below.

$$[K_e] = \frac{AE}{L}\begin{bmatrix} 1 & -1 \\ -1 & 1 \end{bmatrix} \tag{3.7}$$

Taking the sensitivity of the stiffness matrix with respect to element area results in Eq (3.8).

$$\left[\frac{\partial K_e}{\partial A}\right] = \frac{E}{L}\begin{bmatrix} 1 & -1 \\ -1 & 1 \end{bmatrix} \tag{3.8}$$

The sensitivity of the membrane's element stiffness matrix can also be analytically calculated, which requires knowledge of the sensitivity of the matrix [B] with respect to the design variables. The analytic expression for the matrix [B] can be found in Reference [9].

Similarly, the consistent mass matrix for the rod element is repeated below.

$$[M_e^{consistent}] = \frac{\rho AL}{6}\begin{bmatrix} 2 & 1 \\ 1 & 2 \end{bmatrix} \tag{3.9}$$

Taking the sensitivity with respect to element area yields:

$$\left[\frac{\partial M_e^{consistent}}{\partial A}\right] = \frac{\rho L}{6}\begin{bmatrix} 2 & 1 \\ 1 & 2 \end{bmatrix} \tag{3.10}$$

Again, a similar approach can be taken with the mass matrix of the membrane element.

Returning to the static response problem:

$$[K]\{u\} = \{F\} \tag{3.11}$$

The sensitivity of displacement with respect to design variables can be determined by performing implicit differentiation on both sides of the equation.

$$\frac{\partial[K]}{\partial(DV)}\{u\}+[K]\frac{\partial\{u\}}{\partial(DV)}=\frac{\partial\{F\}}{\partial(DV)} \tag{3.12}$$

Moving a term to the right hand side results in Eq (3.13).

$$[K]\frac{\partial\{u\}}{\partial(DV)}=\frac{\partial\{F\}}{\partial(DV)}-\frac{\partial[K]}{\partial(DV)}\{u\} \tag{3.13}$$

In many cases, the external force is constant, so its sensitivity with respect to design variables is zero; however, for piezoelectric and shape memory alloy actuators, some terms in the force vector are functions of temperature or material properties, leaving a non-zero force sensitivity vector. SMART calculates this force sensitivity analytically by dividing the element force vector by the applied actuator temperature changed. The second term on the right hand side has the already known term $\frac{\partial[K]}{\partial(DV)}$ and the static displacement solution, {u}. The right hand side of Eq (3.13) is known as the "pseudo load". The displacement sensitivities of Eq (3.13) can now be found using the same equation solution techniques used for Eq (3.11).

The sensitivity of stress in an element with respect to design variables is also calculated by using implicit differentiation on Eq (2.27), repeated below.

$$\sigma=\{C\}^T\{u\}+\ D \tag{3.14}$$

Taking implicit differentiation of both sides:

$$\frac{\partial\sigma}{\partial(DV)}=\frac{\partial\{C\}^T}{\partial(DV)}\{u\}+\ \{C\}^T\frac{\partial\{u\}}{\partial(DV)}+\frac{\partial\mathrm{D}}{\partial(DV)} \tag{3.15}$$

In many cases, $\frac{\partial\{C\}^T}{\partial(DV)}$ is equal to zero. In the case of shape memory alloy actuator elements, D is a function of temperature and smart material properties; therefore the sensitivity in such cases is non-zero. As mentioned previously, $\frac{\partial \mathrm{D}}{\partial(DV)}$ is calculated using a finite difference approach.

The most common constraint functions used in this work's optimization problems concern maximum or minimum stresses and maximum or minimum nodal displacements. For example, if there is a constraint for a tensile yield stress, $\sigma_{y_{tens}}$, or compressive yield stress, $\sigma_{y_{comp}}$, in a rod element, the constraints can be written as in Eqs (3.16) and (3.17).

$$g_{\sigma_{tens}} = \frac{\sigma}{\sigma_{y_{tens}}} - 1 \leq 0 \tag{3.16}$$

$$g_{\sigma_{comp}} = -\frac{\sigma}{|\sigma_{y_{comp}}|} - 1 \leq 0 \tag{3.17}$$

The sensitivity of the stress constraint in Eq (3.16) with respect to a design variable is:

$$\frac{\partial g_{\sigma}}{\partial(DV)} = \frac{1}{\sigma_{y_{tens}}}\frac{\partial\sigma}{\partial(DV)} \tag{3.18}$$

Similarly, for a displacement constraint:

$$g_u = \frac{u}{u_{y_{max}}} - 1 \leq 0 \tag{3.19}$$

The sensitivity of the displacement constraint with respect to a design variable is:

$$\frac{\partial g_u}{\partial(DV)} = \frac{1}{u_{y_{max}}}\frac{\partial u}{\partial(DV)} \tag{3.20}$$

4 Optimization

4.1 Optimization Strategy

So far, a capability to compute mass and stiffness matrices, element loads, and sensitivities with respect to design variables has been described. The next step is to optimize an objective function subject to constraints on the element's capabilities and range of acceptable design variables. The general optimization problem in this research is a minimization problem, shown below:

$$\begin{gathered} \min F(\{x\}) \\ \\ \mathit{Subject\ to}: \\ \{g\} \leq 0 \\ \{lb\} \leq \{x\} \leq \{ub\} \end{gathered} \tag{4.1}$$

Here, F is the objective function to minimize, g is a vector of constraint values, and {lb} and {ub} are vectors including the side constraints for the design variables. The constraints are written in a manner such that they are feasible when their values are less than zero.

The Nonlinear Programming Approximation Concepts (NLP/AC) strategy, also known as optimization with surrogate modeling, is used to perform the optimization. Essentially, the problem begins with an "exact", nonlinear model to optimize. Then, the technique converts this model into a series of approximate problems over which optimization is carried out to achieve an approximate optimal result. Move limits are imposed in order to preserve the integrity of the approximation throughout the optimization. Then, the approximate optimal result is fed into the "exact" (or detailed) nonlinear simulation for computation of objective function values, sensitivities, and constraint values. The exact values are used to check the accuracy of the approximate values reached by the approximate optimization. When the objective function converges and the constraints are satisfied, the optimization is complete. Figure 4-1 details the NLP/AC process.

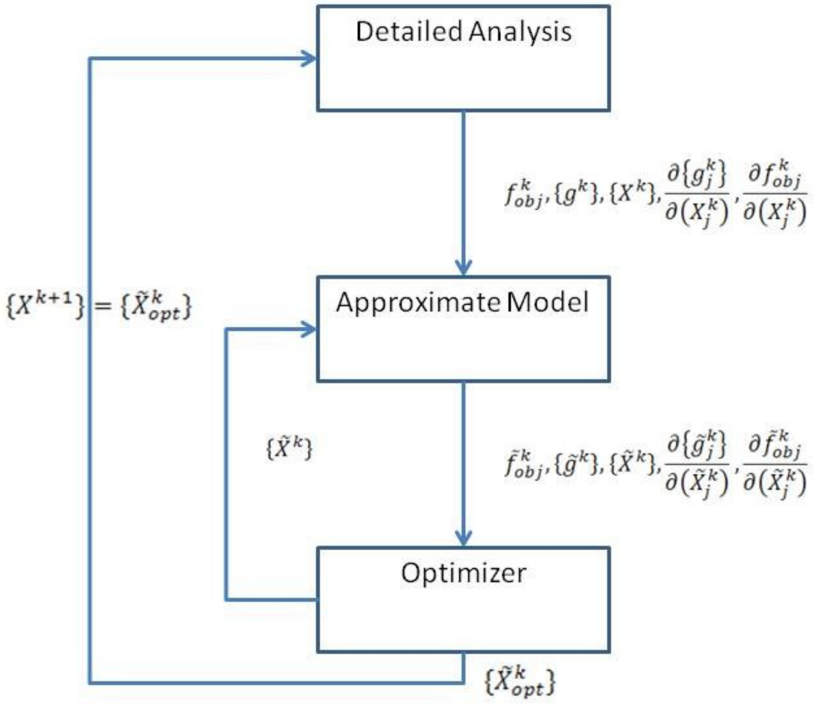

Figure 4-1: NLP/AC Process

4.2 Approximate Modeling

Various models can be used to approximate the nonlinear model being optimized. Here, models based on a Taylor Series approximation are employed. The traditional Taylor Series based approximation techniques are described in the following sections.

4.2.1 Direct Approximation

The direct approximation is essentially the traditional Taylor series approximation linearly expanded about the design variables. The direct technique approximates the objective function and constraints as follows.

$$f^a = f^e + \nabla f^{e^T}\{x - x^{ref}\} \tag{4.2}$$

$$g_j^a = g_j^e + \nabla g_j^{e^T}\{x - x^{ref}\} \tag{4.3}$$

$$\nabla f^a = \nabla f^e \tag{4.4}$$

$$\nabla g_j^a = \nabla g_j^e \tag{4.5}$$

4.2.2 Reciprocal Approximation

While the direct approximation is linear in the design variable, the reciprocal approximation takes the Taylor series expansion about the reciprocal of the design variables. Consider an optimization problem where the objective is to minimize weight of a bar element subject to stress and displacement constraints [13].

$$\begin{gathered} \min W = \rho A L \\ Subject\ to: \\ \sigma = \frac{P}{A} \leq \sigma_y \\ \delta = \frac{PL}{AE} \leq \delta_y \end{gathered} \tag{4.6}$$

The design variable in this case is only the area of the rod. It is noticed that the objective function is linear with the design variable, but the constraints are nonlinear. Performing a change of variables, an intermediate variable, X, is introduced.

$$X = \frac{1}{A} \tag{4.7}$$

The optimization problem can be re-written:

$$\min W = \frac{\rho L}{X}$$

$$\begin{gathered} Subject\ to: \\ \sigma = PX \leq \sigma_y \\ \delta = \frac{PLX}{E} \leq \delta_y \end{gathered} \tag{4.8}$$

Now, there is a nonlinear, but still explicit, function of the design variable and two constraints that are linear with the design variable X. Taking a first order Taylor Series expansion about these constraints creates a much better approximation to the actual constraint functions and one that can be calculated quickly and easily; hence, the reciprocal approximation may be a useful technique to employ when stresses and displacement are concerned.

In general, the reciprocal approximations for the objective function and constraints are expressed as:

$$f^a = f^e - \sum \left(X_i^2 \frac{\partial f}{\partial x_i} \right)_{\mathrm{ref}} \left(\frac{1}{\mathrm{X_i}} - \frac{1}{X_i^{ref}} \right) \tag{4.9}$$

$$g^a = g^e - \sum \left(X_i^2 \frac{\partial g_j}{\partial X_i} \right)_{ref} \left(\frac{1}{X_i} - \frac{1}{X_i^{ref}} \right) \tag{4.10}$$

$$\nabla f^a = \sum \left(X_i^2 \frac{\partial f}{\partial x_i} \right)_{\mathrm{ref}} \left(\frac{1}{\mathrm{X_i^2}} \right) \tag{4.11}$$

$$\nabla g^a = \sum \left(X_i^2 \frac{\partial g_j}{\partial X_i} \right)_{ref} \left(\frac{1}{\mathrm{X_i^2}} \right) \tag{4.12}$$

4.2.3 Hybrid Approximation

Since neither the direct nor the reciprocal method may be the sole best option for an optimization problem, the hybrid, or conservative, approximation provides an attempt to combine the two techniques. The hybrid approximation acts as follows: compare values of a direct approximation and a reciprocal approximation. Then use the more conservative value. From Reference [13] page 324:

$$\text{If} \qquad X_i \frac{\partial g(X^0)}{\partial X_i} \geq 0 \qquad \text{Use Direct Method}$$

$$\text{If} \qquad X_i \frac{\partial g(X^0)}{\partial X_i} < 0 \qquad \text{Use Reciprocal Method}$$

The plot in Figure 4-2 compares the reciprocal and direct methods and outlines the hybrid approximation method.

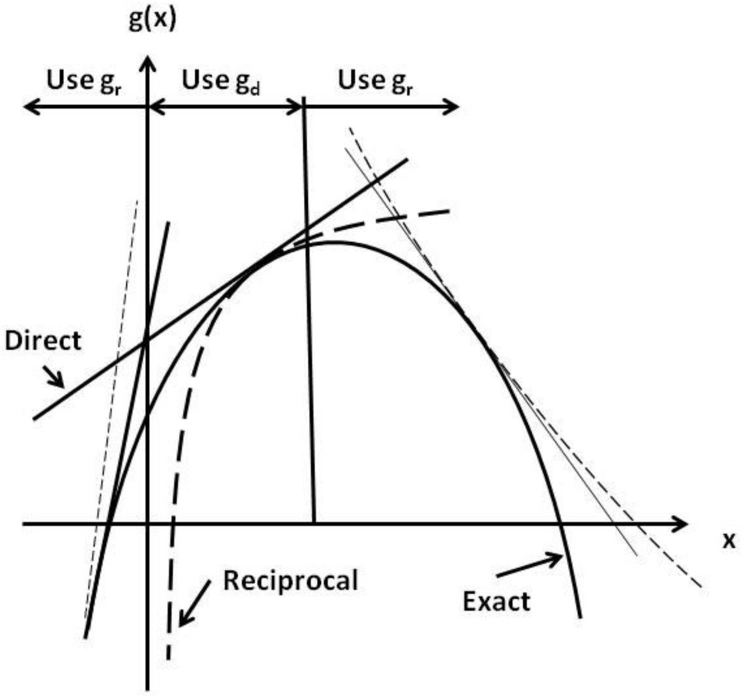

Figure 4-2: Direct, Reciprocal, and Hybrid Approximations [13]

An advantage of the hybrid method is that the approximate problem becomes convex, meaning that if a local minimum exists, it must be the global minimum; however, this assertion is true only for the approximate system. There is no guarantee that this conservative method will find a global minimum for the true nonlinear problem.

4.3 Optimization Method

The Matlab function `fmincon` is utilized to perform the optimization, which can handle both linear and nonlinear programming methods. In most cases, either the objective function or constraints will be nonlinear; however, for the direct method, both the objective and constraint functions are linear. The function `fmincon` is a constrained optimization utility that attempts to find a set of design variables, x, that will minimize the objective function subject to a set of nonlinear or linear constraints, or a combination of both, beginning with an initial guess, x_0. This function is highly customizable to allow the user to specify whether or not to supply the optimizer with sensitivities. The user may also specify other optimization options, such as tolerances and maximum number of iterations. The approximate function gradients are also fed into the `fmincon` function in order for them to be used in the optimization. Refer to the `fmincon` Matlab function reference page for a listing of the user specifications [16]. The numerical analysis algorithms used by `fmincon` are described in References [17]-[25].

4.4 Optimization Capability Testing

4.4.1 Truss with Stress Constraints

This optimization example begins with the 10-bar truss mentioned in Section 2.4.1. The objective is to minimize the mass of the structure subject to a 25 ksi (0.17 GPa) stress constraint on all members except for member 9, which has a stress constraint of 75 ksi (0.52 GPa). The structure begins with all areas being 5 in^2 ($3.23 \times 10^{-3} m^2$) with a minimum area constraint of

$0.1\ in^2\ (6.5 \times 10^{-5} m^2)$. The optimization was performed using direct, reciprocal, and hybrid approximations, and the results of these three methods are then compared. The direct and hybrid methods imposed 20% move limits on the design variables, while the reciprocal method used 10% move limits. Table 3 shows the optimal areas and optimal masses calculated from each approximation method, and these results are compared to those given by Reference [12]. The following figures graphically depict the evolution of the objective function and constraints for each approximation method used.

Table 3: Results for Truss Structure with Stress Constraints

	Reference [12]	Direct	Reciprocal	Hybrid
A_1 (in^2)	7.90	7.90	7.92	7.86
A_2 (in^2)	0.10	0.10	0.10	0.14
A_3 (in^2)	8.10	8.10	8.08	8.14
A_4 (in^2)	3.90	3.90	3.92	3.86
A_5 (in^2)	0.10	0.10	0.10	0.10
A_6 (in^2)	0.10	0.10	0.10	0.14
A_7 (in^2)	5.80	5.80	5.77	5.86
A_8 (in^2)	5.51	5.51	5.54	5.46
A_9 (in^2)	3.68	3.68	3.69	3.64
A_{10} (in^2)	0.14	0.14	0.11	0.18
Mass (lbm)	1,514	1,497	1,498	1,500

The mass calculation at each iteration (each time an approximate model is formulated) is plotted in Figure 4-3. A total of 14 calls to the detailed ("exact") truss model were needed for convergence.

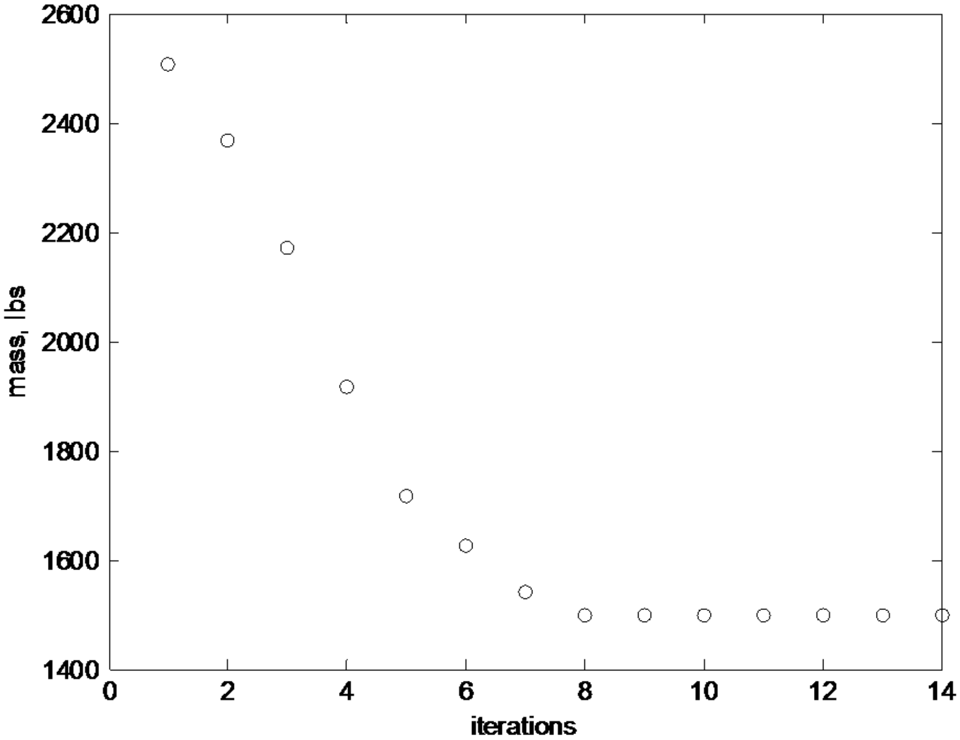

Figure 4-3: Mass of the Structure, Direct Method

Figure 4-4 depicts the evolution of the ten design variables as a function of iteration. As shown in Table 3, elements 2, 5, 6, and 10 come near or reach the lower limit of 0.1in^2.

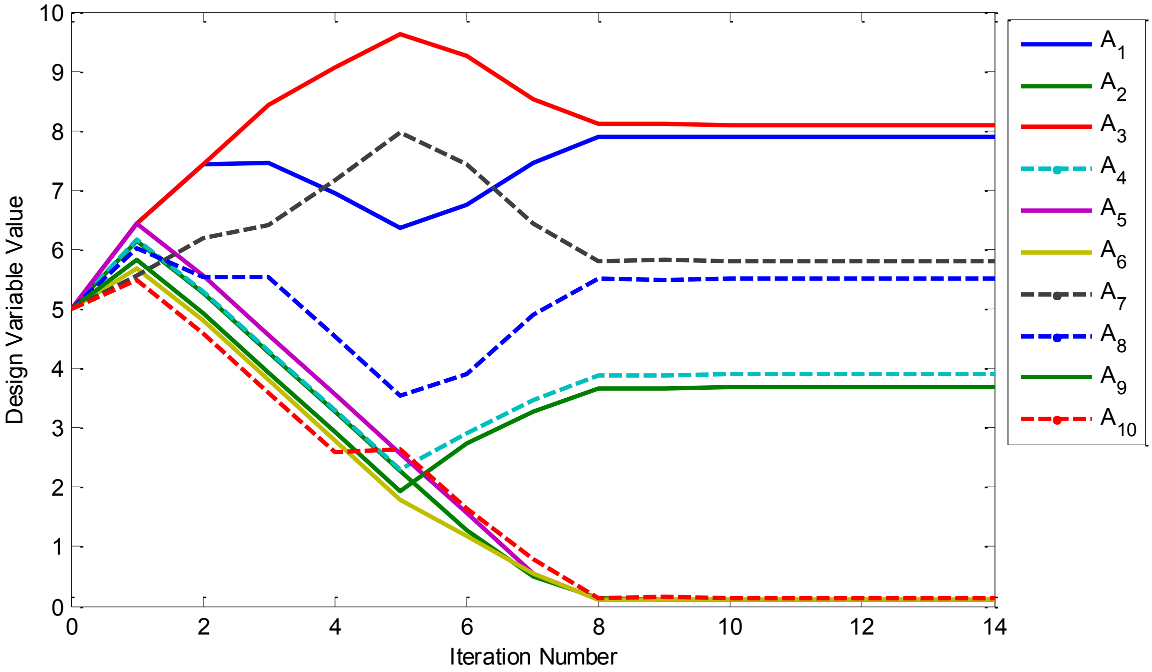

Figure 4-4: Design Variable Progression, Direct Method

Figure 4-5 depicts the constraint values for tensile stress in each truss member. It is observed that constraints values for elements 1, 2, 6, 7, and 9 are tight, where the value becomes close to or equal to zero; as a result, these constraints are driving the optimization.

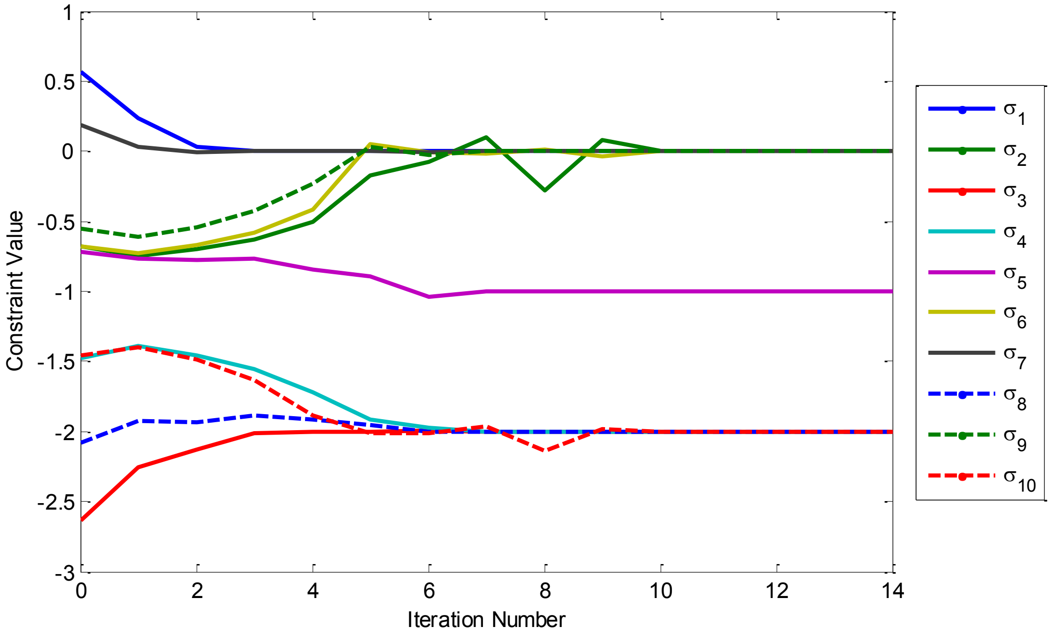

Figure 4-5: Tensile Stress Constraints, Direct Method

Figure 4-6 illustrates the compressive stress constraint values as a function of iteration. The constraint values for elements 3, 4, 8, and 10 are also included in the list of tight constraints.

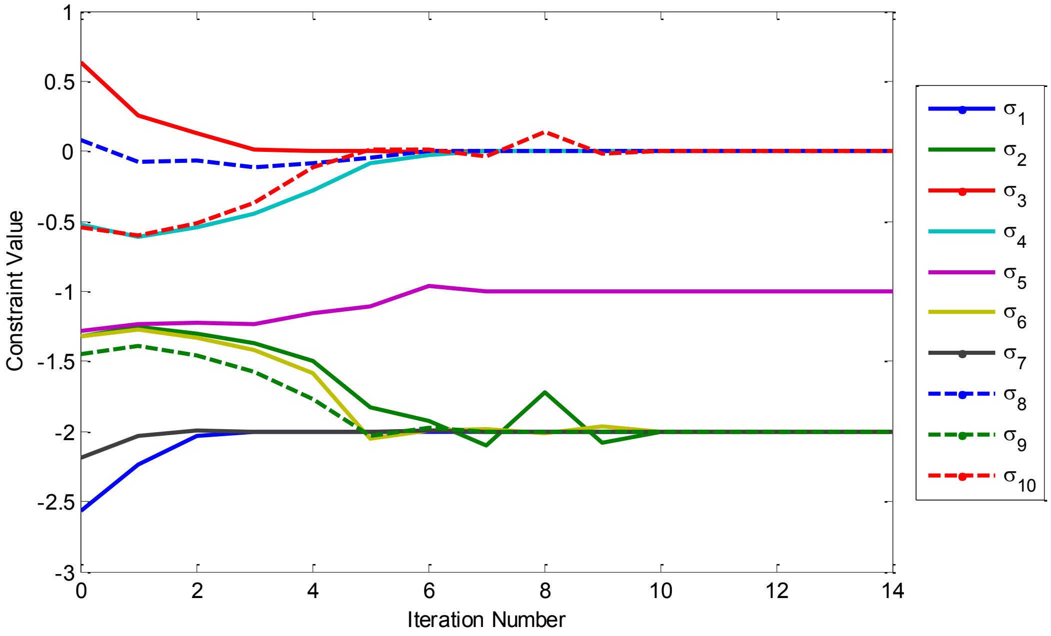

Figure 4-6: Compressive Stress Constraints, Direct Method

As will be noticed in subsequent constraint function plots, the constraints that converge to a value of -2 are a result of the assumption that $\sigma_{yield_{compression}} = -\sigma_{yield_{tensile}}$. For example, the tensile stress in element number 6 approaches zero, or becomes tight. Recalling the expression for a stress constraint from Eq (3.17):

$$g_{\sigma_{comp}} = -\frac{\sigma}{|\sigma_{y_{comp}}|} - 1 \leq 0 \tag{4.13}$$

If σ approaches the tensile yield stress, the ratio of stress to compressive yield stress becomes -1, yielding a constraint function value of -2.

Overall, the direct method provided a quick convergence for the optimization problem; however, of the three methods, the direct approximation method provided the least accurate result when compared with Haftka and Gurdal's work. In this example, the direct approximation still provided an acceptable answer for the optimum, but it is obvious that this method could fail for highly nonlinear problems.

The reciprocal approximation was next applied to the truss optimization problem. Convergence using this method took longer than for the direct method, ending after 22 iterations; however, since the model used in this example is not highly complex, the longer computation time was not a noticeable detriment. The objective function progression is chronicled in Figure 4-7.

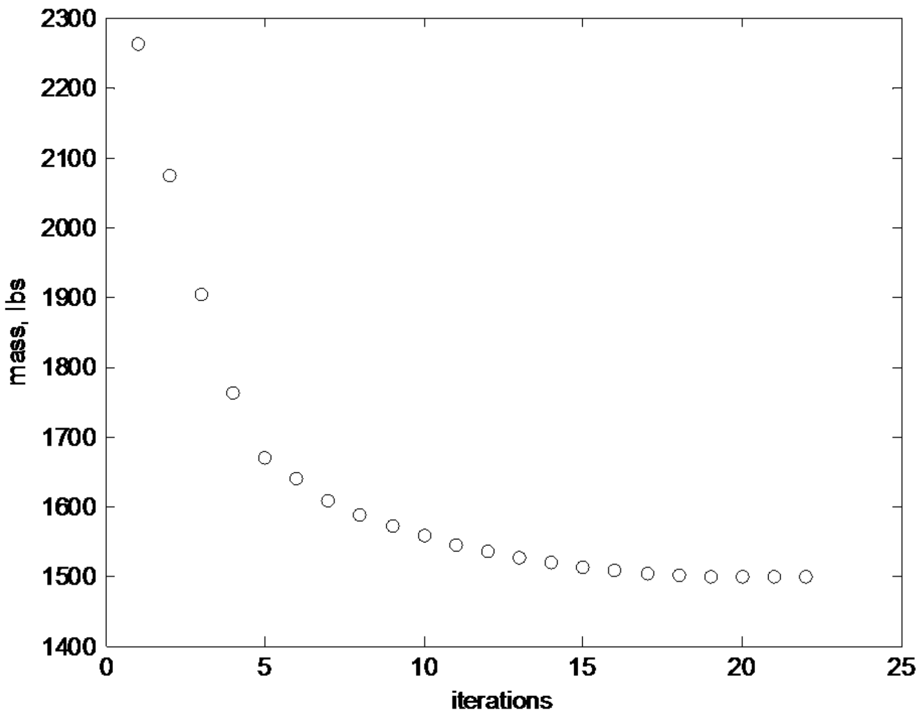

Figure 4-7: Mass of the Structure, Reciprocal Method

The design variable progression is expressed in Figure 4-8. In this case, nearly all of the design variables took approximately 20 iterations to converge to their final values, twelve iterations longer than what was produced by the direct approximation. The progression using the reciprocal method is also quite smooth, indicating that each optimization resulted in a set of numbers fairly close to the result from the previous iteration. This observation is most likely a result of the more stringent move limits imposed on the reciprocal approximation.

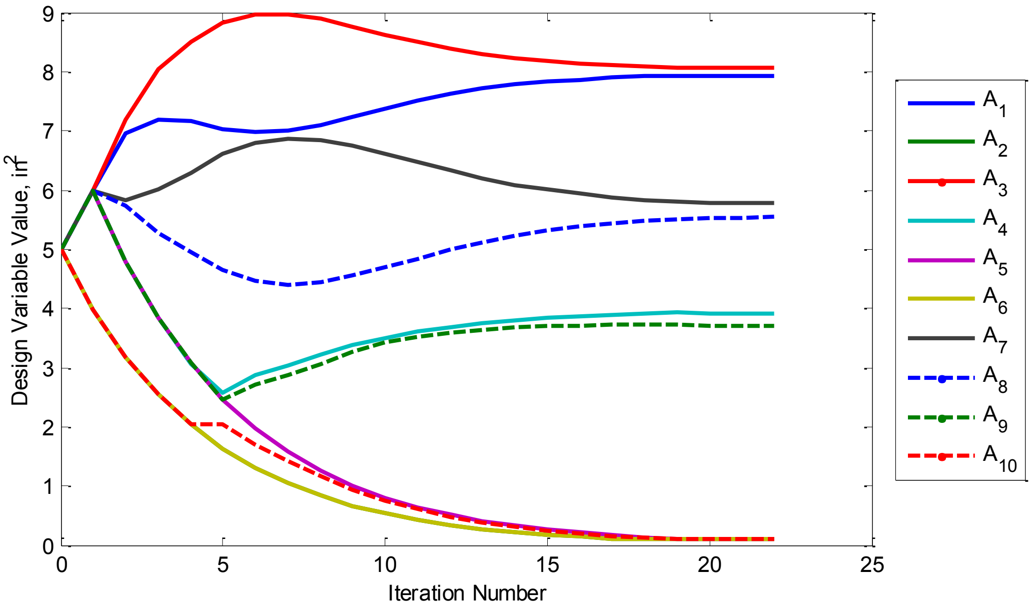

Figure 4-8: Design Variable Progression, Reciprocal Method

Figure 4-9 and Figure 4-10 showcase the tensile and compressive constraint values, respectively. For this optimization problem, the constraints that drive the optimization are tensile stress for elements 1, 7, and 9 and compressive stress for elements 3, 4, 8, and 10. The reciprocal method, therefore, resulted in fewer tight constraints than the direct method.

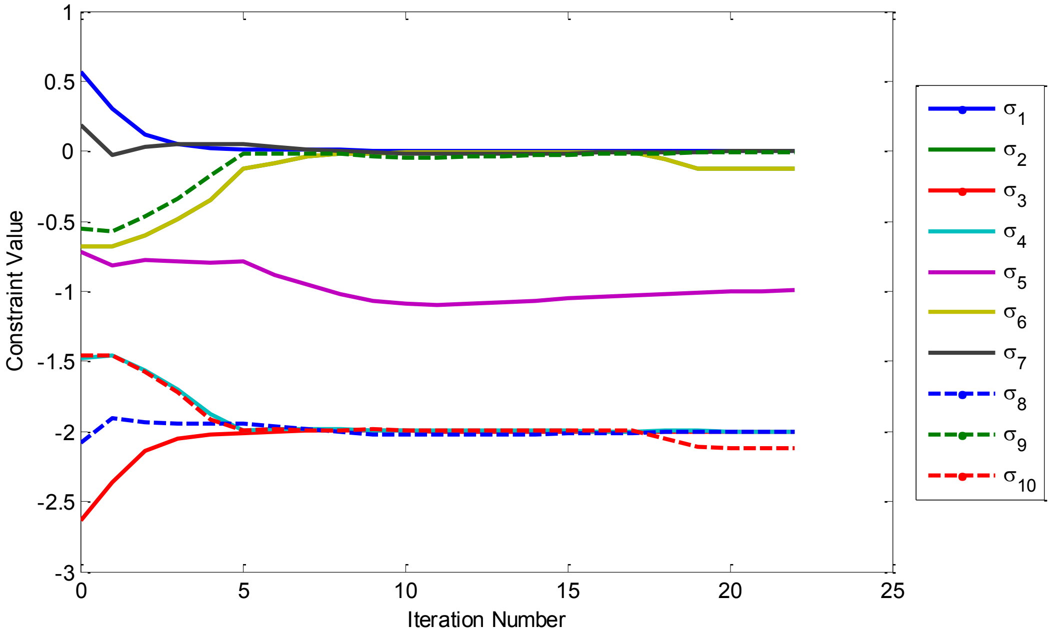

Figure 4-9: Tensile Stress Constraints, Reciprocal Method

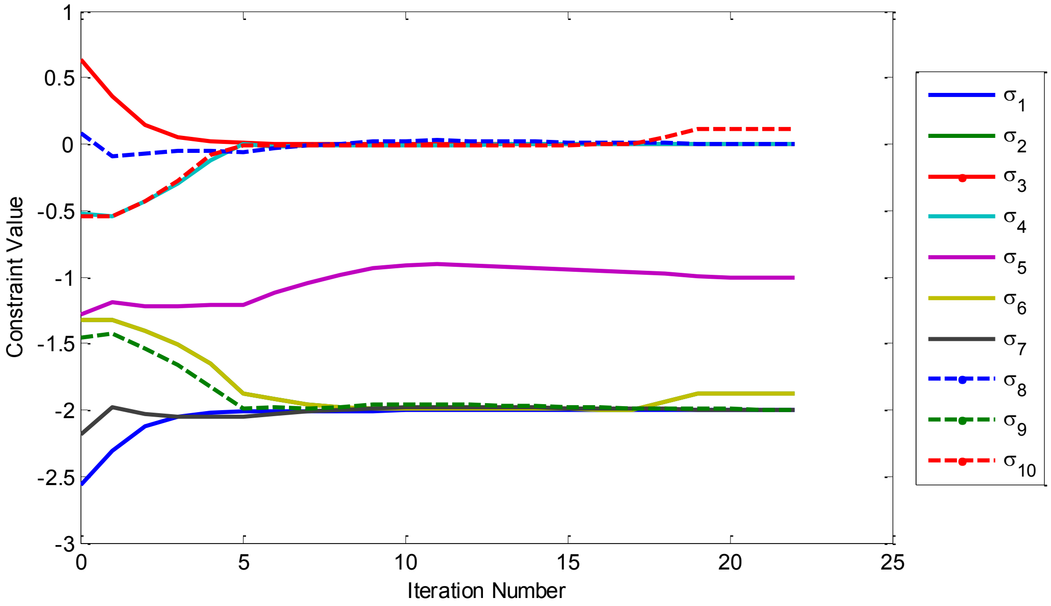

Figure 4-10: Compressive Stress Constraints, Reciprocal Method

The optimization using the reciprocal approximation method converged later than the direct approximation and also only produced an optimal mass that was one pound closer to the result from Haftka and Gurdal; therefore, given a choice for this example, the direct method is probably the more desirable method of the two.

Lastly, the most conservative method, the hybrid method, was implemented. The method's conservatism that comes with a price of possible inaccuracy is evident in Figure 4-11, which shows the progression of the objective function. Taking 70 iterations to converge to an optimum, this optimization took significantly longer than the direct and reciprocal approximation approaches in this test case.

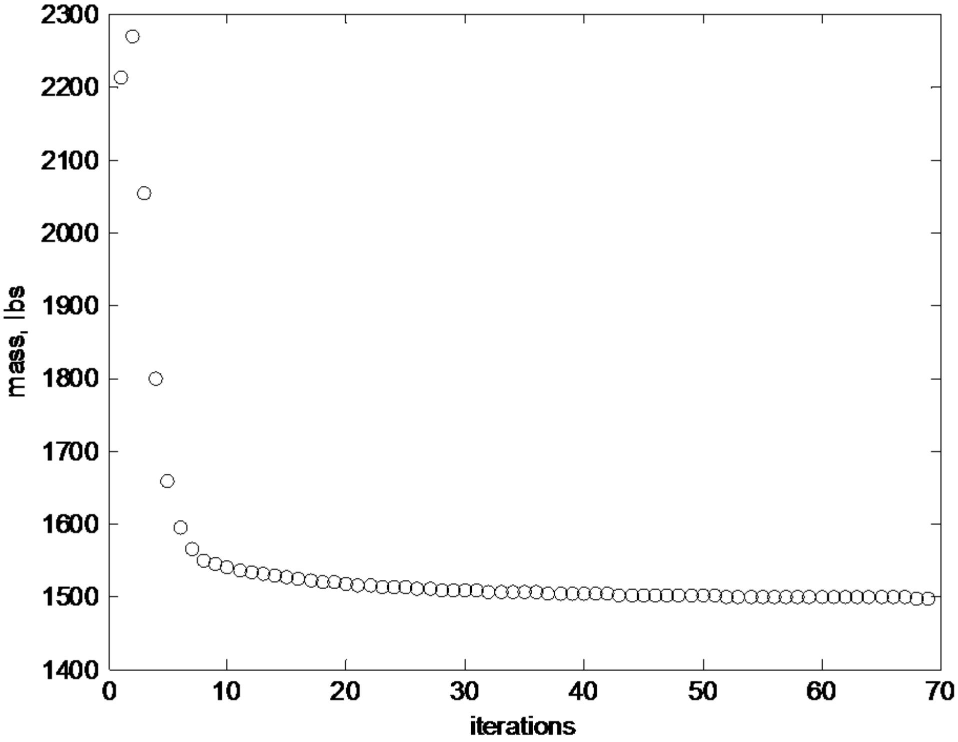

Figure 4-11: Mass of the Structure, Hybrid Method

The design variable evolution is shown in Figure 4-12. The first ten iterations produce some abrupt changes in design variable value, but the remaining 60 iterations serve to fine-tune the values.

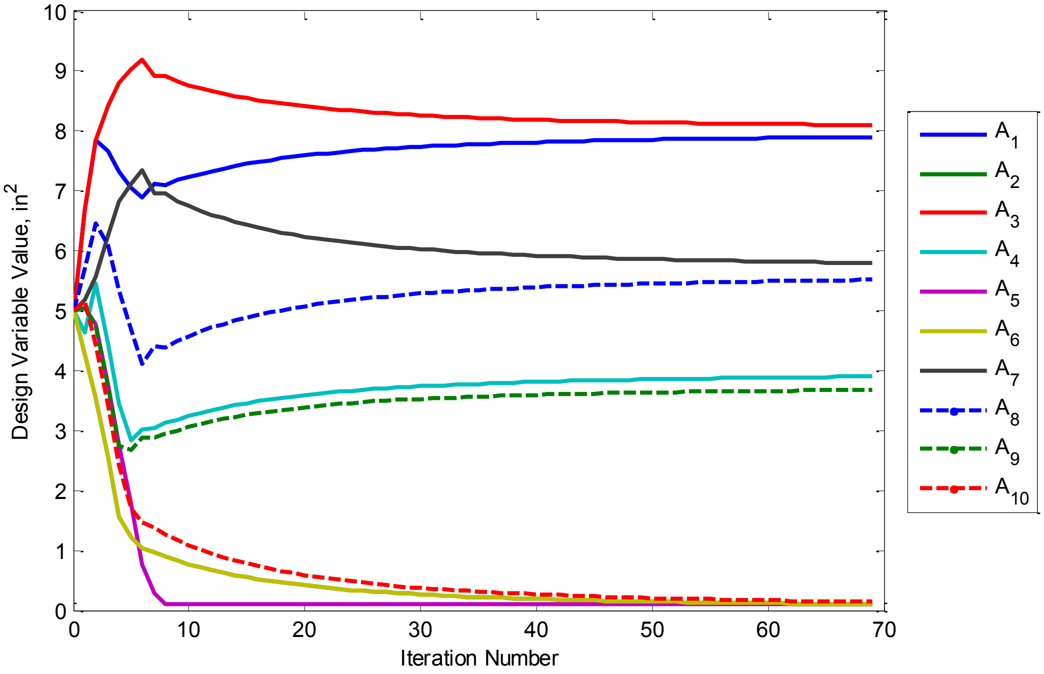

Figure 4-12: Design Variable Progression, Hybrid Method

The constraint values as a function of iteration are shown in Figure 4-13 and Figure 4-14. Like the progression of the design variables, the values essentially converge by the tenth iteration, but the hybrid method continues to fine-tune the results until overall convergence is reached. The eight tight constraints include tensile stress for elements 1, 2, 6, and 7 and compressive stress for elements 3, 4, 8, and 10. The identity of the tight constraints remained nearly constant through the usage of all three approximation methods.

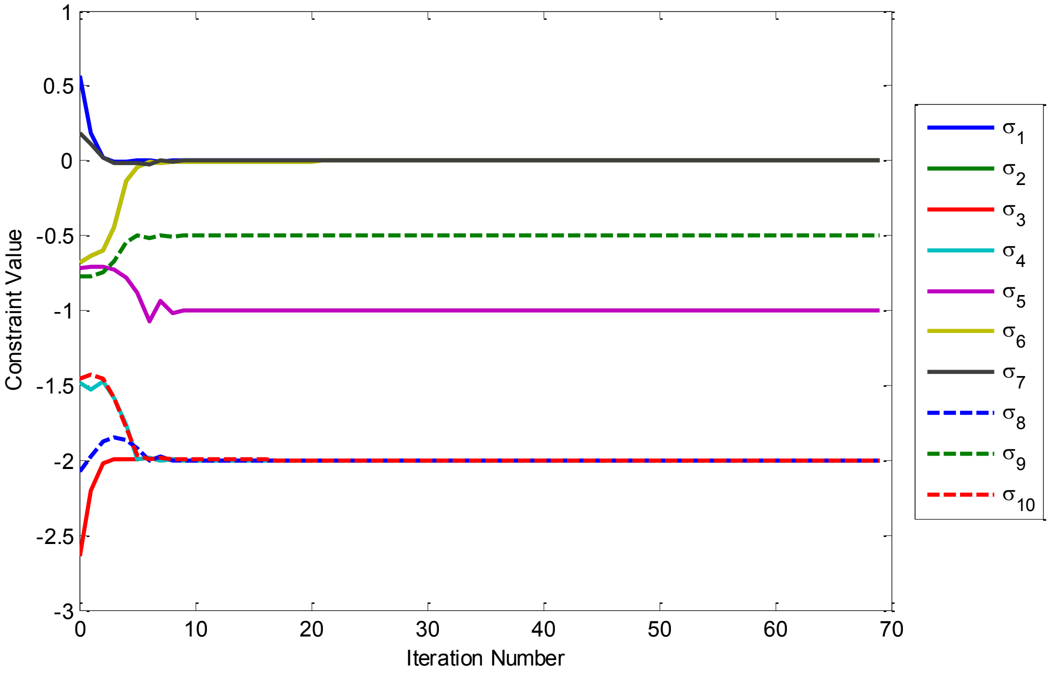

Figure 4-13: Tensile Stress Constraints, Hybrid Method

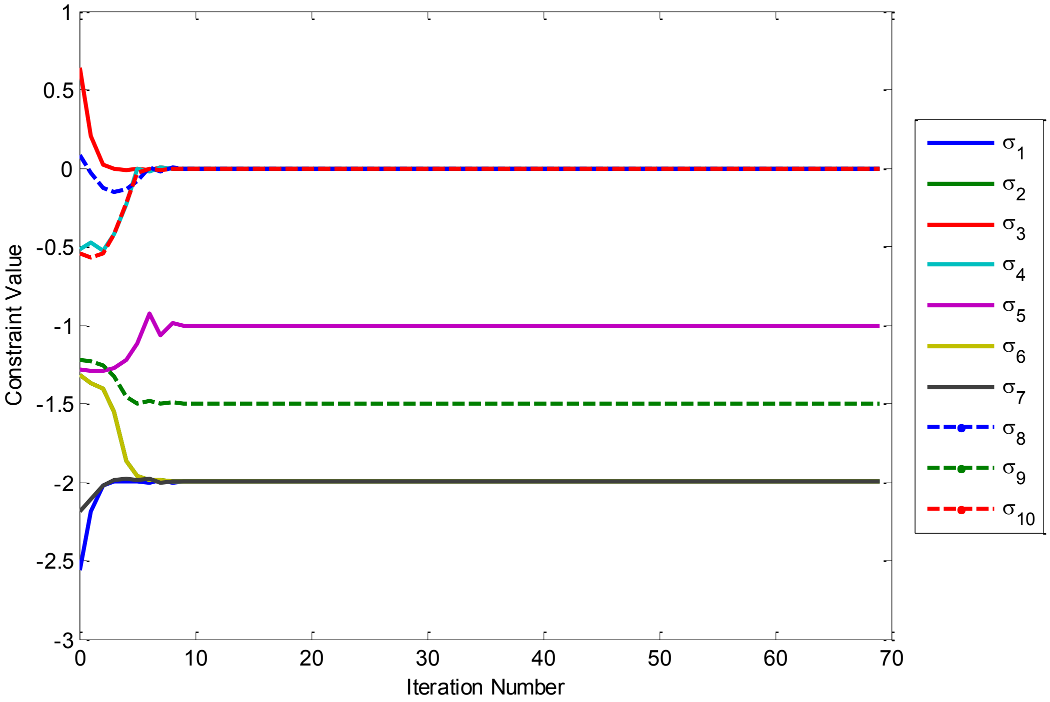

Figure 4-14: Compressive Stress Constraints, Hybrid Method

Of the three methods, the direct approximation approach provided the quickest convergence and also produced an acceptable optimal structural mass and number of tight constraints compared with the other approximation methods; as a result, the direct method is likely the most desirable method for this example. Note that this conclusion is limited to this case.

4.4.2 Truss with Displacement Constraints

The mass of the truss in this case is then minimized subject to the same stress constraints as in the previous section as well as two sets of displacement constraints. The displacement specifications for case A and case B are displayed in Table 4.

Table 4: Displacement Limits

Case	Node	Direction	Displacement Lower Limit	Displacement Upper Limit
A	1	Y	-2.0	-2.0
	3	Y	-1.0	-2.0
B	1-4	Y	-2.0	+2.0

Again, the direct, reciprocal, and hybrid methods were used to approximate the objective and constraint functions. For all approximation methods, move limits of 20% were imposed.

Table 5 shows the optimal areas and masses for displacement cases A and B for all three methods.

Table 5: Results for Case A and B

	Case A				Case B			
	Direct	Reciprocal	Hybrid	Ref [12]	Direct	Reciprocal	Hybrid	Ref [12]
A_1	20.49	20.96	20.96	22.66	31.27	30.93	30.73	30.52
A_2	1.62	1.04	1.04	1.40	0.10	0.10	0.10	0.10
A_3	21.28	22.15	22.16	21.58	21.53	22.46	23.94	23.20
A_4	8.05	8.03	8.03	8.43	14.84	15.25	14.73	15.22
A_5	0.10	0.10	0.10	0.10	0.10	0.10	0.10	0.10
A_6	0.10	0.10	0.10	0.10	0.22	0.96	0.10	0.55
A_7	12.84	12.63	12.63	12.69	6.85	6.80	7.54	7.46
A_8	14.10	13.97	13.97	14.54	21.30	21.83	20.95	21.04
A_9	10.57	11.28	11.28	11.93	21.95	21.57	20.84	21.53
A_{10}	2.06	1.30	1.30	1.98	0.10	0.10	0.10	0.10
Mass (lbm)	3,996	4,002	4,003	4,049	4,955	5,020	5,077	5,061

Figure 4-15 through Figure 4-17 show the progressions of the mass through the optimization process for case A. For this case, the active constraints for all three methods remained the same: constraint numbers 7, 9, and 19. All three of these constraints correspond to stresses in the elements (tensile stress in elements 7 and 9 and compressive stress in element 9).

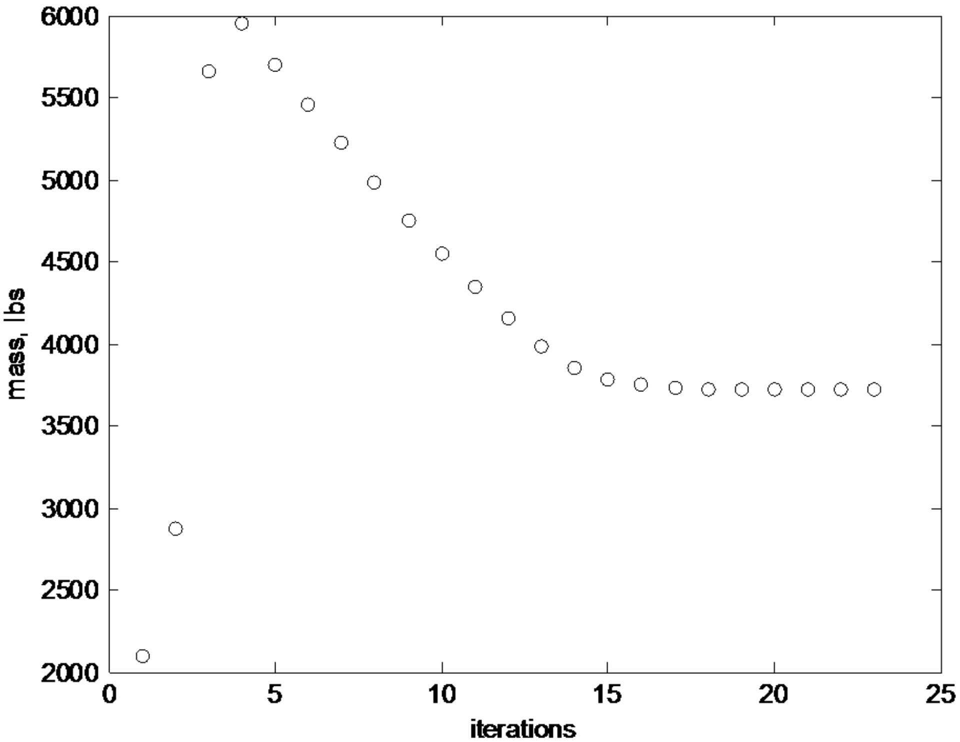

Figure 4-15: Mass Progression for Direct Method: Case A

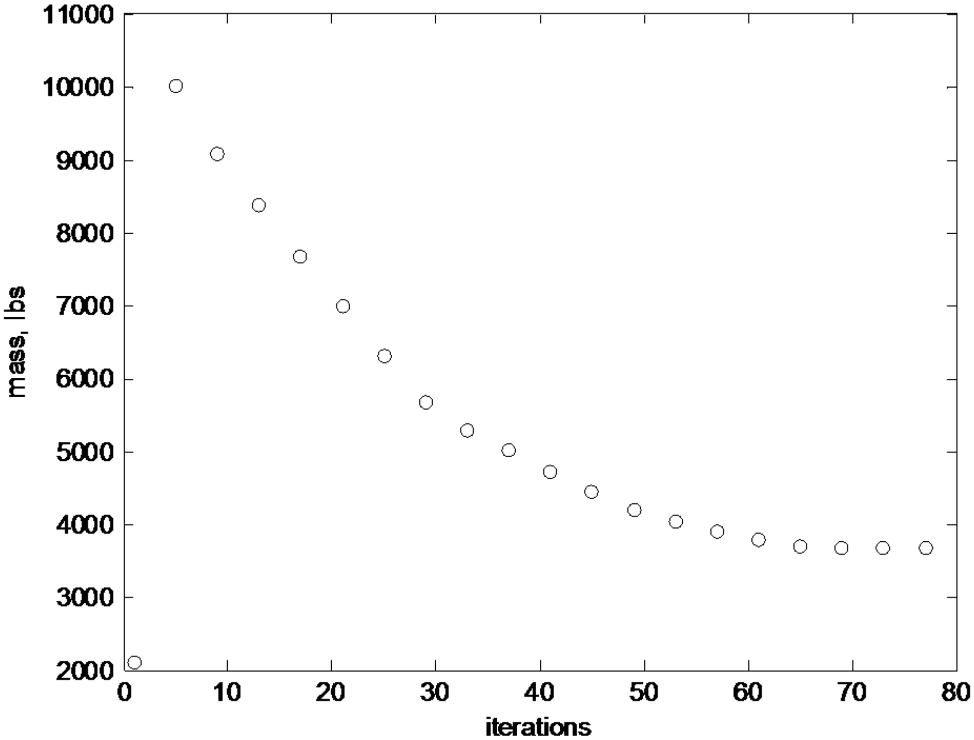

Figure 4-16: Mass Progression for Reciprocal Method: Case A

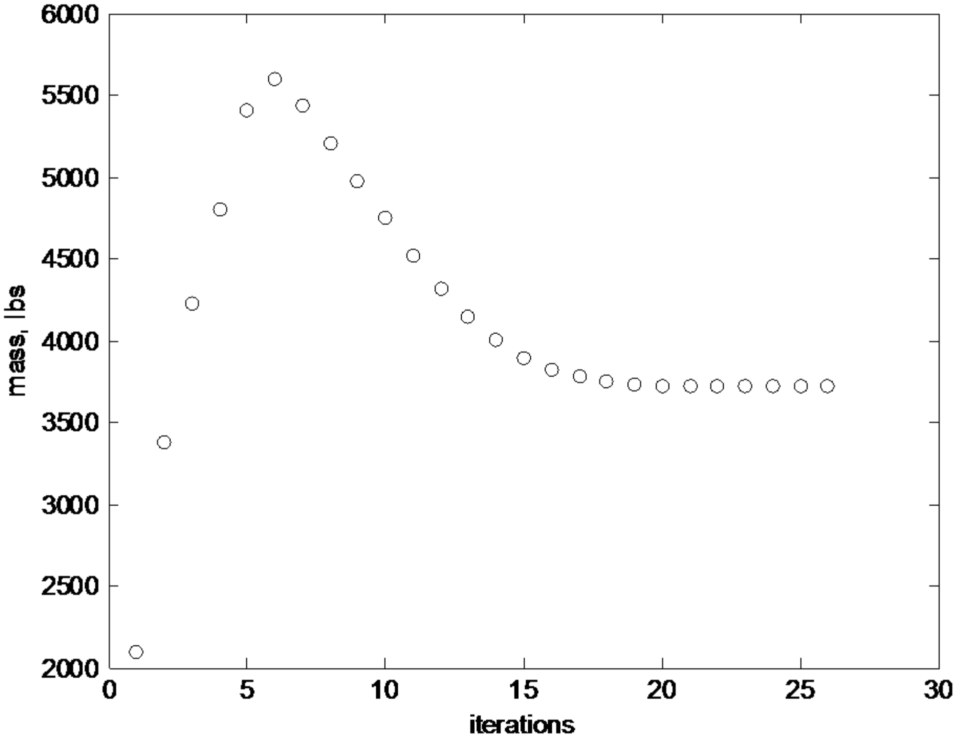

Figure 4-17: Mass Progression for Hybrid Method: Case A

Overall for case A, the direct method converged to slightly smaller areas than the hybrid and reciprocal approximations calculated, leading to a lighter optimized structural mass. While the direct and hybrid methods converged in approximately 25 iterations, the reciprocal did not converge until close to 80 iterations.

Figure 4-18 through Figure 4-20 display the mass progression results for case B. Using the direct method, the tight constraints were for compressive stress in elements 9 and 10 and lower displacement for node 2; the reciprocal method produced tight constraints for compressive stress in element 9 and lower displacement for element 2; and lastly, the hybrid method's tight constraints were compressive stress for elements 9 and 10.

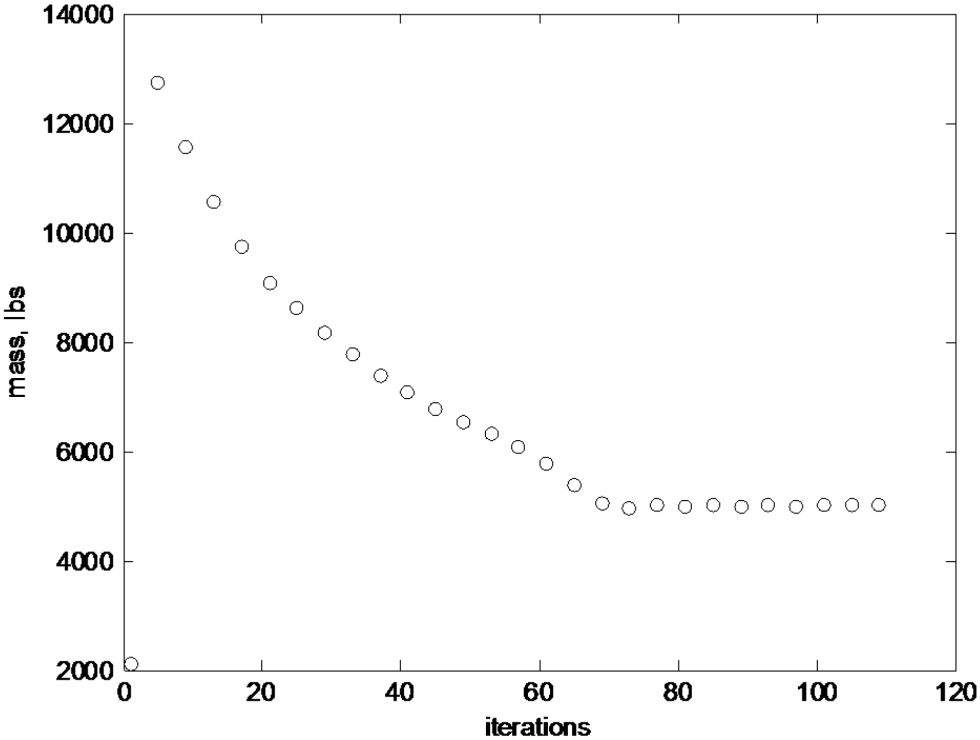

Figure 4-18: Mass Progression for Direct Method: Case B

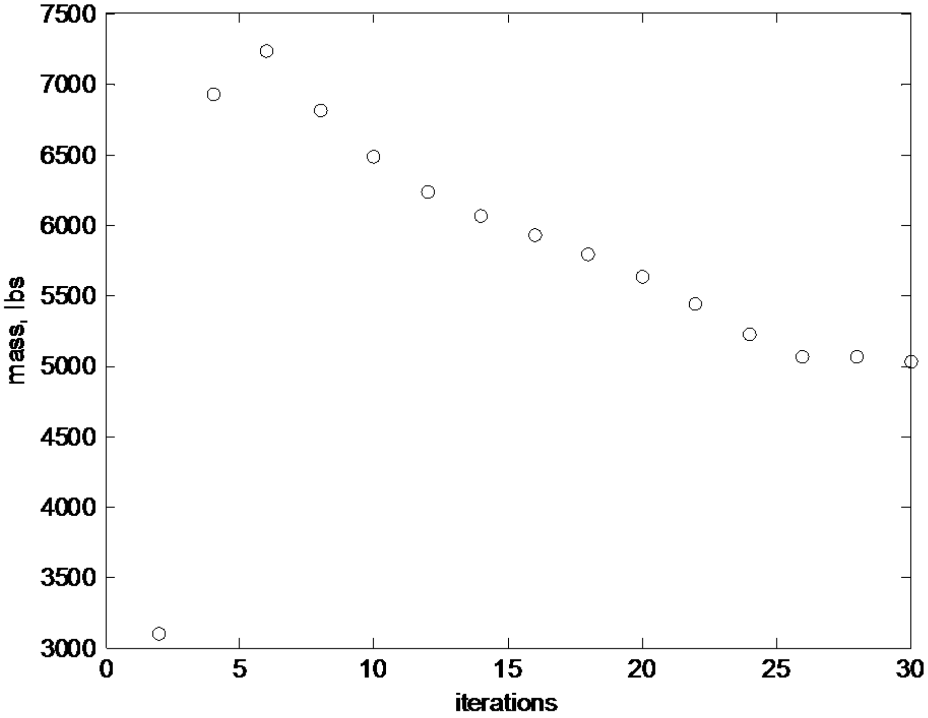

Figure 4-19: Mass Progression for Reciprocal Method: Case B

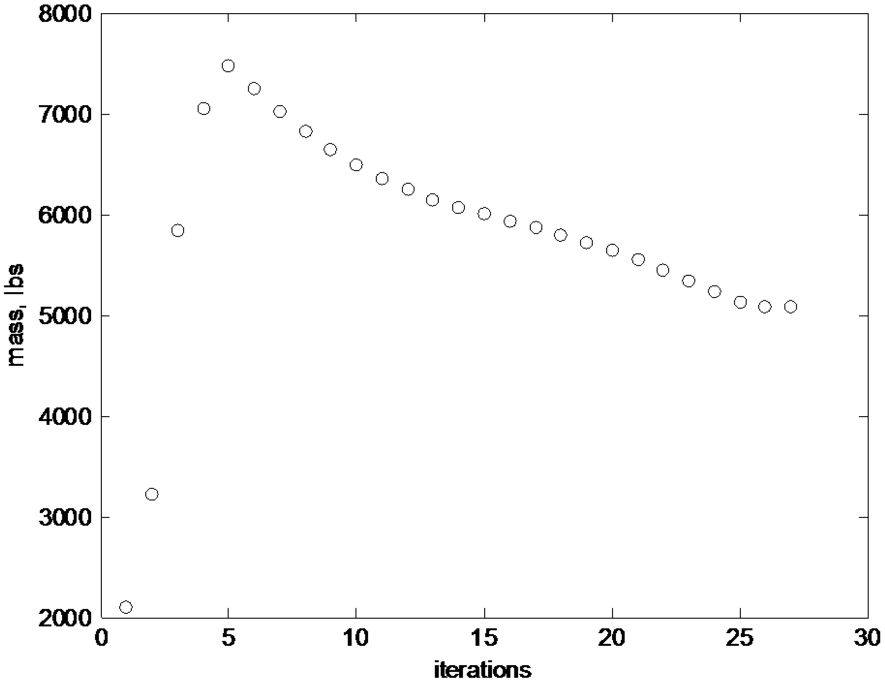

Figure 4-20: Mass Progression for Hybrid Method: Case B

In this case, the direct method was the undesirable approximation method in terms of computation time, converging in over 100 iterations, while the reciprocal and hybrid optimizations converged after about 30 iterations. The optimizations produced fairly close objective function values, resulting in masses that ranged from 98.7-98.9% of the results from Reference [12] for case A and 97.9-100.3% for case B.

5 Strain-Based Optimization Example

5.1 Strain-actuated truss Background

The aforementioned optimization method is exercised on a truss with shape memory alloy actuation. The truss is 48 inches (1.219 meters) long, 10 inches (0.254 meters) high, and it is cantilevered at one end of the structure. The truss includes 12 aluminum rod elements for caps and 12 shape memory alloy diagonal truss elements for actuation. The system has 84 degrees of freedom when including x, y, and z directions as well as rotational motion; however, the number of degrees of freedom reduce to 24 when restricting the motion in the x-y plane and eliminating rotational motion. Six forces are distributed over the bottom nodes of the structure, pulling in the negative y direction, with a magnitude of 44,500N each, approximately 10,000 pounds. The SMA is also initially heated 5°C over the ambient -35°C temperature. A schematic of this truss is shown in Figure 5-1.

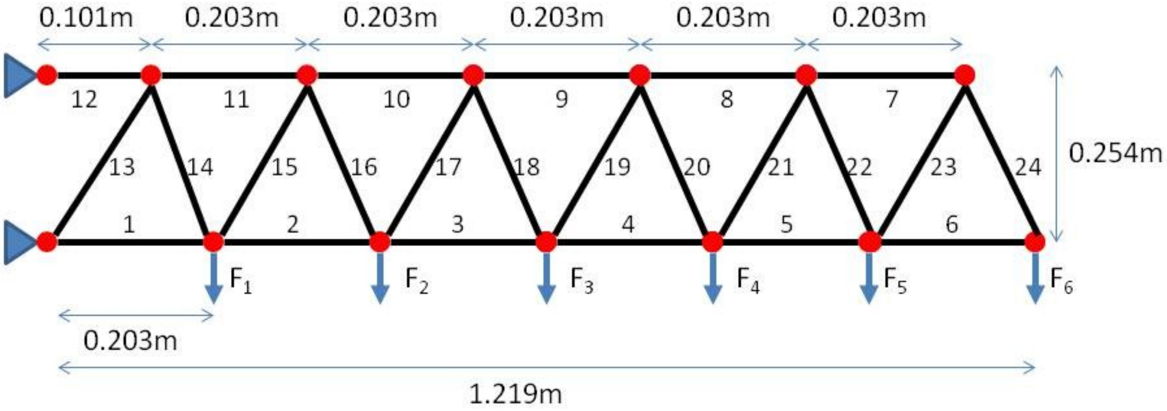

Figure 5-1: Truss Schematic

The initial deformation of the structure, caused by the forces and SMA heating, are shown in Figure 5-2.

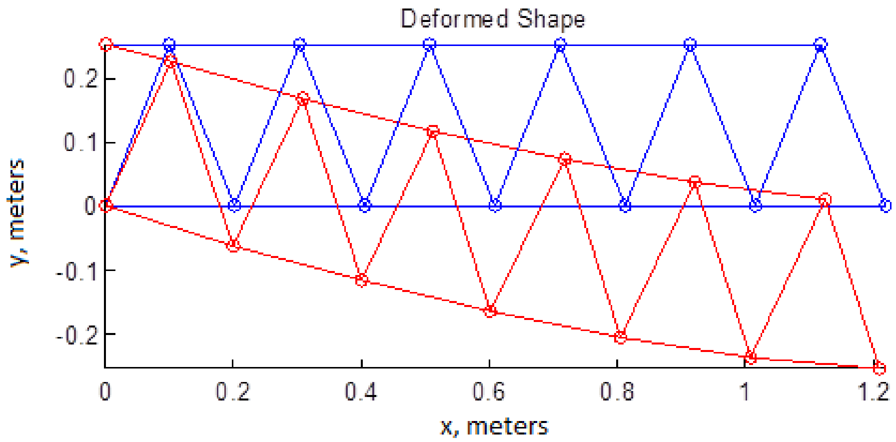

Figure 5-2: Strain-Based Truss Initial Deformation

The SMA material is the same copper-based SMA specified by Liang and Rogers, with properties shown in Table 2.

The aluminum elements are all solid cylinders, while the SMA actuators have a hollow cross section to accommodate a non load carrying rod with temperature controls. The mass of these heating rods are assumed to be massless for this study or to not contribute to the overall mass of the structure. The initial diameters for the aluminum elements and outer diameters of the SMA actuators were all set at 0.0287m, or 1.13 inches. It is assumed that the ratio of the inner diameter, d_i and the outer diameter, d_o, for the diagonal elements is constant throughout the optimization and is defined as the Greek letter η. In this exploratory study, this ratio was set at 0.3.

To protect against failure, the stresses in each element must be less than the yield stresses, σ_y, for each material in compression and in tension. In this example, the tensile yield stresses for all elements were set at 25 ksi (0.17 GPa), and the compressive yield stresses were -25ksi. Assuming σ_y as a positive number, then for tension, the following must be true for each element of the structure.

$$\sigma \leq |\sigma_y| \tag{5.1}$$

Normalizing this constraint results in the constraint function in Eq (5.2).

$$g_{\sigma_{tens}} = \frac{\sigma}{\sigma_y} - 1 \leq 0 \tag{5.2}$$

Similarly for compression:

$$\sigma \geq -|\sigma_y| \tag{5.3}$$

$$g_{\sigma_{comp}} = \frac{-\sigma}{|\sigma_y|} - 1 \leq 0 \tag{5.4}$$

When truss elements are in compression, it is also necessary to guard against Euler buckling. For a pinned-pinned beam of length L and cross sectional moment of inertia I with a load P acting in compression, buckling will occur when the compressive load becomes larger than $\frac{\pi^2 EI}{L^2}$; therefore, the constraint must be as expressed in Eq (5.5).

$$|P| \leq \frac{\pi^2 EI}{L^2} \tag{5.5}$$

Rewriting in terms of compressive stress:

$$|\sigma| \leq \frac{\pi^2 EI}{L^2} \frac{1}{A} \tag{5.6}$$

If the traditional sign convention is used, with positive stresses being in tension and negative stresses being in compression, then for each element, the relation expressed in Eq (5.7) is needed.

$$\sigma \geq -\frac{\pi^2 EI}{L^2}\frac{1}{A} \tag{5.7}$$

Using the diameter specifications for the aluminum rods, the area of each cap element is therefore:

$$A = \frac{\pi d^2}{4} \tag{5.8}$$

For a circular cross section, the moment of inertia is:

$$I = \frac{\pi d^4}{64} \tag{5.9}$$

Therefore, the ratio of inertia to area can be expressed.

$$\frac{I}{A} = \frac{d^2}{16} \tag{5.10}$$

The area of a hollow circular cross section is:

$$A = \frac{\pi}{4}\left(d_o^2 - d_i^2\right) \tag{5.11}$$

Eq (5.11) can then be written to be in terms of η.

$$A = \frac{\pi}{4} d_o^2 (1 - \eta^2) \tag{5.12}$$

Similarly, the moment of inertia is:

$$I = \frac{\pi}{64} d_o^4 (1 - \eta^4) \tag{5.13}$$

Therefore, the ratio of inertia to area can be calculated.

$$\frac{I}{A}=\frac{1}{16}d_o^2(1+\eta^2) \tag{5.14}$$

Taking the stress constraint in Eq (5.7) and information for a solid circular cross section leads to the constraint function in Eq (5.15).

$$g_{\sigma_{buck}}=-\sigma\left(\frac{16\mathrm{L}^2}{\pi^2\mathrm{Ed}^2}\right)-\ 1\leq 0 \tag{5.15}$$

Similarly, for a hollow cross section, the buckling stress constraint function is:

$$g_{\sigma_{buck}}=-\sigma\left(\frac{16\mathrm{L}^2}{\pi^2\mathrm{Ed}_\mathrm{o}^2(1+\eta^2)}\right)-\ 1\leq 0 \tag{5.16}$$

It is also desired to force the upper and lower cap nodes to move to create a certain shape, designated by $y_{upper}(x)$ and $y_{lower}(x)$ to within some root mean square global error, ϵ, which was set to 0.001m in this case. This error is expressed in Eq (5.17), where C is the number of cap nodes in the structure.

$$\frac{\sqrt{\sum_{i=1}^{C}\left(y_{node_i}-y_{node_{i_{desired}}}\right)^2}}{C}\leq\epsilon \tag{5.17}$$

The above relation can be expressed as a normalized constraint as in Eq (5.18).

$$g_{shape}=\frac{\sqrt{\sum_{i=1}^{C}\left(y_{node_i}-y_{node_{i_{desired}}}\right)^2}}{C\epsilon}-1\leq 0 \tag{5.18}$$

For this optimization problem, it was desired to force the structure back to its initial state; therefore, the desired deformation in the y-direction was zero for all nodes.

The optimization problem will also impose side constraints on the size of the temperature change in the SMA material to be between 0℃ and 20ºC, heating or cooling. Since diameters cannot be equal to zero, a lower limit of 6.5×10^{-5}m was placed on the diameter design variable.

The objective of this optimization will be to minimize total mass of the structure while ensuring that there exist no stress failures nor Euler buckling and that the structure conforms to the desired shape as closely as possible within the given temperature constraints; therefore, the optimization problem is expressed as:

$$\min \sum_{i=1}^{N_{elements}} \rho_i A_i L_i$$

$$\begin{gathered} \text{Subject to} \\ g_\sigma \leq 0 \\ g_{\sigma_{buck}} \leq 0 \\ g_{shape} \leq 0 \\ 0 \leq |\Delta T| \leq 20℃ \\ 6.5 \times 10^{-5} \leq d \leq 0.1 \text{ m} \end{gathered} \tag{5.19}$$

The design variables of this problem are diameter of each aluminum cap element, outer diameter of each hollow SMA element, and temperature difference needed for the SMA actuators. The inner diameters of the SMA elements will then be calculated from the outer diameters by using the preassigned ratio η. Convergence was defined to be when the objective function value came within 1% of the previous iteration's value and that all constraints were satisfied.

5.2 Approximation Validation and Sensitivities

The buckling stress constraint function for a closed circular section is displayed in Eq (5.20).

$$\sigma \geq -\frac{\pi^2 E}{L^2}\frac{d^2}{16} \tag{5.20}$$

Noticing that everything except for diameter is constant, the buckling stress constraint can be re-written with an overall constant, C, as shown in Eq (5.21).

$$\sigma \geq -Cd^2 \tag{5.21}$$

Normalizing:

$$-\frac{\sigma}{Cd^2} - 1 \leq 0 \tag{5.22}$$

Therefore, the buckling stress constraint is proportional to the reciprocal of d^2.

For the diameter design variable, it is noticed that a better approximation technique than direct or reciprocal can be developed for the buckling stress relationships. The same conclusion can be drawn about the stress constraint. Since stress and buckling stress constraints are both proportional to $\frac{1}{d^2}$, the "reciprocal squared" method was derived.

For a buckling stress constraint, the reciprocal squared approximation is written as a Taylor Series expansion in Eq (5.23).

$$g_{\sigma_{buck_{approx}}} = g_{\sigma_{buck_0}} + \left.\frac{\partial g_{\sigma_{buck_{approx}}}}{\partial y}\right|_0 (y - y_0) \tag{5.23}$$

Where $y = \frac{1}{d^2}$.

The derivative of buckling stress constraint with respect to the intermediate variable, $y = \frac{1}{x^2}$, can be calculated using the chain rule.

$$\frac{\partial g_{\sigma_{buck_{approx}}}}{\partial y} = \frac{\partial g_{\sigma_{buck_{approx}}}}{\partial x}\frac{\partial x}{\partial y} \tag{5.24}$$

Since $y = \frac{1}{x^2}$:

$$\frac{\partial x}{\partial y} = -\frac{1}{2}\mathrm{x}^3 \tag{5.25}$$

Plugging Eq (5.24) into Eq (5.23) yields the reciprocal squared approximation.

$$g_{\sigma_{buck_{approx}}} = g_{\sigma_{buck_0}} - \frac{1}{2}\mathrm{x}_0^3 \left.\frac{\partial g_{\sigma_{buck_{approx}}}}{\partial x}\right|_0 \left(\frac{1}{x^2} - \frac{1}{\mathrm{x}_0^2}\right) \tag{5.26}$$

$$\nabla g_{\sigma_{buck_{approx}}} = \mathrm{x}_0^3 \left.\frac{\partial g_{\sigma_{buck_{approx}}}}{\partial x}\right|_0 \left(\frac{1}{x^3}\right) \tag{5.27}$$

The approximation method is tested on the buckling stress constraint value for element number 6 in the strain-based truss structure, as shown in Figure 5-3. The diameter value for element 6 was perturbed from -50% to +50% of its value, and the buckling stress constraint value was calculated at each point.

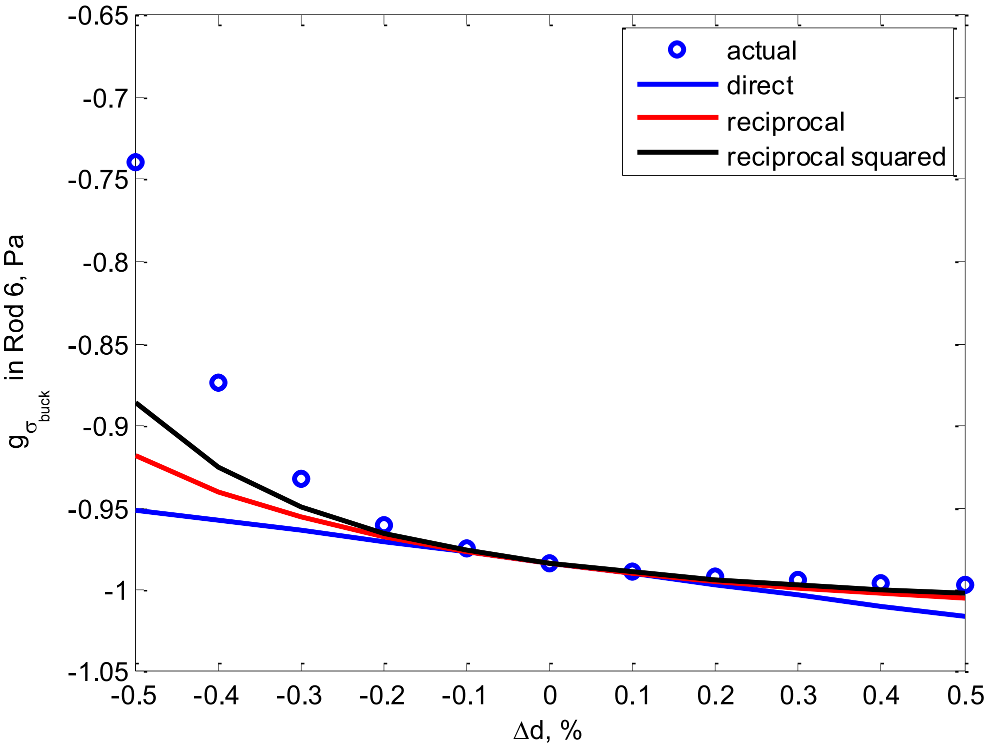

Figure 5-3: Buckling Stress Constraint Approximations

It is observed that the fit is quite good up to 20% away from the nominal diameter but begins to break down when approaching -30% of the nominal value.

The approximation methods were then tested on stress for element 24, an SMA actuator element. The temperature change value was perturbed from -50% to +50% of its value, and the stress value was calculated at each point. Results are shown in Figure 5-4. It is noticed that none of the approximations accurately represent that actual behavior of the SMA material, which looks sinusoidal in nature. The linear approximation may be appropriate for perturbations of 10% from the nominal value or less, but all approximations stray from the exact results after a 10% perturbation.

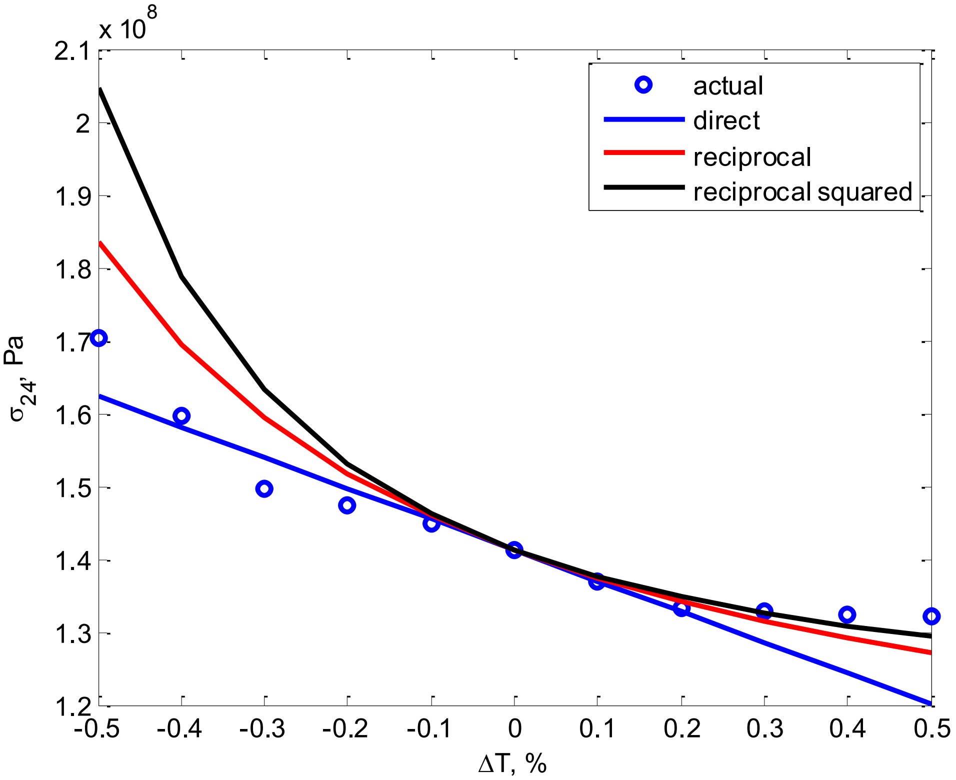

Figure 5-4: SMA Stress Approximations

The approximation methods were lastly tested on y displacement for the bottom node of element 24, node number 7. The temperature change value was perturbed from -50% to +50% of its value, and the displacement was calculated at each point. Results are shown in Figure 5-5. It is noticed that none of the approximations accurately represent that actual behavior of the SMA material, which looks sinusoidal in nature. All of the approximations were fairly accurate for perturbations of 10% the nominal value or less, but all approximations stray from the exact results after a 10% perturbation.

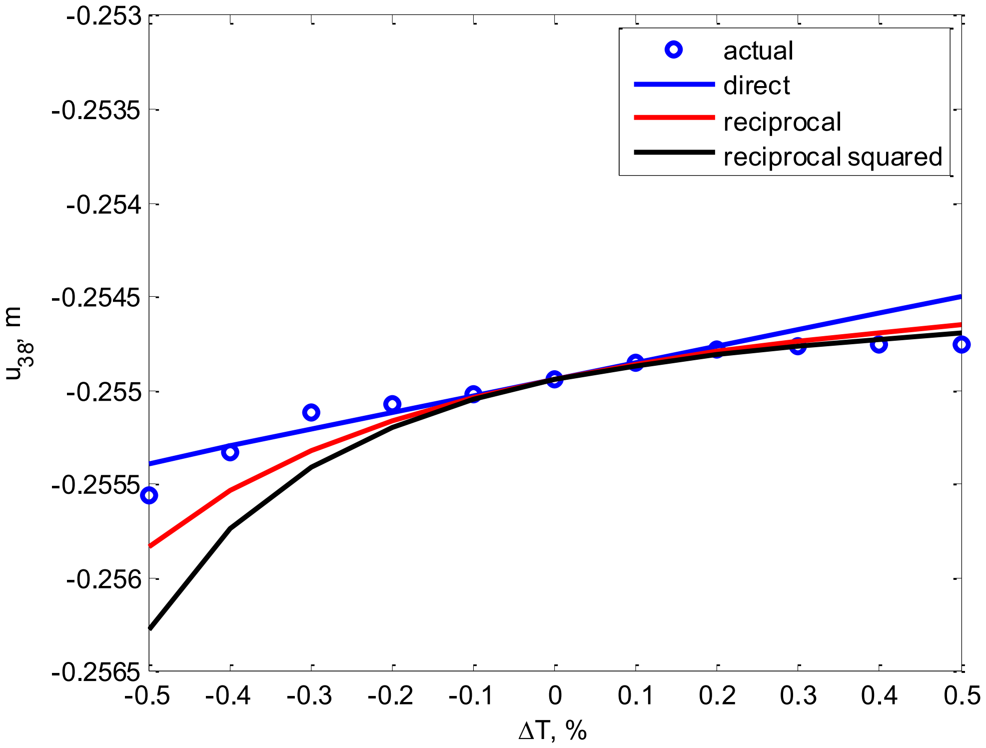

Figure 5-5: SMA Displacement Approximations

As mentioned previously, two approaches could be use for calculating sensitivities: finite difference and analytically. In this exploratory example, the sensitivities of the objective function, structural mass, with respect to all design variables were calculated through forward finite differencing as well as the sensitivity of structure shape constraint with respect to the design variables. The other sensitivities related to the remaining constraints, force, displacement, and stress were calculated analytically according to the equations found in Section 3.1.2.

6 Numerical Results

Multiple approximation techniques and move limit adjustments were used to examine the strain-based truss optimization problem, and the overall results are presented in Table 6. In this table, mass is in kilograms, diameter is in meters, and temperature is in ℃. The results tabulated are the design variable values for each optimization method and, where applicable, for each move limit applied. Due to the units of diameter, the results are shown to three significant figures.

It is determined from this table that all optimization techniques approached mass and design variable values that are fairly close to one another. This may indicate that the reciprocal squared and linear approximations are fairly comparable optimization approximation methods for this specific case.

The optimizations were run on a Dell Studio 1558 laptop with an Intel® Core ™ i3-330M processor. The computer has 3.80GB of RAM that is usable, and it runs the 64-bit Windows 7 Operating System.

Table 6: DV and Objective Results

	Linear			Reciprocal Squared			Combination		
	5%	10%	15%	5%	10%	15%	5%	10%	15%
Mass	42.84	42.25	42.25	42.14	42.30	41.78	42.17	42.32	41.76
d_1	0.0693	0.0693	0.0693	0.0693	0.0693	0.0693	0.0693	0.0693	0.0693
d_2	0.0577	0.0577	0.0577	0.0577	0.0577	0.0577	0.0577	0.0577	0.0577
d_3	0.0462	0.0462	0.0462	0.0462	0.0462	0.0462	0.0462	0.0462	0.0462
d_4	0.0346	0.0346	0.0346	0.0346	0.0346	0.0346	0.0346	0.0346	0.0346
d_5	0.0310	0.0231	0.0231	0.0234	0.0239	0.0231	0.0234	0.0241	0.0231
d_6	0.0309	0.0224	0.0180	0.0234	0.0239	0.0143	0.0239	0.0239	0.0143
d_7	0.0309	0.0224	0.0180	0.0234	0.0239	0.0163	0.0239	0.0239	0.0160
d_8	0.0311	0.0283	0.0283	0.0283	0.0283	0.0283	0.0283	0.0283	0.0283
d_9	0.0400	0.0400	0.0400	0.0400	0.0400	0.0400	0.0400	0.0400	0.0400
d_{10}	0.0516	0.0516	0.0516	0.0516	0.0516	0.0516	0.0516	0.0516	0.0516
d_{11}	0.0632	0.0632	0.0632	0.0632	0.0632	0.0632	0.0632	0.0632	0.0622
d_{12}	0.0748	0.0748	0.0748	0.0748	0.0748	0.0748	0.0748	0.0748	0.0748
d_{13}	0.0675	0.0654	0.0659	0.0666	0.0694	0.0700	0.0666	0.0694	0.0700
d_{14}	0.0677	0.0679	0.0659	0.0679	0.0699	0.0642	0.0681	0.0699	0.0642
d_{15}	0.0631	0.0633	0.0648	0.0651	0.0656	0.0629	0.0651	0.0656	0.0629
d_{16}	0.0647	0.0654	0.0670	0.0632	0.0645	0.0624	0.0632	0.0645	0.0624
d_{17}	0.0577	0.0568	0.0608	0.0597	0.0574	0.0558	0.0597	0.0574	0.0558
d_{18}	0.0574	0.0596	0.0606	0.0570	0.0570	0.0611	0.0570	0.0570	0.0611
d_{19}	0.0528	0.0553	0.0495	0.0522	0.0511	0.0537	0.0522	0.0511	0.0537
d_{20}	0.0509	0.0506	0.0488	0.0506	0.0495	0.0538	0.0506	0.0495	0.0538
d_{21}	0.0439	0.0426	0.0466	0.0454	0.0425	0.0413	0.0454	0.0425	0.0413
d_{22}	0.0421	0.0419	0.0395	0.0433	0.0422	0.0445	0.0433	0.0422	0.0445
d_{23}	0.0318	0.0347	0.0360	0.0324	0.0300	0.0318	0.0324	0.0300	0.0318
d_{24}	0.0314	0.0285	0.0270	0.0265	0.0298	0.0251	0.0265	0.0298	0.0251
T_1	1.7320	0.4753	0.5927	0.1446	0.1446	0.1442	0.1446	0.1446	0.1442
T_2	8.2680	10.016	10.267	10.272	10.272	12.52	10.2430	10.240	11.32
T_3	1.7320	0.3727	0.5212	0.1147	0.2612	0.1151	0.1147	0.2612	0.1151
T_4	8.2680	10.016	10.267	10.272	10.521	12.520	10.2430	10.240	11.32
T_5	1.7320	0.3727	0.4629	0.1051	0.2450	0.1151	0.1051	0.2450	0.1151
T_6	8.2680	10.016	10.267	10.272	10.521	12.520	10.2430	10.240	11.32
T_7	1.7320	0.3249	0.4525	0.0989	0.2056	0.1199	0.0989	0.2056	0.1199
T_8	8.2680	10.016	10.266	10.272	10.521	12.521	10.2430	10.240	11.32
T_9	1.7320	0.3247	0.4017	0.0852	0.1918	0.1928	0.0852	0.1918	0.1928
T_{10}	8.2680	10.016	10.266	10.272	10.521	12.520	10.2430	10.240	11.32
T_{11}	1.7320	0.2918	0.3598	0.0841	0.1895	0.0872	0.0841	0.1895	0.0872
T_{12}	6.2680	10.016	10.279	6.2720	10.521	12.520	6.3220	10.240	11.32

6.1 Linear Approximation Results

The first optimization attempt began with using the direct method for the objective and constraint functions. The move limits began at 5% and were increased to 10% and 15%, then the progressions of the objective function, constraint functions, and design variables were produced.

6.1.1 Results with 5% Move Limits

The optimization with 5% move limits converged after 18 iterations, taking about 2 minutes to complete; therefore, an approximate optimization problem was created and optimized 18 times. The progression of the objective function is shown in Figure 6-1.

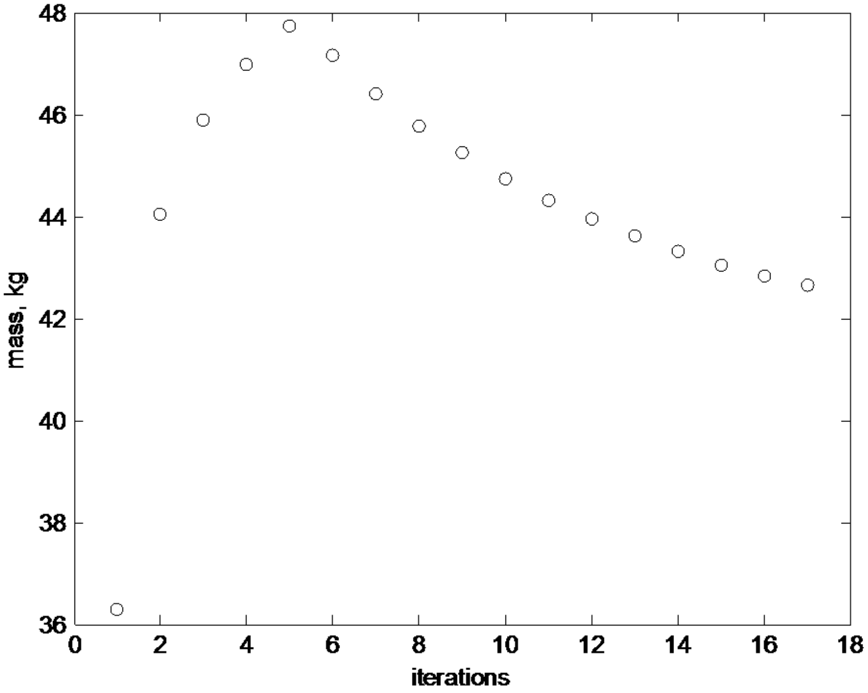

Figure 6-1: Objective Function, Direct, 5% Move Limits

The stress and buckling stress constraints for both the aluminum and SMA elements converged to their end values smoothly and within 5 iterations. Examples of these kinds of constraints are shown in Figure 6-2 and Figure 6-3. Four of the aluminum stress constraints proceeded to drive the optimization by being tight, but the SMA constraints were sufficiently satisfied.

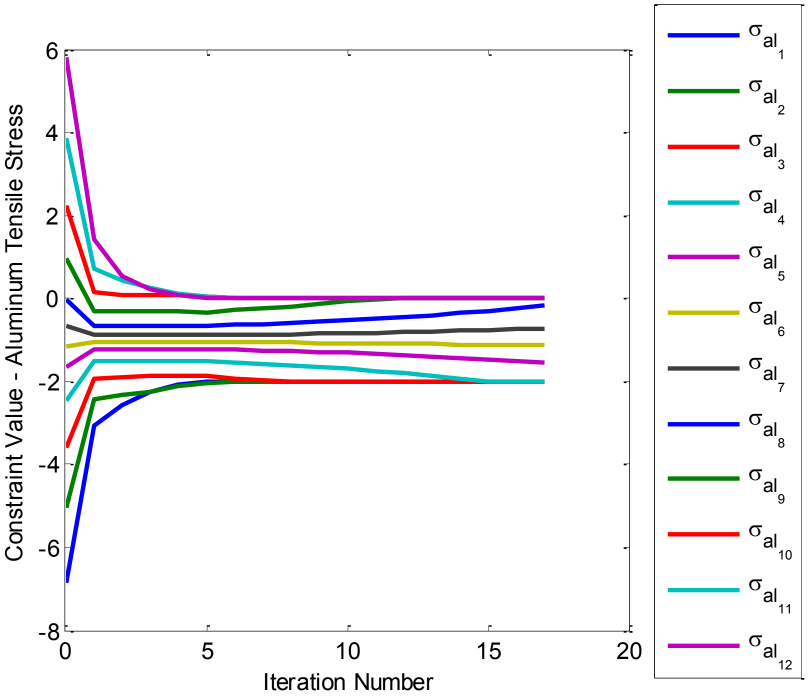

Figure 6-2: Representative Aluminum Stress Constraint, Direct, 5% Move Limits

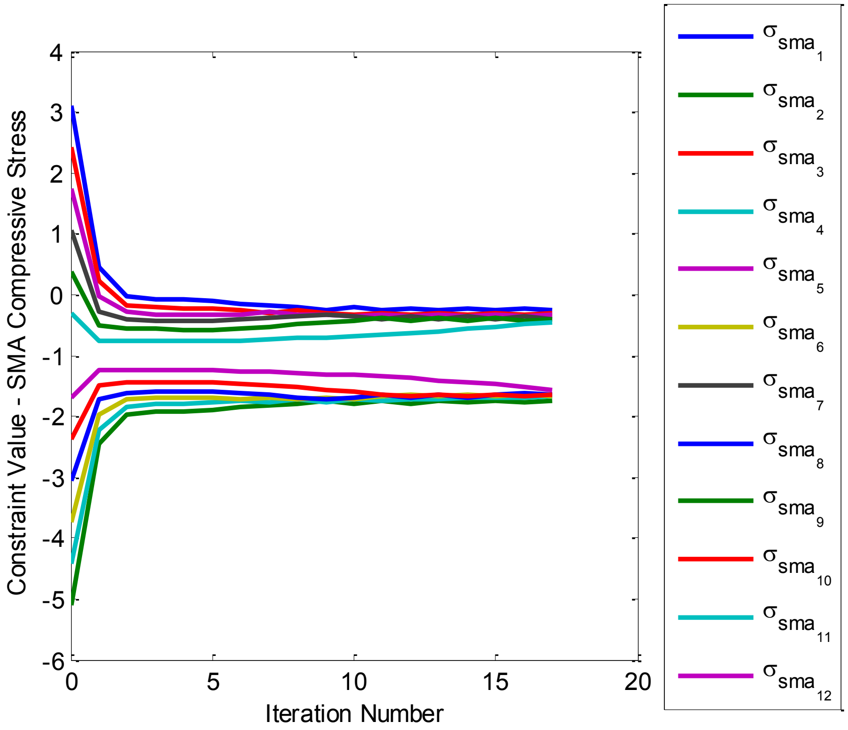

Figure 6-3: Representative SMA Stress Constraint, Direct, 5% Move Limits

The shape error constraint is shown in Figure 6-4 to be smoothly reaching its final value. The shape error constraint is one of the tight constraints that drive this optimization.

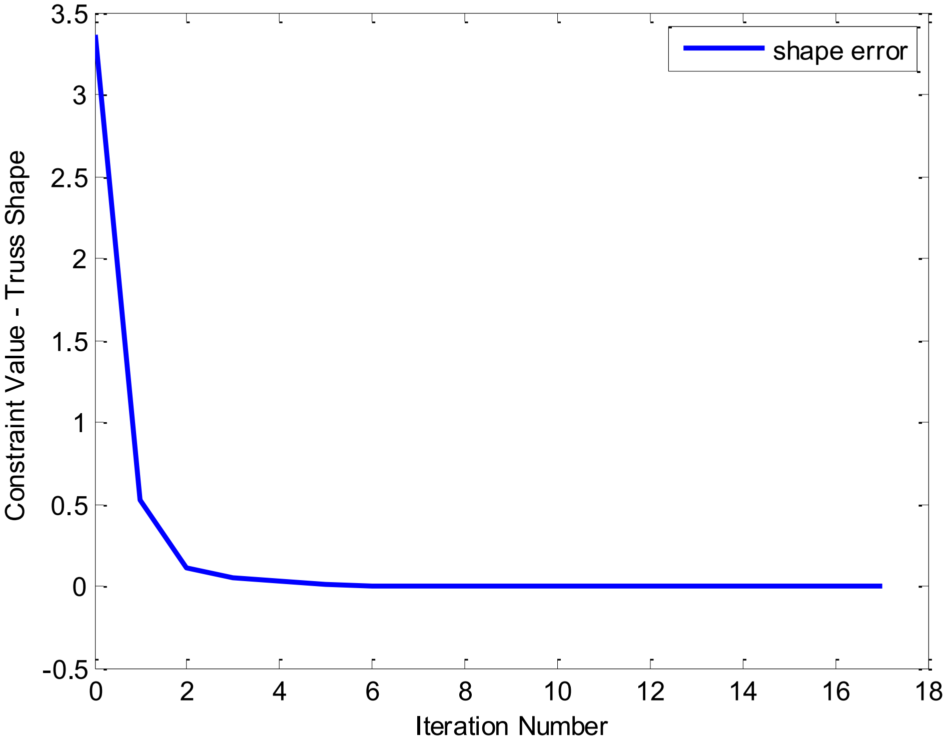

Figure 6-4: Shape Constraint, Direct, 5% Move Limits

For the direct method, both the SMA element diameter and applied temperature change experienced oscillations in their progressions, as shown in Figure 6-5 and Figure 6-6. It is noticed that most of the temperatures approached three values: approximately 8, 6, and 1.5 degrees Celsius.

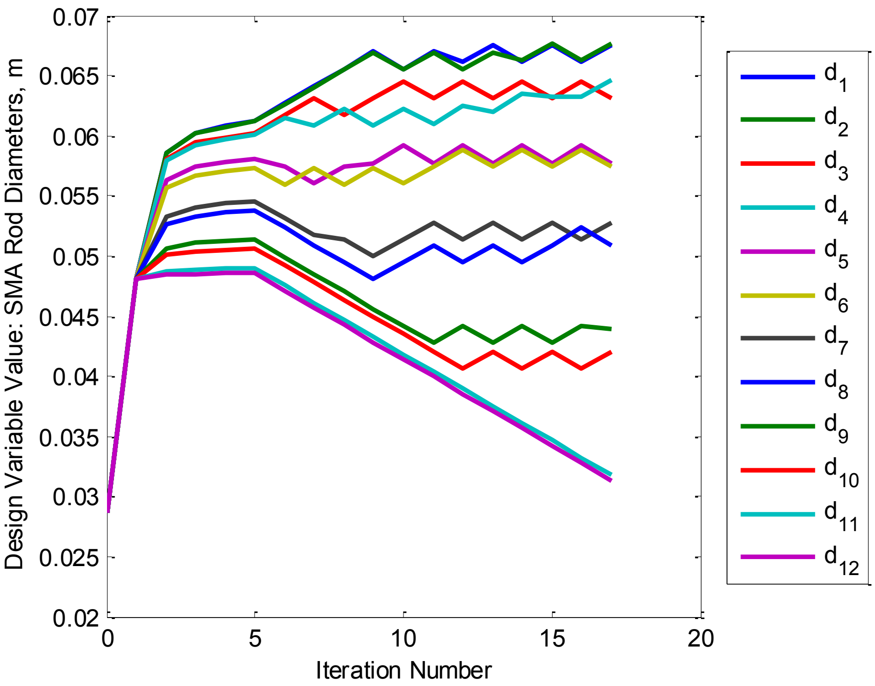

Figure 6-5: SMA Diameters, Direct, 5% Move Limits

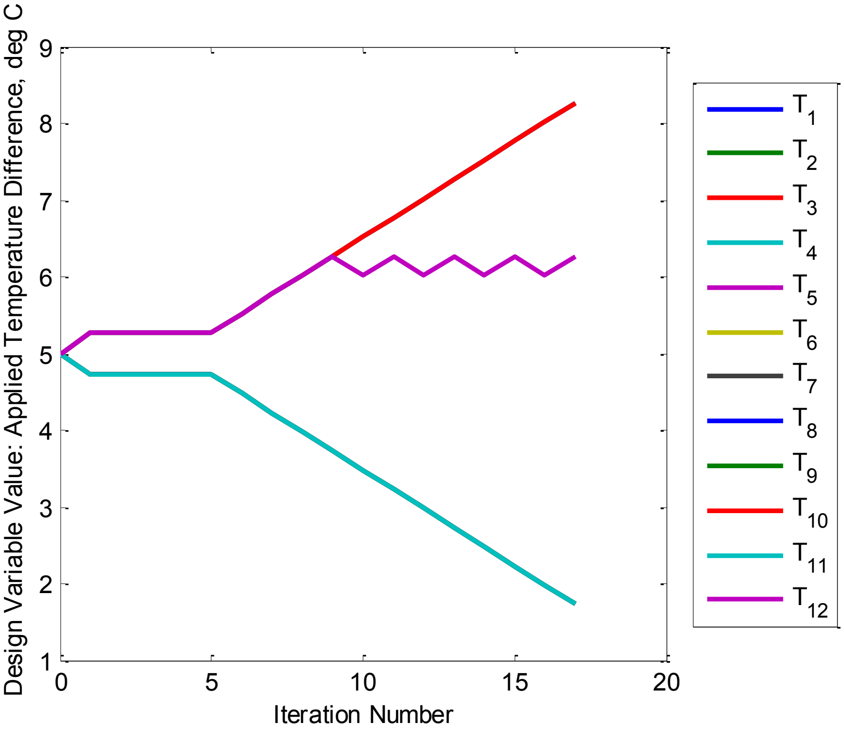

Figure 6-6: Temperatures, Direct, 5% Move Limits

6.1.2 Results with 10% Move Limits

The move limits were then increased to 10% for the direct approximation. This approach allowed the optimization to converge in 13 iterations, resulting in 4 fewer calls to the nonlinear simulation code. The mass progression is shown in Figure 6-7.

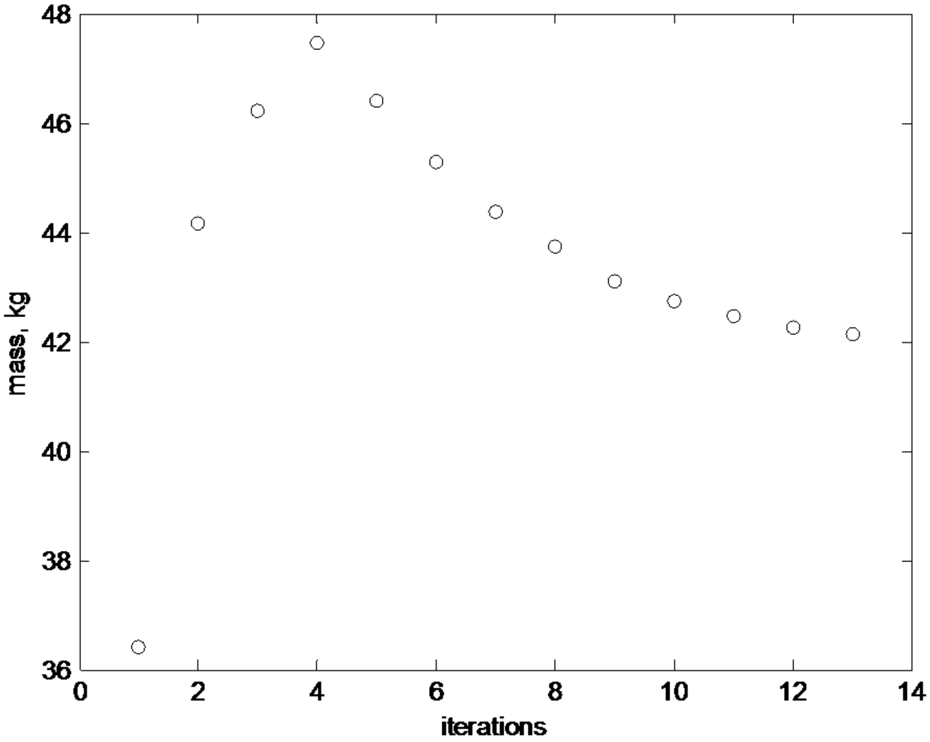

Figure 6-7: Objective Function, Direct, 10% Move Limits

With the increased move limits, oscillations in the SMA stress constraints appeared, and the ones in the SMA diameter results increased in magnitude. These results are shown in Figure 6-8 and Figure 6-9.

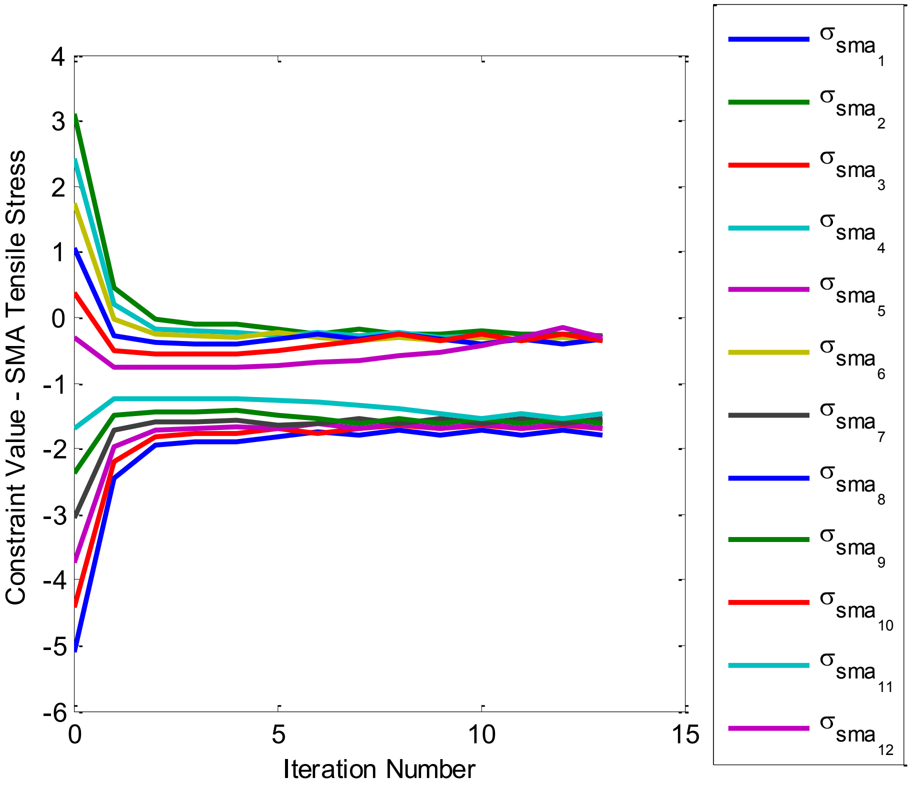

Figure 6-8: Representative SMA Stress Constraint, Direct, 10% Move Limits

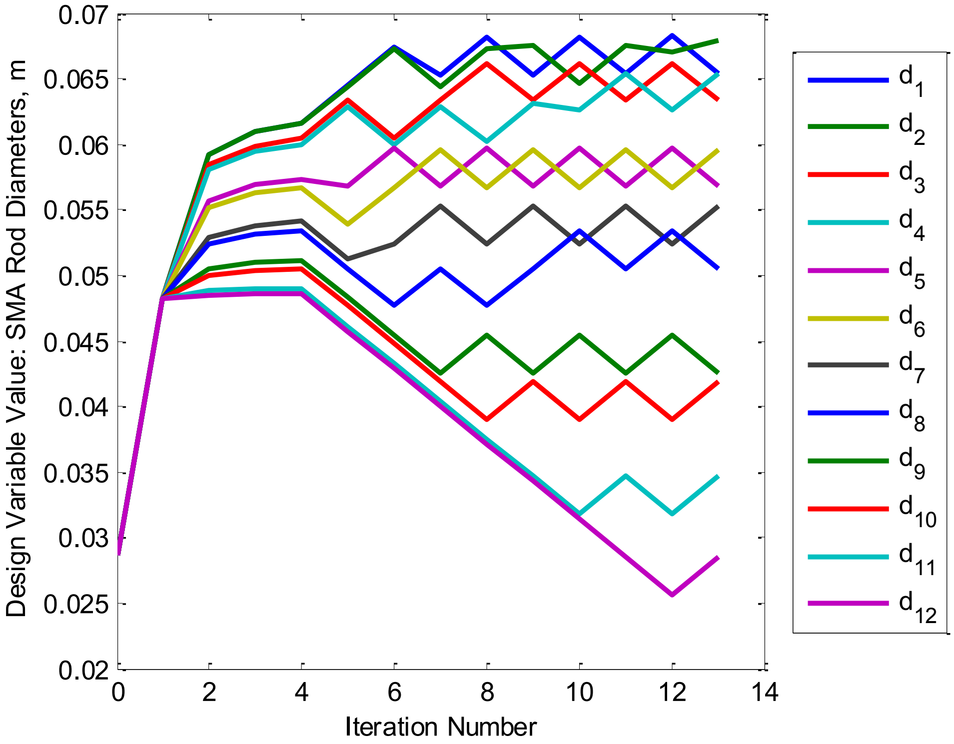

Figure 6-9: SMA Diameters, Direct, 10% Move Limits

6.1.3 Results with 15% Move Limits

Lastly, the move limits were increased to 15% for the direct method. This approximation method caused the optimization to converge in only 10 iterations, or about a minute of computation time. The objective function is plotted in Figure 6-10.

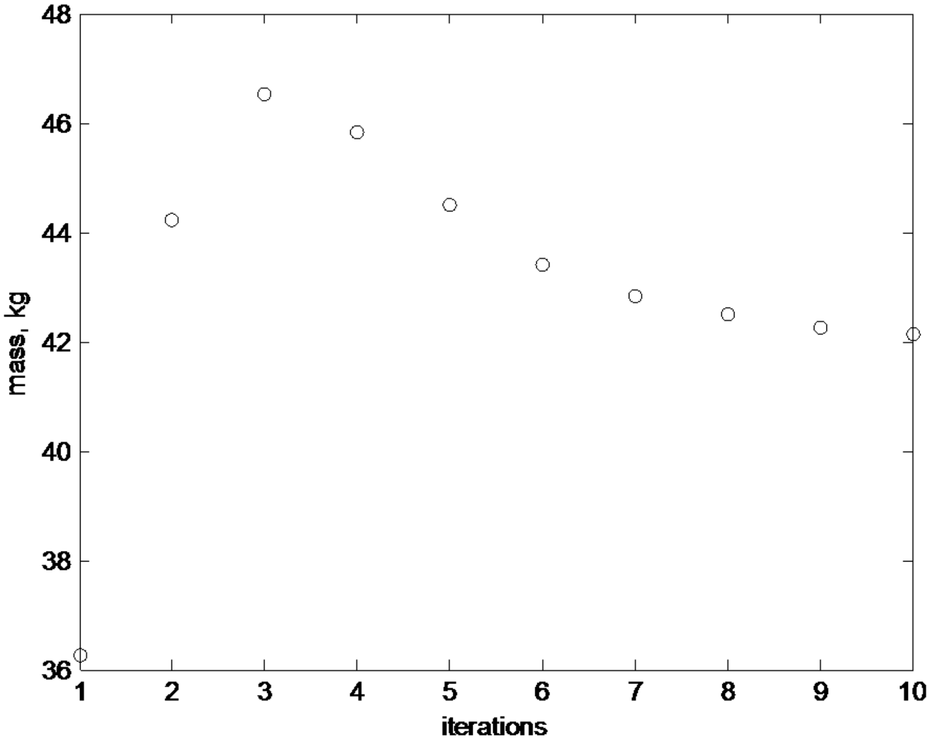

Figure 6-10: Objective Function, Direct, 15% Move Limits

The oscillations in the SMA stress constraints have increased slightly, and the oscillations in the diameter calculation have magnitudes of approximately 0.004m, or 0.17 inches. When compared to the overall scale of the model – 0.2m per element in length – these oscillations are equal to approximately one fourth of the element's size. These results are displayed in Figure 6-11 and Figure 6-12.

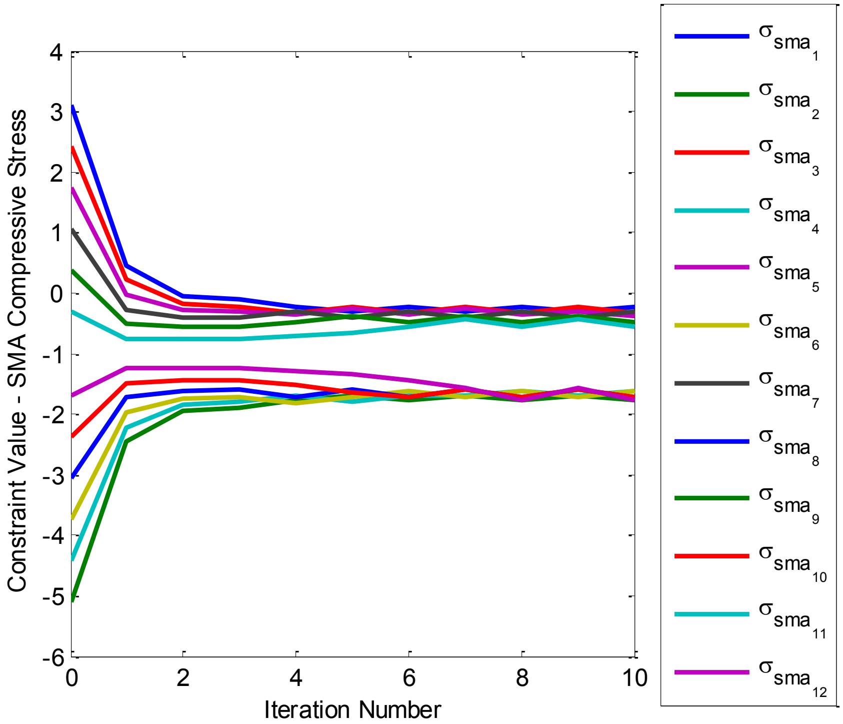

Figure 6-11: Representative SMA Stress Constraint, Direct, 15% Move Limits

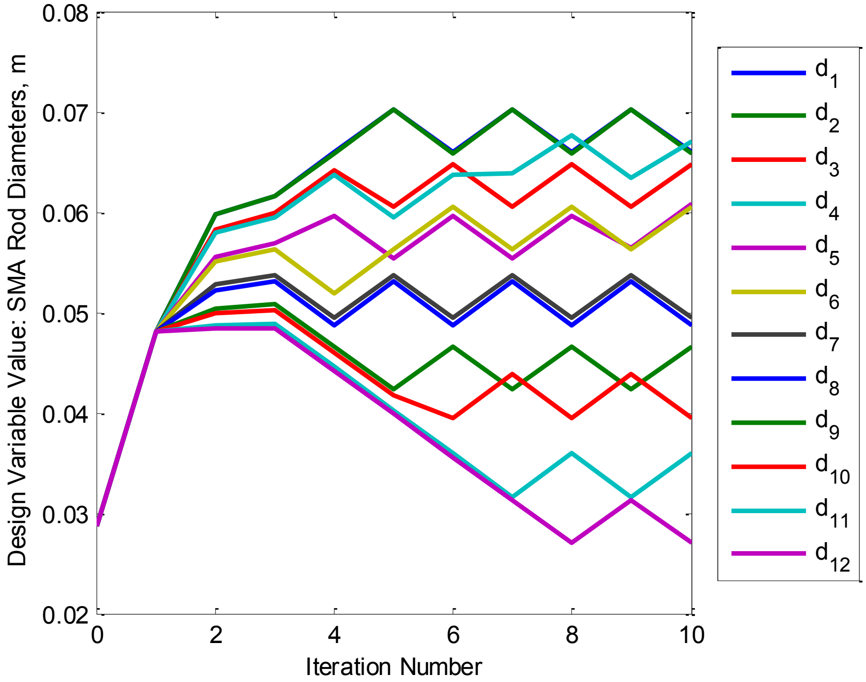

Figure 6-12: SMA Diameters, Direct, 15% Move Limits

The direct approximation, for small move limit values, produced realistic design variable values in a short amount of time; therefore, when used appropriately, this approximation can give desirable results when computation time is an issue.

6.2 Reciprocal Squared Results

Since it is hypothesized that the reciprocal squared approximation will better serve the stress constraints, this method was used for all design variables. The integrity of this approximation method is tested by increasing move limits from 5% to 10% and 15%.

6.2.1 Results with 5% Move Limits

The objective function progression of the reciprocal squared approximation with 5% move limits applied to both diameter and temperature design variables is shown in Figure 6-13. The optimization took 25 iterations to converge to an answer, approximately 3 minutes of computation time.

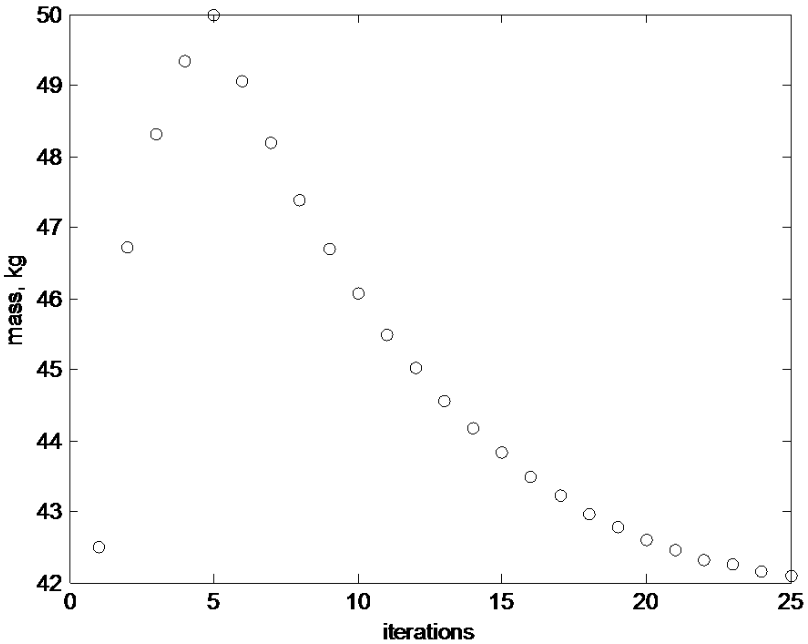

Figure 6-13: Objective Function, Reciprocal Squared, 5% Move Limits

The stress and buckling stress constraint values for the aluminum elements smoothly converged, with a representation of this behavior shown in Figure 6-14. As seen in this figure, five of the constraints became tight. Also, seeing the constraint values of -2 indicate the some compressive stress constraints are also tight. It was also noticed that all forms of stress constraints converged within about 5 iterations.

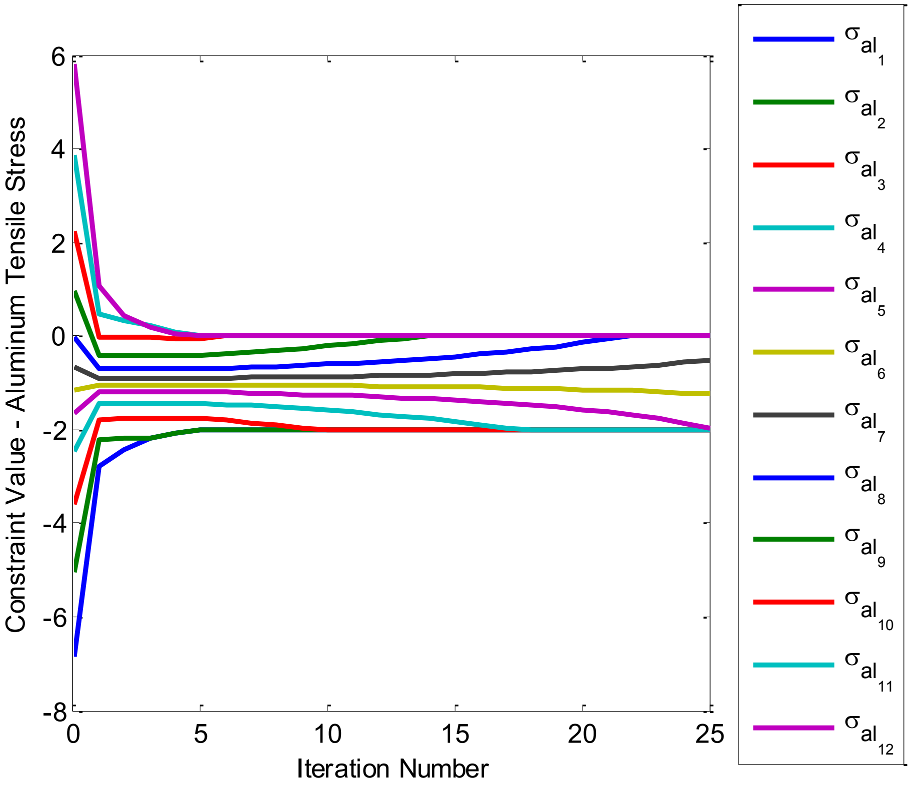

Figure 6-14: Representative Aluminum Stress Constraint, Reciprocal Squared, 5% Move Limits

The stress constraint values had a slight numerical oscillation as shown in Figure 6-15. These constraints also took much longer to converge than its aluminum element counterparts.

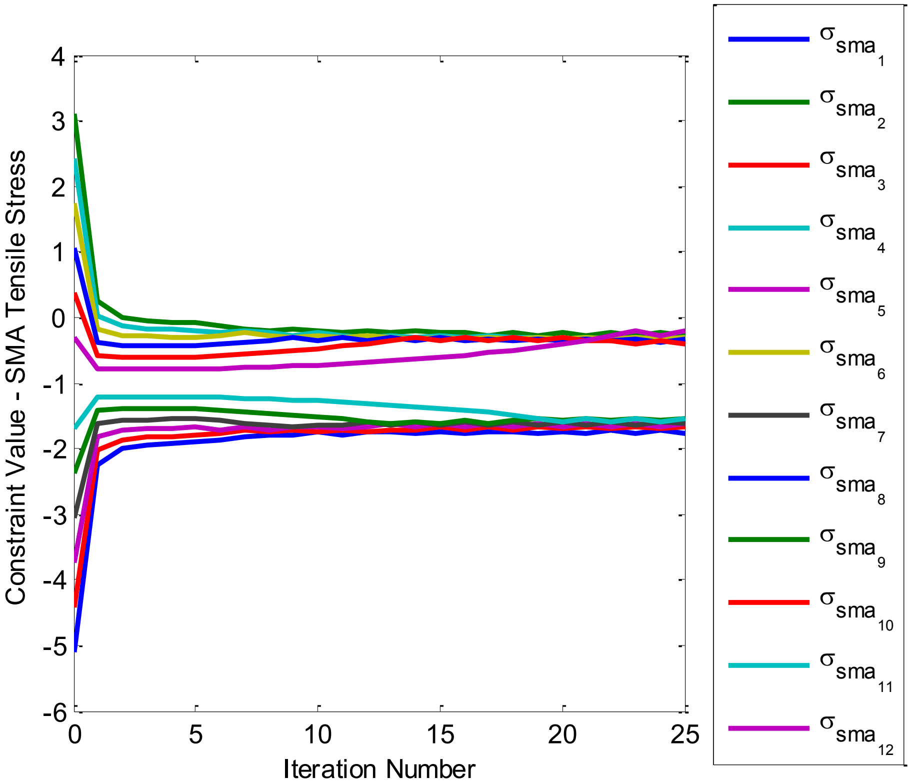

Figure 6-15: Representative SMA Stress Constraint, Reciprocal Squared, 5% Move Limits

The shape constraint value progression is shown in Figure 6-16. The result is a smooth progression that converged at approximately 5 iterations.

The diameter design variables related to the aluminum elements also smoothly converged to their final values shown in Table 6, as did the temperature results; on the other hand, the SMA diameter design variables had oscillations as in the stress constraints, as shown in Figure 6-17. The magnitude of these oscillations were 0.0014 meters, or approximately 0.6 inches.

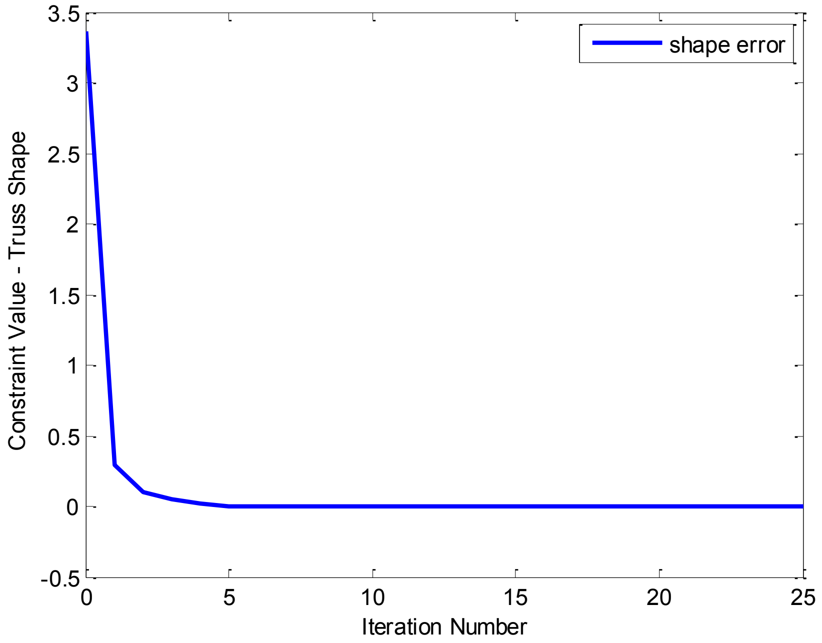

Figure 6-16: Shape Constraint, Reciprocal Squared, 5% Move Limits

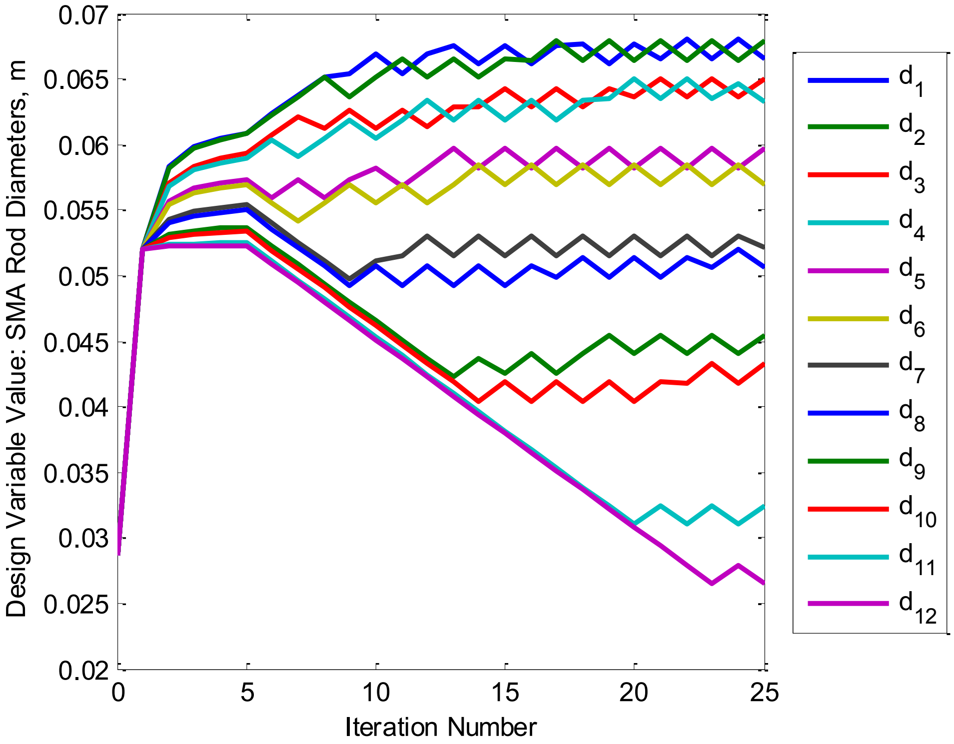

Figure 6-17: SMA Diameters, Reciprocal Squared, 5% Move Limits

6.2.2 Results with 10% Move Limits

The move limits were then increased to 10%, and results are shown in the following figures, beginning with the objective function progression in Figure 6-18. Increasing the move limits reduced the computation time and number of iterations, with the system converging in 14 iterations.

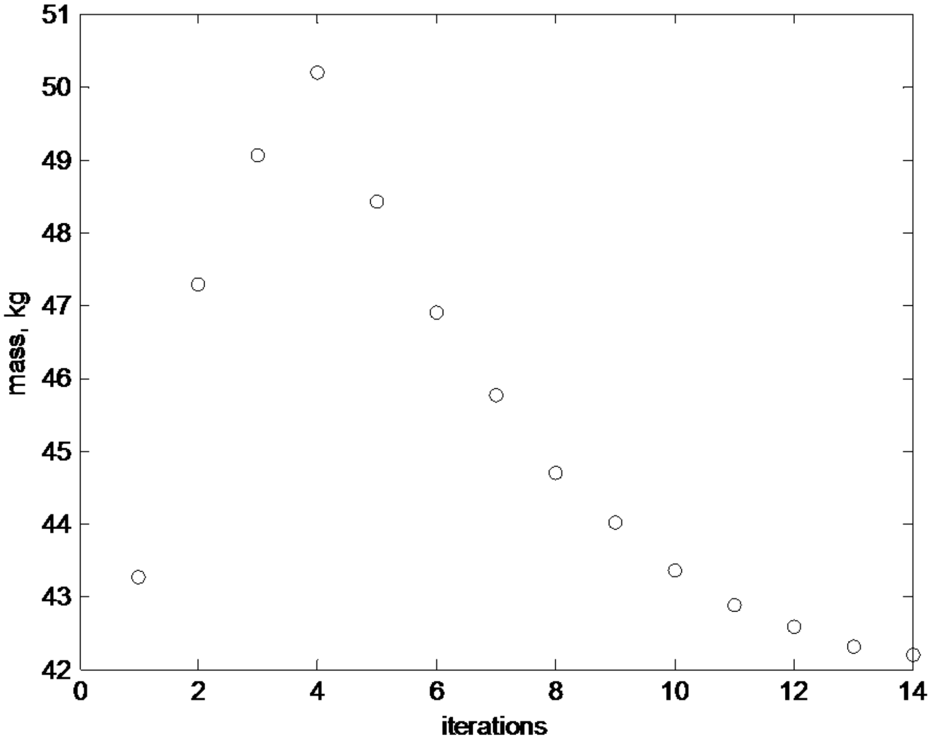

Figure 6-18: Objective Function, Reciprocal Squared, 10% Move Limits

The stress and buckling stress constraints as well as the shape error constraint behave similarly to those with 5% move limits, but the SMA rod design variables produced larger oscillation magnitudes, as shown in Figure 6-19.

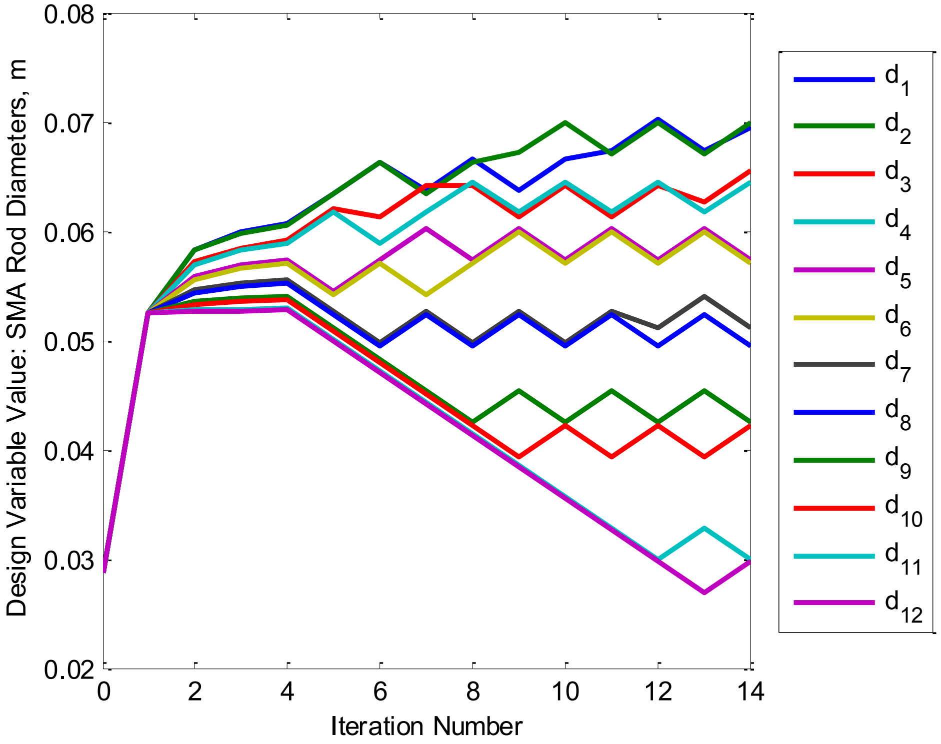

Figure 6-19: SMA Diameters, Reciprocal Squared, 10% Move Limits

6.2.3 Results with 15% Move Limits

The move limits were increased one more time to 15%. Increasing the move limits by 5% only saved two iterations worth of convergence time, as shown in the objective function history in Figure 6-20.

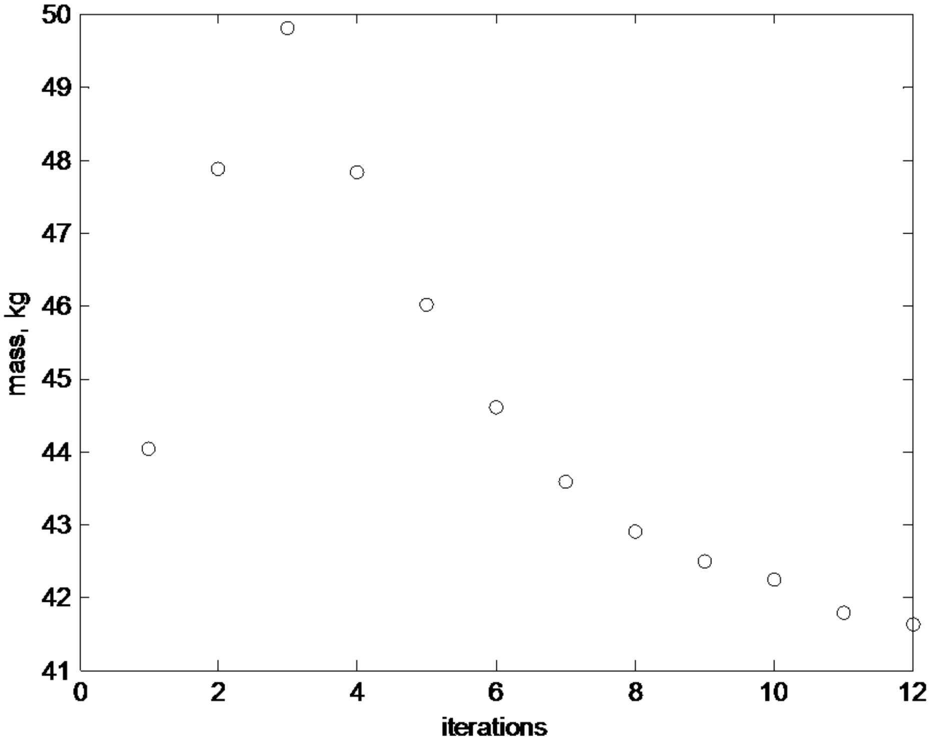

Figure 6-20: Objective Function, Reciprocal Squared, 15% Move Limits

The oscillation magnitudes related to the SMA elements again increased as the move limit increased. A representative stress constraint and the SMA diameters are plotted in Figure 6-21 and Figure 6-22. At this point, the oscillations in the SMA diameter design variables are unacceptably large.

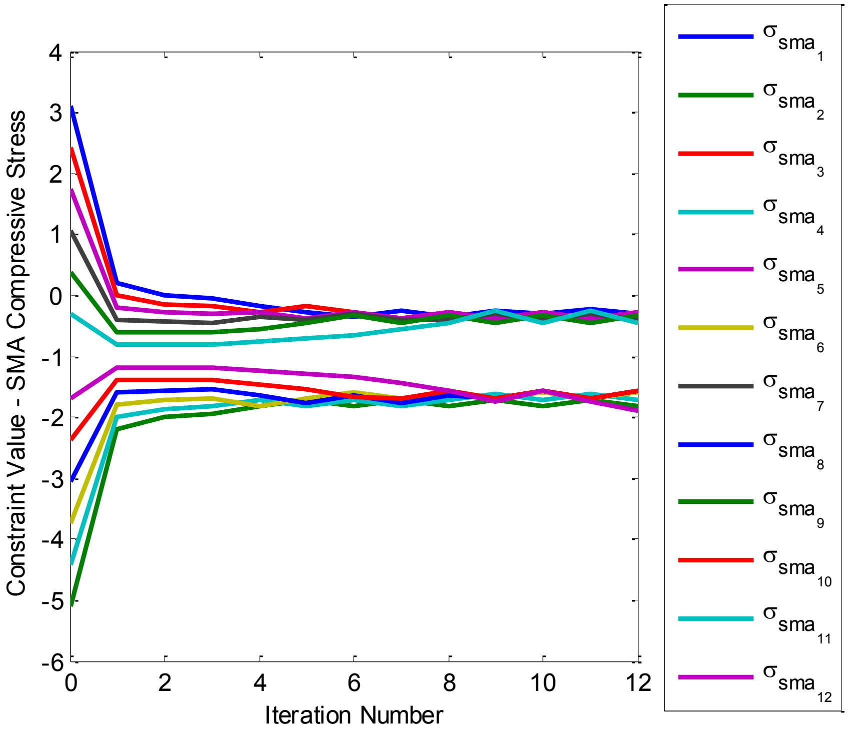

Figure 6-21: Representative SMA Stress Constraint, Reciprocal Squared, 15% Move Limits

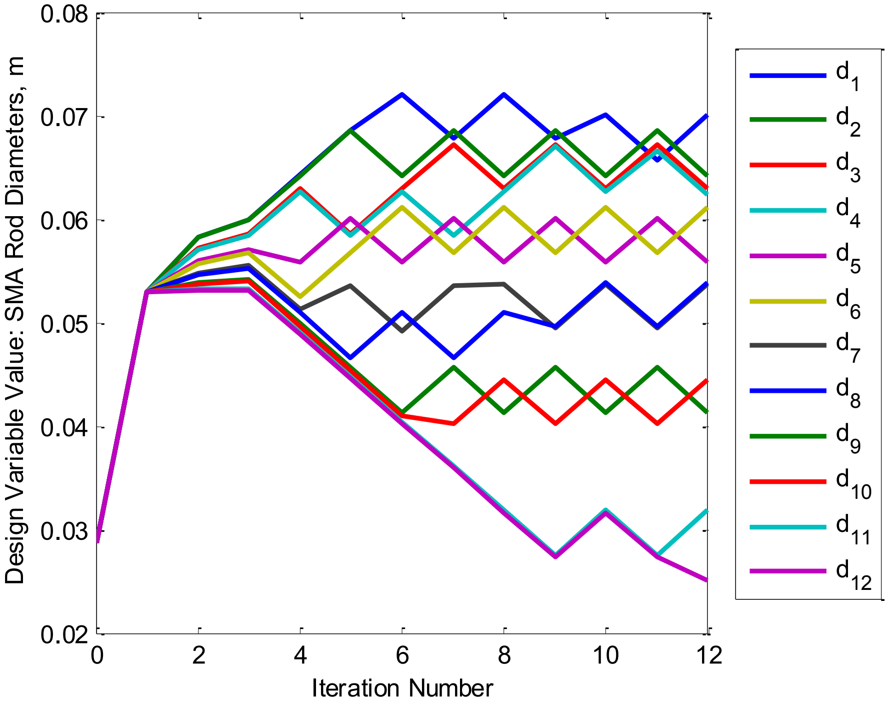

Figure 6-22: SMA Diameters, Reciprocal Squared, 15% Move Limits

Overall, the reciprocal squared approximation behaved similarly to the linear approximations for all design variables in terms of final values and oscillation behavior. The move limit values must still remain quite small, due to the nonlinearity of the SMA behavior, to prevent the oscillations from becoming too large. For this magnitude of a problem, using small move limits is not a large issue, as the smallest move limit case produced results in approximately 3 minutes; for a large problem with thousands of degrees of freedom, however, an even better approximation should be found to allow for larger move limits and to decrease convergence time.

6.3 Reciprocal Squared/Linear Combination Results

A combination of the reciprocal squared method for the diameter design variables and the direct method for temperatures was employed to examine whether or not the direct approximation was better than the linear approximation for temperatures. Again, the move limits were increased from 5% to 10% and 15%.

6.3.1 Results with 5% Move Limits

The approximation technique with 5% move limits again, obviously, took the longest to run, completing in approximately 3 minutes and ending in 25 iterations. Figure 6-23 displays the mass progression for this technique.

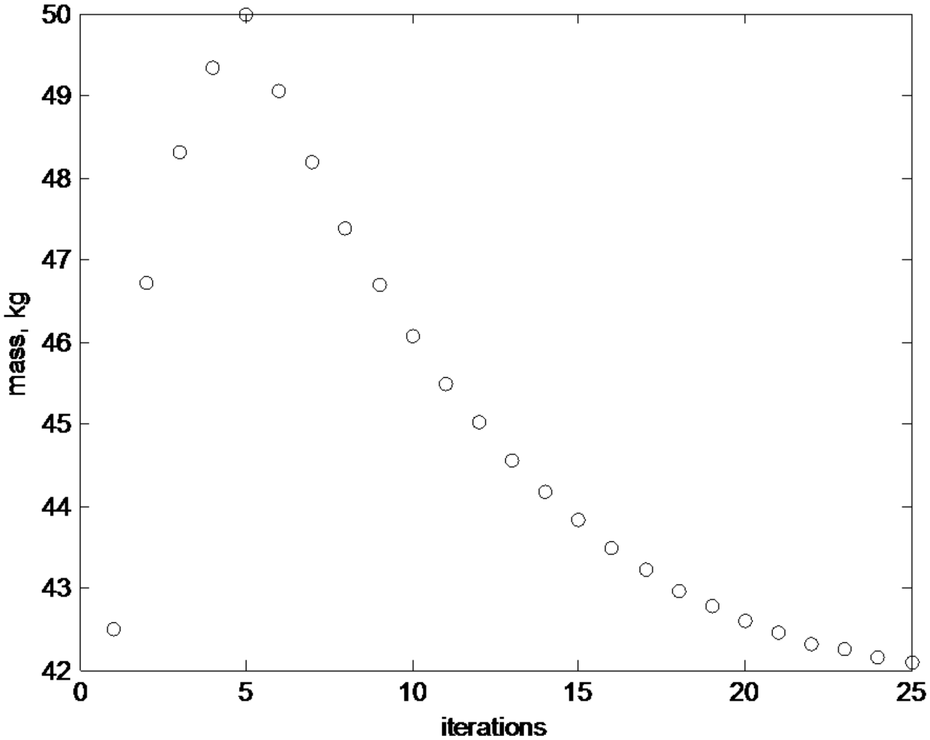

Figure 6-23: Objective Function, Combination, 5% Move Limits

Again, the stress constraints for the SMA elements had slight oscillations in their results, as shown in Figure 6-24.

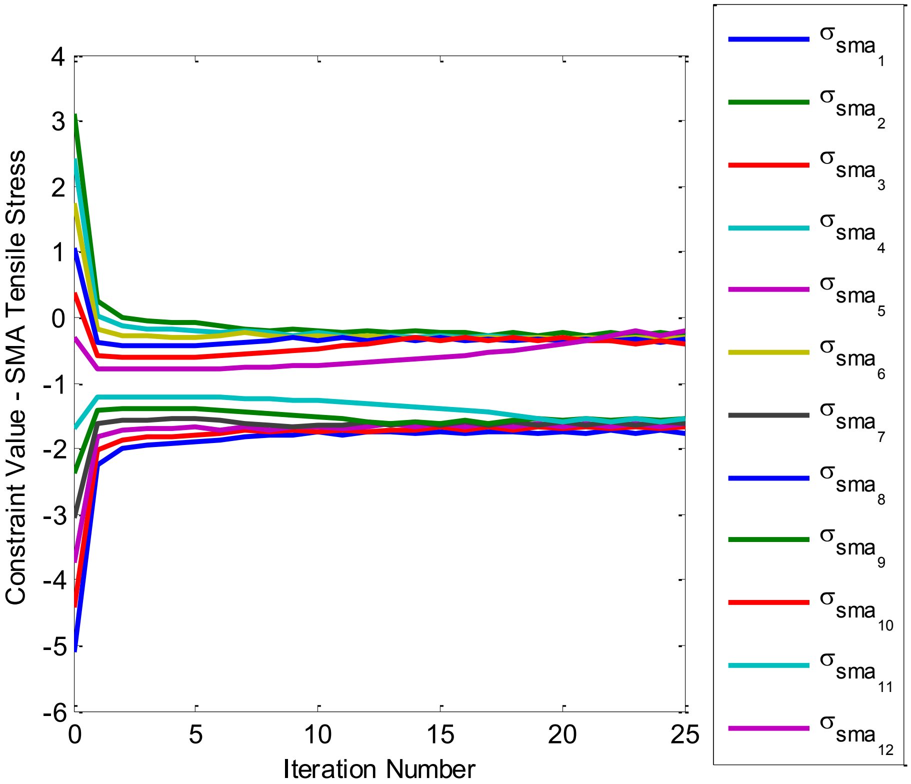

Figure 6-24: Representative SMA Stress Constraint, Combination, 5% Move Limits

The shape constraint value progressed smoothly (seen in Figure 6-25) as well as constraints and design variables related to the aluminum elements; however, there were again oscillations in the SMA diameter design variables, shown in Figure 6-26.

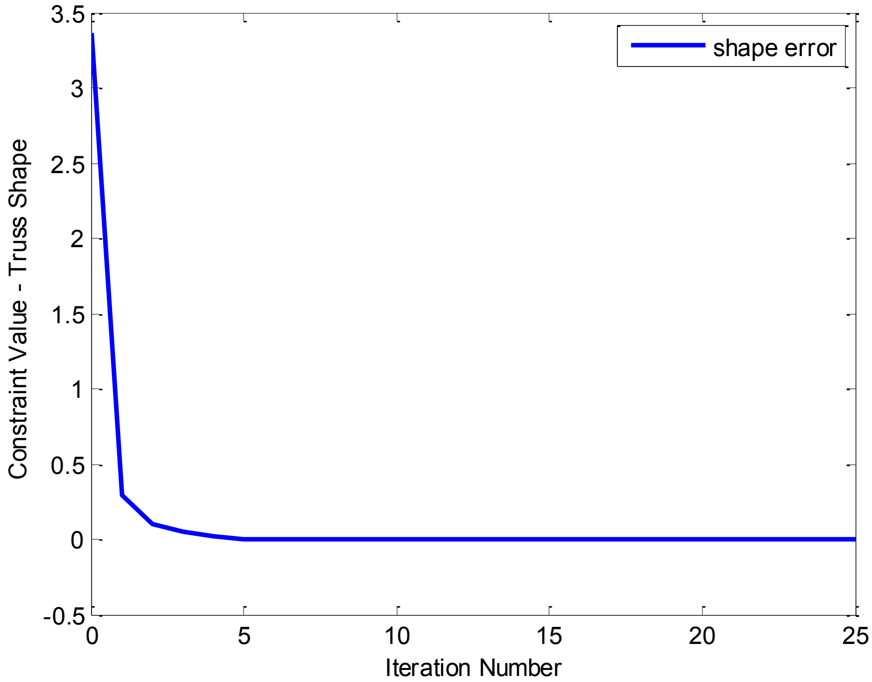

Figure 6-25: Shape Constraint, Combination, 5% Move Limits

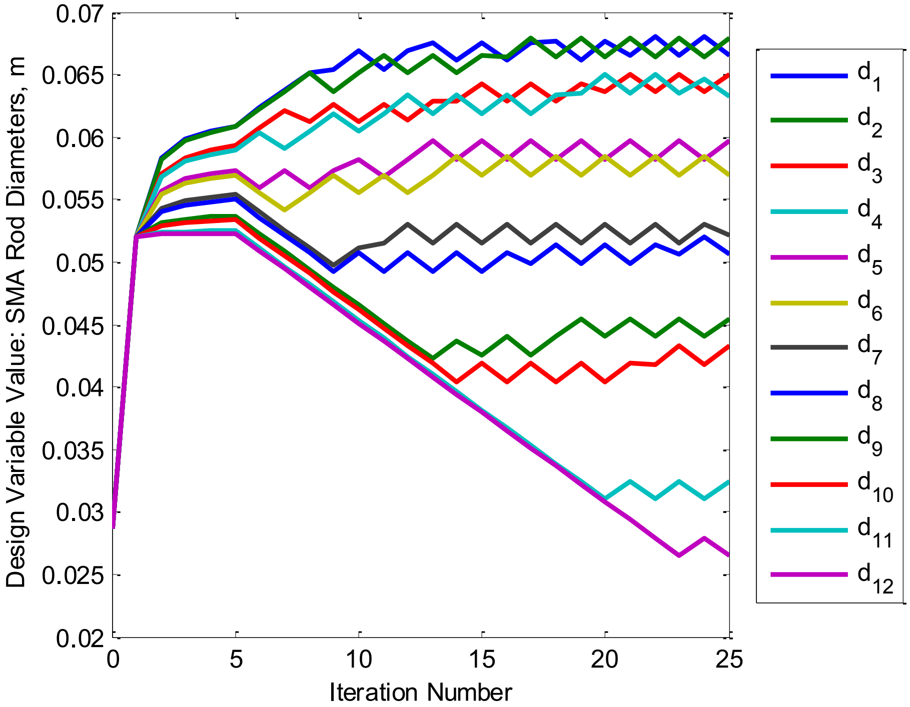

Figure 6-26: SMA Diameters, Combination, 5% Move Limits

6.3.2 Results with 10% Move Limits

The move limits were next increased to 10%. Similar to the reciprocal squared method, the optimization converged in 14 iterations, as shown in Figure 6-27. The oscillations in the SMA design variables were still present and slightly larger than those in the 5% move limit plots.

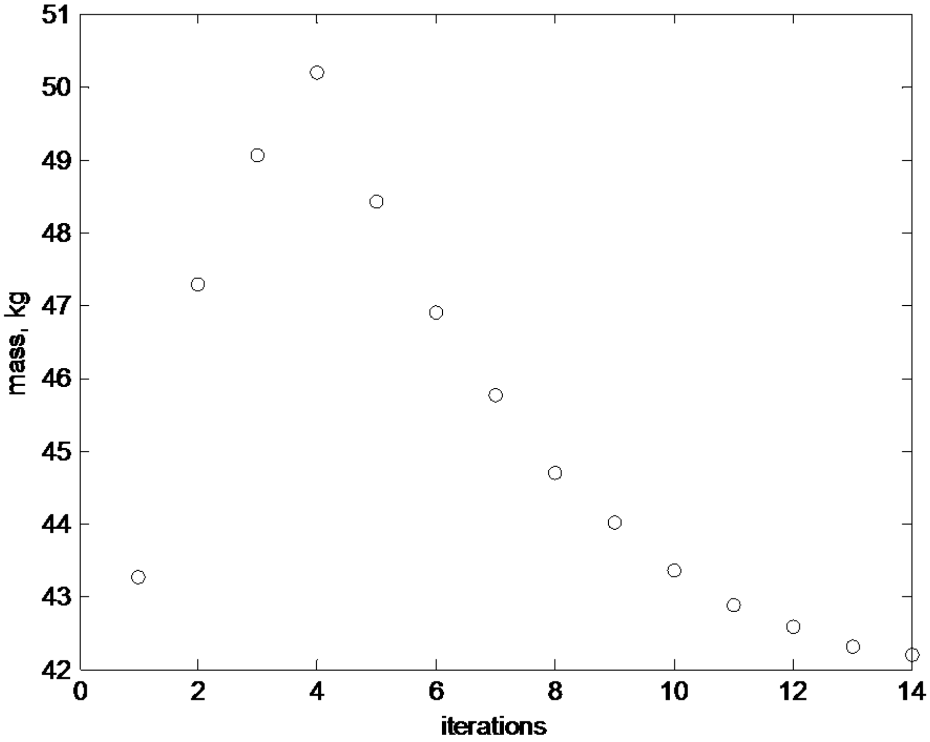

Figure 6-27: Objective Function, Combination, 10% Move Limits

6.3.3 Results with 15% Move Limits

Lastly, a 15% move limit is imposed on the design variables, again resulting in larger oscillations for the SMA elements. The optimization converged the quickest, in 12 iterations, but produced the least accurate results with the largest oscillations, which were again approximately 0.004 meters. These assertions are evident in Figure 6-28 and Figure 6-29.

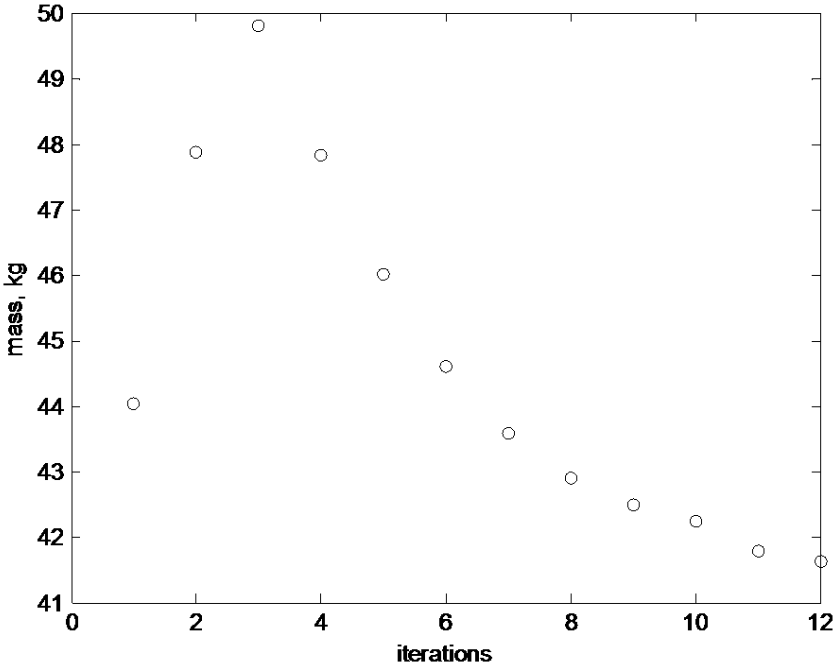

Figure 6-28: Objective Function, Combination, 15% Move Limits

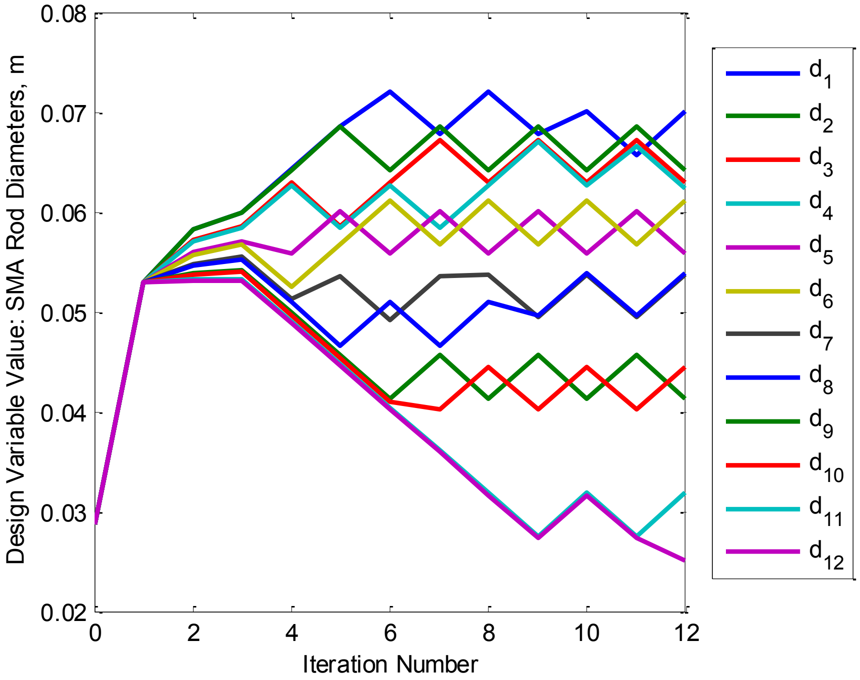

Figure 6-29: SMA Diameters, Combination, 15% Move Limits

The combination method behaved similarly to the reciprocal squared method, with optimizations converging in similar amounts of time and oscillations in the constraints and design variables related to SMA materials.

Ultimately, all of these approximations yielded similar results, with minimum masses all reaching close to 42kg. All approximations were susceptible to oscillations, due to the nonlinearities of the system and to the quality of the approximation fit.

7 Conclusions and Future Work

A capability was developed to perform structural analysis on three-dimensional structures with rod and membrane elements, which was validated in Chapter 2 (membrane validation is shown in Appendix A). This code allows the user to specify:

- Node locations (x, y, z) for the structure
- External forces on the structure
- Material and geometric properties for each element

Structural responses such as stress and displacement were then calculated. The second phase of the code allows for gradient-based optimizations using direct, reciprocal, hybrid, or reciprocal squared model approximations using the NLP/AC optimization method. Finite difference and analytic sensitivities were calculated with respect to design variables such as rod cross sectional area or diameter and applied temperature to the SMA actuator. The optimization was then exercised on a truss structure with conventional structural elements and one with strain-based actuators. These optimization problems sought to minimize mass subject to a combination of stress and buckling stress constraints, and it was also required that the truss be forced back to its original configuration as closely as possible. For the strain-based truss structure, the linear and reciprocal squared approximations produced good results for small move limit values and included increasingly larger oscillations in SMA results as the move limits were increased; therefore, it can be concluded that, although the approximations produced feasible results, the high nonlinearities associated with buckling as well as shape memory alloy behavior made the process difficult. For this small of an optimization problem, either a brute-force approach where the optimizer interacts directly with the nonlinear simulation may be the best way to achieve desirable results, or better approximation methods must be developed.

Because of the complex nonlinear behavior of SMA actuators, Taylor Series-based constraint function approximations have to be used with caution, with proper move limits that would protect the accuracy of the approximation. In the present studies, the NLP/AC process converged to find feasible locally-optimal designs, but some oscillations of SMA related design variables were noticed - a result, probably, of slight differences in value of such functions between consecutive approximate optimization steps. Oscillations of SMA-related inactive constraints were also noticed. With the optimization convergence criteria used in typical practical NLP/AC optimizations, quite often objective and constraint functions would converge to their optimal values while certain design variables would still show variation in magnitudes when the process is stopped.

A great deal of work can be done in the future to improve this technology. The inclusion of membrane elements will allow for the development of more complex structures, such as a wing box, to analyze. Other approximation methods could also be explored to remove the oscillations in the SMA design variable results. For example, the SMA stress-temperature relationship somewhat resembled a sinusoid, so a sinusoidal approximation could potentially relate temperature and stress and provide better results. If a wing is a desired structure to analyze, the code can then be coupled with an unsteady aerodynamics code to perform aeroservoelastic optimizations. The usage of the SMA and piezoelectric materials could also be better employed on a wing or airfoil. For example, it is known that SMA materials can provide large deflections, while piezoelectric materials are usually applied for vibration control; therefore, a problem can be set up where SMA's are employed on the wing to control camber, for example, while piezoelectrics are placed on an aileron element for flutter suppression. An optimization technology could also be developed to determine where on the wing an SMA or a piezoelectric material could be optimally employed. Also, since the code can compute mode shapes and frequencies, frequency-related constrains can also be imposed on the system in the future.

References

[1] Jordan, T.L and Ounaies, Z. Piezoelectric Ceramics Characterization. Langley Research Center, Hampton, Virginia: National Aeronautics and Space Administration (US). September 2001. ICASE Report No: 2001-28.

[2] Chopra, Inderjit. “Review of State of Art of Smart Structures and Integrated Systems”. AIAA Journal, Vol. 40, No.11 (2002), pp. 2145-2187.

[3] Simpson, J.O., Wise, S.A., Bryant, R.G, Cano, R.J., Gates, T.S., Hinkley, J.A., Rogowski, R.S., Whitley, K.S. “Innovative Materials for Aircraft Morphing”. Technical Report, 1998. NASA Langley Technical Report Server.

[4] Huang, Weimin. Shape Memory Alloys and their Application to Actuators for Deployable Structures. Diss. University of Cambridge, 1998.

[5] Song, Chengli. “History and Current Situation of Shape Memory Alloys Devices for Minimally Invasive Surgery.” The Open Medical Devices Journal, Vol. 2, 2010, pp 24-31.

[6] Hartl, Darren and Lagoudas, Dimitris C. “Aerospace Applications of Shape Memory Alloys.” Proceedings of the Institution of Mechanical Engineers, Part G: Journal of Aerospace Engineering, April 1, 2007 vol. 221 no. 4: 535-552

[7] Bieniawski, Stefan R., Bushnell, Glenn S, Calkins, Frederick T, Mabe, James H. Feb 2012. Shape Memory Alloy Actuator. United States Patent 8118264 B2.

[8] Jackson, Timothy W. Design-oriented Aeroservoelastic Optimization of Strain-actuated Aircraft. Diss. University of Washington, 2005.

[9] Cook, R.D., et.al. Concepts and Applications of Finite Element Analysis. John Wiley & Sons, Inc., Fourth Edition, 2002.

[10] Liang, C. and Rogers, C.A., "Design of Shape Memory Alloy Actuators," Journal of Mechanical Design, Vol. 114, June, 1992, pp 223-230.

[11] Liang, C. and Rogers, C.A., "One-Dimensional Thermomechanical Constitutive Relations for Shape Memory Materials." Journal of lntelligent Material Systems and Structures, Vol. 1, April, 1990, pp 207-234.

[12] Haftka, R.T. and Gurdal, Zafer. Elements of Structural Optimization. Springer, Third Revised and Expanded Edition, 2008.

[13] Vanderplaats, Garret N. Multidiscipline Design Optimization. Vanderplaats Research & Development, Incorporated, First Edition, First Printing, 2007.

[14] De Veubeke, B.Matrix Methods of Structural Analysis. Pergamon Press, 1964.

[15] Harvey, Michael. Automated Finite Element Modeling of Wing Structures for Shape Optimization. Thesis. University of Washington, 1993.

[16] Mathworks, Inc. “fmincon”. Documentation Center. <http://www.mathworks.com/help/optim/ug/fmincon.html>

[17] Byrd, R.H., J. C. Gilbert, and J. Nocedal, "A Trust Region Method Based on Interior Point Techniques for Nonlinear Programming," Mathematical Programming, Vol 89, No. 1, pp. 149–185, 2000.

[18] Byrd, R.H., Mary E. Hribar, and Jorge Nocedal, "An Interior Point Algorithm for Large-Scale Nonlinear Programming, SIAM Journal on Optimization," SIAM Journal on Optimization, Vol 9, No. 4, pp. 877–900, 1999.

[19] Coleman, T.F. and Y. Li, "An Interior, Trust Region Approach for Nonlinear Minimization Subject to Bounds," SIAM Journal on Optimization, Vol. 6, pp. 418–445, 1996.

[20] Coleman, T.F. and Y. Li, "On the Convergence of Reflective Newton Methods for Large-Scale Nonlinear Minimization Subject to Bounds," Mathematical Programming, Vol. 67, Number 2, pp. 189–224, 1994.

[21] Gill, P.E., W. Murray, and M.H. Wright, Practical Optimization, London, Academic Press, 1981.

[22] Han, S.P., "A Globally Convergent Method for Nonlinear Programming," Vol. 22, Journal of Optimization Theory and Applications, p. 297, 1977.

[23] Powell, M.J.D., "A Fast Algorithm for Nonlinearly Constrained Optimization Calculations," Numerical Analysis, ed. G.A. Watson, Lecture Notes in Mathematics, Springer Verlag, Vol. 630, 1978.

[24] Powell, M.J.D., "The Convergence of Variable Metric Methods For Nonlinearly Constrained Optimization Calculations," Nonlinear Programming 3 (O.L. Mangasarian, R.R. Meyer, and S.M. Robinson, eds.), Academic Press, 1978.

[25] Waltz, R. A., J. L. Morales, J. Nocedal, and D. Orban, "An interior algorithm for nonlinear optimization that combines line search and trust region steps," Mathematical Programming, Vol 107, No. 3, pp. 391–408, 2006

Appendix A: Membrane and Piezoelectric Structural Analysis

The code capability developed in this project also calculates stiffness and mass matrices as well as stresses and other parameters for general membrane elements as well as piezoelectric actuators (rod and membrane elements). References [8] and [9] provide full derivations of the following sections.

A.1 Membrane Element

A membrane is a 2-dimensional element that carries in-plane loads only. Specifically, finite element modeling for this research uses the 4-node bilinear isoparametric quadrilateral (Q4) formulation. The Q4 may be any shape with four sides (including curved sides), and it is described using the reference coordinates (ξ, η) that map the element's shape to a square. The shape functions have the property such that both the displacement and location of a point within the element may be written in terms of the shape functions and nodal information– hence the "isoparametric" name – as seen in Eqs (A.1) and (A.2).

$$\{u \quad v \quad w\}^T = [N]\{d\} \tag{A.1}$$

$$\{x \quad y \quad z\}^T = [N]\{c\} \tag{A.2}$$

Where $\{d\}$ and $\{c\}$ are nodal degrees of freedom and nodal coordinates, respectively, and [N] is the matrix of shape functions. For the bilinear quadrilateral, the shape functions are defined as:

$$N_1 = \frac{1}{4}(1-\xi)(1-\eta) \tag{A.3}$$

$$N_2 = \frac{1}{4}(1+\xi)(1-\eta) \tag{A.4}$$

$$N_3 = \frac{1}{4}(1+\xi)(1+\eta) \tag{A.5}$$

$$N_4 = \frac{1}{4}(1-\xi)(1+\eta) \tag{A.6}$$

The element stiffness matrix is calculated by numerically integrating the following:

$$[K_e] = \iint [B]^T[E][B]t\,dxdy = \int_{-1}^{1}\int_{-1}^{1} [B]^T[E][B]\,t\,J\,d\xi d\eta \tag{A.7}$$

[B] is a 3x8 strain-displacement relationship, [E] is a 3x3 elastic modulus matrix, t is the thickness of the element, and J is the determinant of the Jacobian matrix. See Reference [9] for a full derivation of the stiffness matrix.

The result is an 8x8 stiffness matrix for the DOF $\{u_1 \quad v_1 \quad u_2 \quad v_2 \quad u_3 \quad v_3 \quad u_4 \quad v_4\}$, and the elements are then placed in the appropriate DOF locations for the full 24x24 matrix. Then, this matrix will be transformed into global coordinates for assembly into the overall structure's global stiffness matrix.

As for the truss, the element mass matrix for the Q4 may be computed using the lumped for consistent formulation. The elemental lumped and consistent matrices are shown in Eq (A.8) and (A.9), respectively.

$$[M_e^{lumped}] = \iiint \rho[N]dV \tag{A.8}$$

$$[M_e^{consistent}] = \iiint \rho[N]^T[N]dV \tag{A.9}$$

A.2 Piezoelectric Materials

From the Greek *piezo* for "pressure", piezoelectric materials demonstrate a relationship between their mechanical stress and an electric charge. For example, these materials develop an electric charge when restrained – a result of the piezoelectric effect; conversely, when placed in an electric field, the material deforms. The latter phenomenon, called the "converse piezoelectric effect," is useful for actuation of the material. [8][1] The constitutive relation for the converse effect is:

$$\begin{Bmatrix} \epsilon_1 \\ \epsilon_2 \\ \epsilon_3 \\ \epsilon_4 \\ \epsilon_6 \\ \epsilon_7 \end{Bmatrix} = \begin{bmatrix} S_{11} & S_{12} & S_{13} & 0 & 0 & 0 \\ S_{12} & S_{22} & S_{23} & 0 & 0 & 0 \\ S_{13} & S_{23} & S_{33} & 0 & 0 & 0 \\ 0 & 0 & 0 & S_{44} & 0 & 0 \\ 0 & 0 & 0 & 0 & S_{55} & 0 \\ 0 & 0 & 0 & 0 & 0 & S_{66} \end{bmatrix} \begin{Bmatrix} \sigma_1 \\ \sigma_2 \\ \sigma_3 \\ \sigma_4 \\ \sigma_5 \\ \sigma_6 \end{Bmatrix} + \begin{bmatrix} 0 & 0 & d_{31} \\ 0 & 0 & d_{32} \\ 0 & 0 & d_{33} \\ 0 & d_{25} & 0 \\ d_{15} & 0 & 0 \\ 0 & 0 & 0 \end{bmatrix} \begin{Bmatrix} E_1 \\ E_2 \\ E_3 \end{Bmatrix} + \begin{Bmatrix} \alpha_1 \\ \alpha_2 \\ \alpha_3 \\ 0 \\ 0 \\ 0 \end{Bmatrix} \Delta T \qquad (A.10)$$

Where d_{ij} is the piezoelectric modulus for normal strain in the *j*-direction for a voltage in the *i*-direction, E_i is the electric field applied in the i-direction, and S_{ij} is the elastic compliance for stress in the *j*-direction and accompanying strain in the *i*-direction.

A.2.1 Membrane SMA and Piezo Actuator

Membrane strain actuators are treated as Q4 elements, but there exists a field in the element's material information data structure that differentiates between a simple Q4 element and a Q4 actuator – and further, differentiates between an SMA, thermal, and piezoelectric actuator. Both forms of smart actuators have a similar structure; the "active" layers of material (SMA or piezoelectric material) are integrated into a composite layup. For the SMA actuator, the active layer includes SMA wires that are encased in a matrix of epoxy, for example, to act as the bias spring found in the actuator's formulation. Figure A.1 displays the construction of the membrane strain actuators.

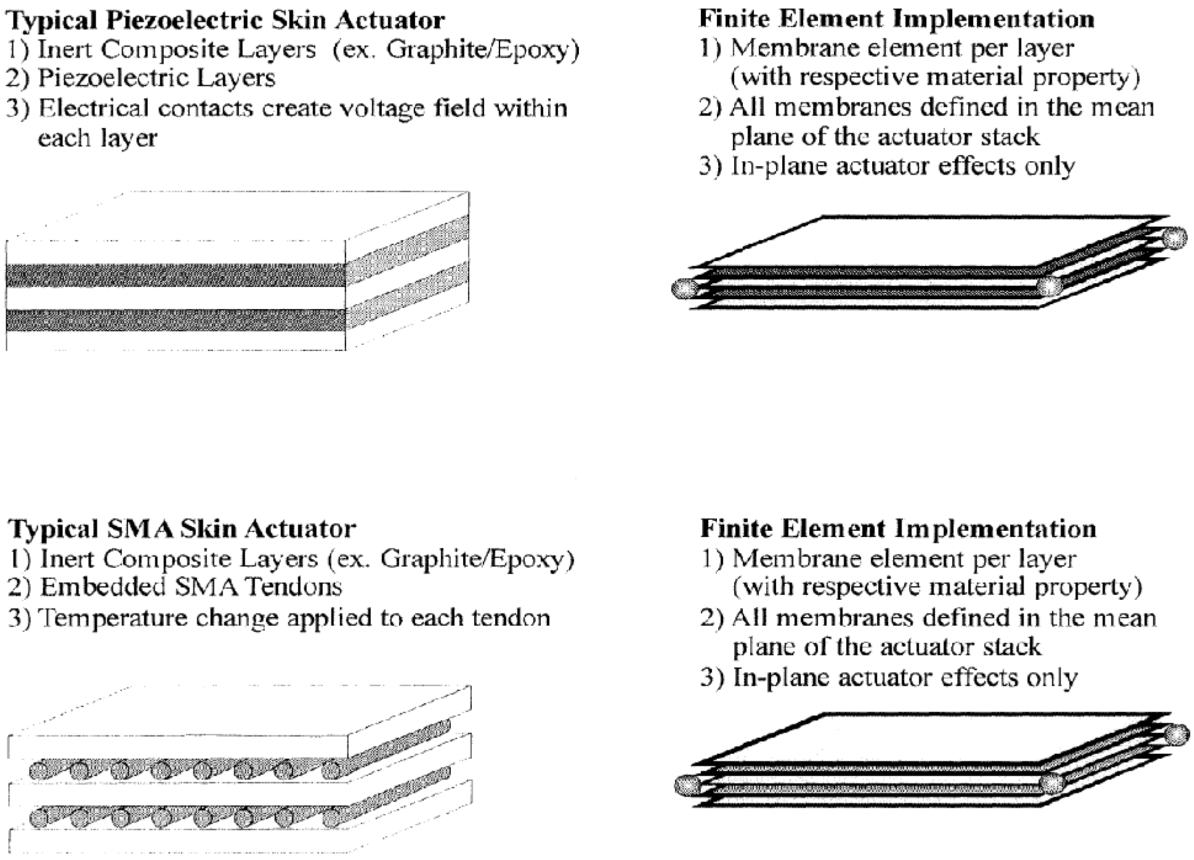

Figure A-1: Membrane Actuators

The general formulation for the force vector generated by an "active" membrane layer in the 1-direction of the material's local coordinate system is:

$$\{F_e\} = \iiint [B]^T [E] \{\epsilon_{active}\} dV \tag{A.11}$$

where $\{F_e\}$ is an 8x1 load vector, [B] is the 3x8 strain-displacement relationship matrix, [E] is the 3x3 elastic modulus matric, and $\{\epsilon_{active}\}$ is the 3x1 induced free-strain vector. The elements of $\{F_e\}$ are re-organized into a 24x1 vector to match the number of degrees of freedom of a membrane element, and then it may be transformed from the material system to the local element system, and then to the global system so that it may be assembled into the overall structure's load vector.

For orthotropic piezoelectric layers, the active strain is equal to:

$$\left\{\epsilon_{active}^{piezo}\right\} = \begin{bmatrix} 0 & 0 & d_{31} \\ 0 & 0 & d_{32} \\ 0 & 0 & 0 \end{bmatrix} \begin{Bmatrix} E_1 \\ E_2 \\ E_3 \end{Bmatrix} \tag{A.12}$$

For orthotropic shape memory alloy layers, the active strain is equal to:

$$\left\{\epsilon_{active}^{SMA}\right\} = \begin{Bmatrix} -(\sigma - \sigma_0)\left(\dfrac{1+\nu}{2E_c}\right) + \epsilon_0 \\ 0 \\ 0 \end{Bmatrix} \tag{A.13}$$

In this formulation, the equivalent spring value, k_{equiv}, rather than the bias spring stiffness is used for the matrix that surrounds the SMA wires. The equivalent spring value is calculated as:

$$k_{equiv} = \frac{E_c \pi t}{2(1+\nu)} \tag{A.14}$$

Here, E_c is the combined modulus of elasticity, t is the thickness of the active layer, and ν is the Poisson ratio for the SMA and matrix (both assumed to be 0.3). It is assumed that the SMA wires have a diameter equal to the thickness of the active layer and that the wires have a circular cross-section.

A.2.2 Bar Piezo Actuator

A common practice for piezoelectric actuation is to stack thin layers of piezoelectric materials then apply voltage between the layers, resulting in a displacement in the bar's axial direction. Following the standard definition of strain:

$$\epsilon_{33} = \frac{\Delta L}{L} \tag{A.15}$$

The change in axial length is:

$$\Delta L = d_{33} E_3 L = d_{33}\left(\frac{V_3}{L}\right)(nt) = d_{33} V_3 n \tag{A.16}$$

Here, d_{33} is the piezoelectric modulus in the axial direction due to an electric field, E_3. The electric field is equal to the applied voltage V_3 divided by the layer thickness, t, and then the length of the stack is a product of the number of layers, n, and t.

The piezoelectric force is then defined as:

$$F_{piezo} = \epsilon_{33} E A \tag{A.17}$$

where E is the modulus of elasticity of the material and A is the cross-sectional area of the piezoelectric stack. Lastly, the force generated by the piezoelectric bar actuator is assembled into the local coordinate load vector:

$$\left\{F_e^{piezo}\right\} = \{-F_{piezo} \quad 0 \quad 0 \quad 0 \quad 0 \quad 0 \quad F_{piezo} \quad 0 \quad 0 \quad 0 \quad 0 \quad 0\}^T \tag{A.18}$$

A.3 Stress in Membrane Elements

The stress calculation for a membrane element is:

$$\{\sigma\} = [E]([B]\{d\} - \{\epsilon_0\}) + \{\sigma_0\} \tag{A.19}$$

The terms $\{\epsilon_0\}$ and $\{\sigma_0\}$ are initial strains and stresses, respectively, and typically, only one of these terms is included unless there are multiple initial conditions simultaneously. Stress and strain contributions from piezoelectric and shape memory alloy materials contribute to the $\{\epsilon_0\}$ and/or $\{\sigma_0\}$ components. The mechanical strains are represented by the product of [B], a matrix that is a function of coordinates, and {d}, a vector of the elemental degrees of freedom.

For membrane elements, it is common practice to calculate stresses at Gauss points, which are points throughout the membrane element that produce more accurate stress measurements than at other locations. The code created for this research has the option of calculating stresses at these Gauss points, which are $\frac{1}{\sqrt{3}}$ distance from the center of the element, or at the nodes of the membrane. The stresses at each point are then averaged to determine an overall stress value for the membrane element. Figure A.2 demonstrates the locations of Gauss Points at points 1, 2, 3, and 4.

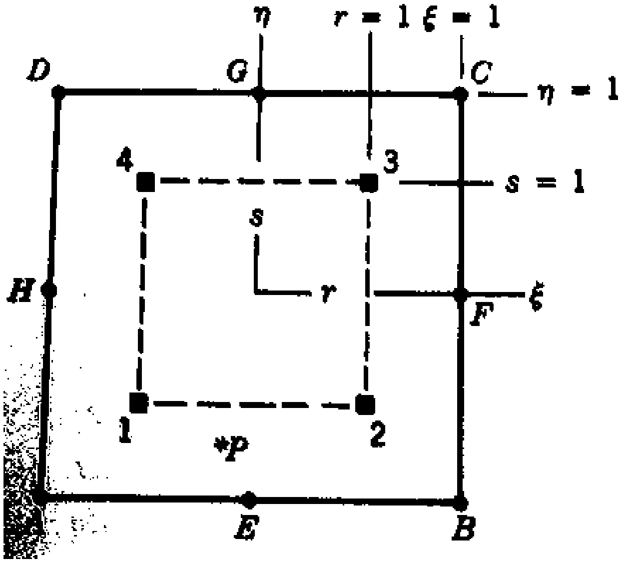

Figure A-2: Gauss Points of a QUAD Element [9]

A.4 Modal Analysis

When performing modal analysis, the free vibration problem is considered:

$$[M]\{\ddot{u}(t)\} + [K]\{u(t)\} = 0 \tag{A.20}$$

[M] and [K] are the global mass and stiffness matrices, respectively, and $\{\ddot{u}(t)\}$ and $\{u(t)\}$ are the global acceleration and displacement vectors. It is assumed that the solution is harmonic motion:

$$\{u(t)\} = \{\phi\}e^{j\omega t} \tag{A.21}$$

Substituting this solution back into the free vibration problem, the result is the generalized eigenvalue problem.

$$([K] - \lambda_i[M])\{\phi_i\} = \{0\} \tag{A.22}$$

The vector $\{\phi_i\}$ is the i^{th} mode shape and. Also, the i^{th} natural frequency, ω_i, is defined as:

$$\omega_i^2 = \lambda_i \tag{A.23}$$

Appendix B: Membrane Testing

A simple wing model is used to test the displacements and stresses computed by an assembly of truss and membrane elements. The Turner/Martin/Weikel wing, first studied by Eggwertz and Noton, is a cantilevered wing that has a 30 degree sweep and which is untapered throughout. Five identical spars and three identical ribs are fitted to the top and bottom skins of the structure. The cover skins are assumed to carry in-plane stress only; as a result, this portion of the wing is modeled with membrane elements. The spars and ribs are modeled with truss elements. The material used is aluminum with a Young's modulus of $10^7 psi$, Poisson ratio of 0.3, and density of $0.000259\ lbm/in^3$. The dimensions of the wing are shown in Figure B-1 and Figure B-2.

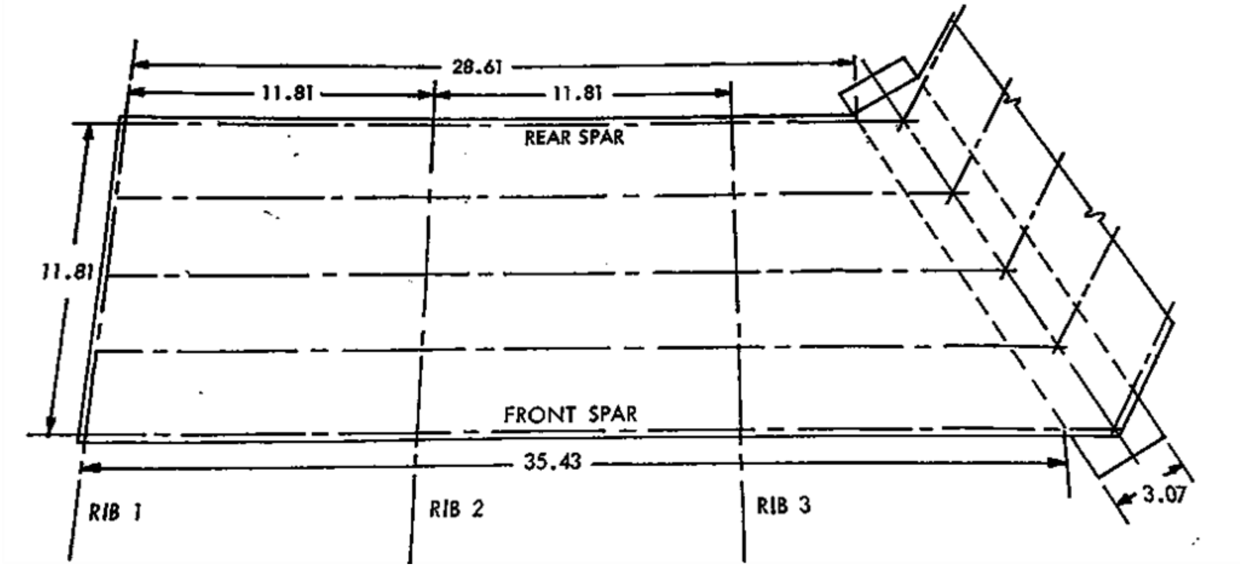

Figure B-1: Planform of the Turner Wing [14]

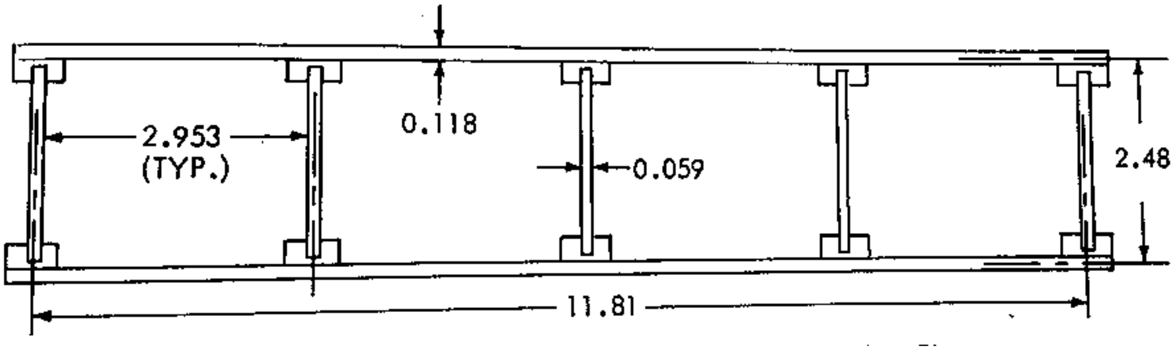

Figure B-2: Chordwise Section of the Turner Wing [14]

The wing is loaded with a 1 pound force downward at the tip of the trailing edge, as shown in Figure B-3.

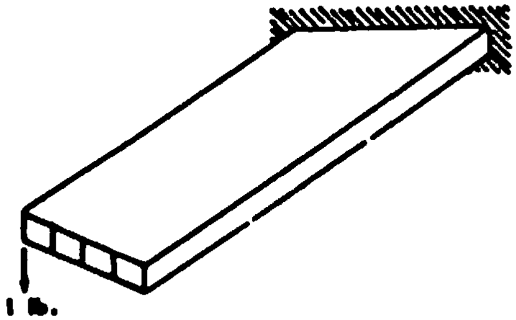

Figure B-3: Turner Wing Loading Condition [14]

In Ref [14], the each skin of the wing is constructed with 39 rectangles, which are separated into four triangular elements each, and four single triangles along the root. Harvey in Ref [15] has experimented with this same wing by using LST and CST elements to cover the skin; however, in this research the wing is constructed, as previously mentioned, with rod elements for the spars and ribs and with membrane elements for the skins. Overall, the structure contains 328 rod elements and 220 membrane elements, resulting in a 780 degree of freedom problem. The structure was built as a rectangular prism, with single point constraints being implemented to simulate the 30 degree sweepback.

The deflection results are shown in Figure B-4, with the red representing the deformed shape and the blue representing the original shape. Since the deflections are so small in magnitude, it is difficult to determine any major deformations from this figure.

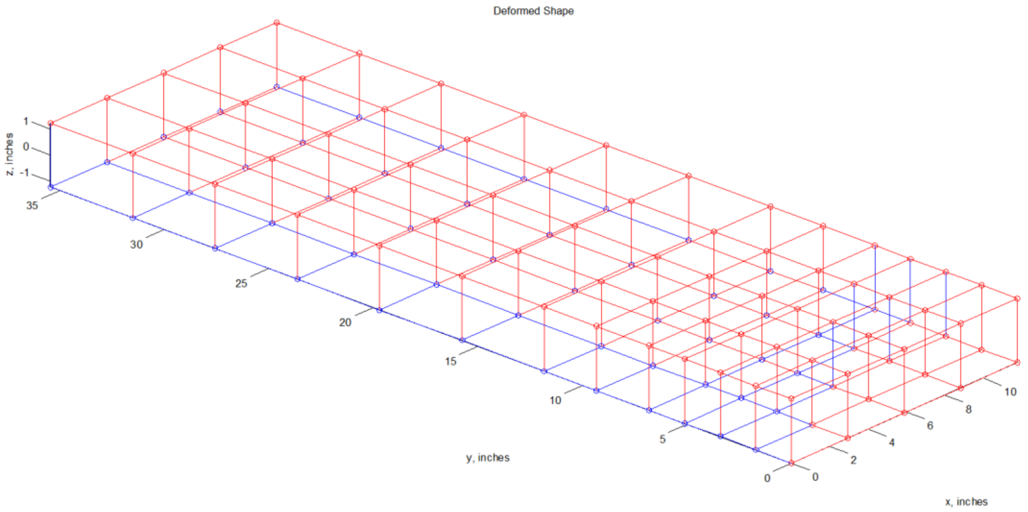

Figure B-4: Turner Wing Deformed Shape

The deflections of the leading and trailing edge of the Turner Wing are shown in Figure B-5. Data begins at the tip of the wing and expands inward to the wing root. The results match closely with the experiment conducted in Ref [14], with the largest wing deflection being at the trailing edge tip, where the load is applied, with a value of approximately 20×10^{-5} inches.

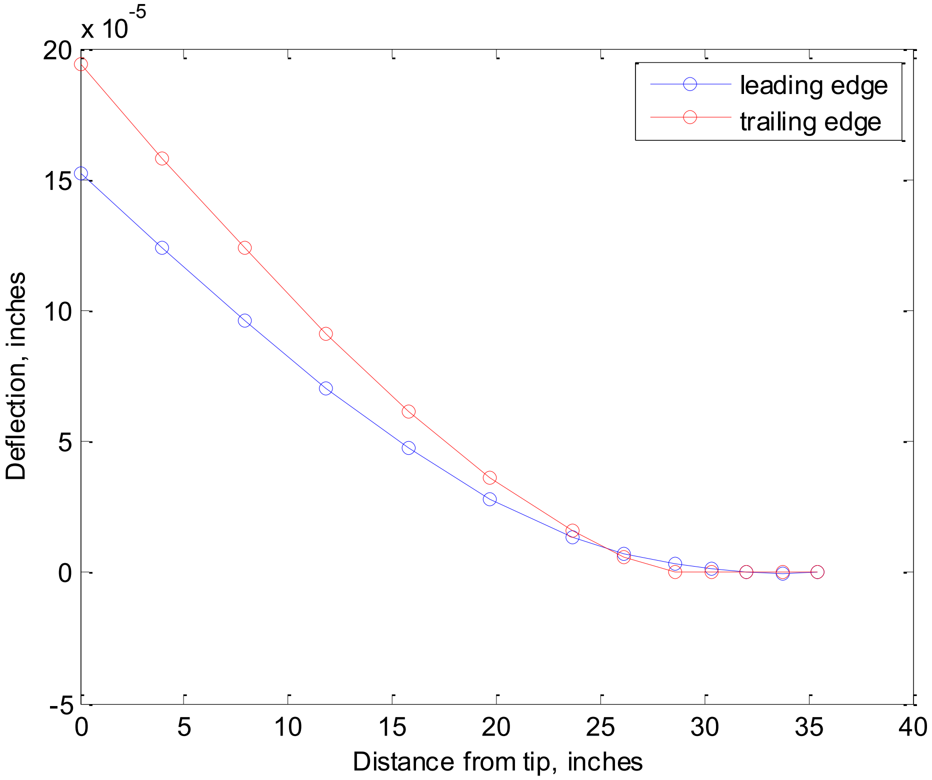

Figure B-5: Turner Wing Edge Deflections